Fábio João Oliveira Rodrigues

Microelectrodes for Biomedical Devices

UMinho | 2020

Universidade do Minho
Escola de Engenharia

Fábio João Oliveira Rodrigues

Microelectrodes for Biomedical Devices

julho de 2020

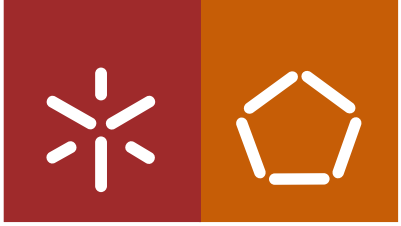

Universidade do Minho
Escola de Engenharia

Fábio João Oliveira Rodrigues

Microelectrodes for Biomedical Devices

Tese de Doutoramento
Doutoramento em Engenharia Biomédica

Trabalho efetuado sob a orientação do
Professor Doutor Paulo Mateus Mendes
e do
Professor Doutor Luís Gonçalves

julho de 2020

ACKNOWLEDGEMENTS

In first place I'd like to thank my parents, Leonor and António. O meu muito obrigado a vós, por me terem ensinado a escutar a opinião e o saber das outras pessoas. Mas sempre a decidir pela minha própria cabeça, para isso tenho "uma em cima dos ombros". Sem esses ensinamentos esta Tese nunca teria existido.

The second big acknowledgement goes to my supervisor, Professor Paulo Mateus Mendes, for his unconditional and nearly endless (!) support throughout this Thesis project and writing. Thank you for introducing me to the fascinating world of electrodes and for all the fruitful discussions.

I wish to express my deepest gratitude to Professor Lina Sarro. Thank you for making me feel as part of the ECTM team in Delft, something I will never forget. And thank you for put me in the same office as Bruno, female intuition at its finest. I'd like to thank and hug my friend Bruno Morana, a special thanks to you, for your immense support, more than a colleague you were like a big brother, duude! Also thanks to Gregory Pandraud, Cinzia Silvestri, Benjamin Mimoun, Nishant Lawand, Giuseppe Fiorentino, and others at TU Delft who helped me in some way. Also wish to thank Professor Marian Bartek for having received me in Delft.

I would like to thank Professor Luís Gonçalves, Professor Higino Correia, João Ribeiro and Pedro Anacleto at Universidade do Minho for all their support, as well as the collaborators in Grenoble, Olivier David and Pascale Pham, respectively from Grenoble Institut des Neurosciences and CEA-Leti. Thank you José Amaral for the proofreading.

Last but not least I wish to thank my girlfriend Caroline. Obrigado por tudo.

The author, Fábio João Oliveira Rodrigues, was supported by FCT, the Portuguese Foundation for Science and Technology, under projects PTDC/EEI- TEL/5250/2014 - POCI01-145-FEDER-16695, by FEDER funds through Projeto 3599 – Promover a Produção Científica e Desenvolvimento Tecnológico e a Constituição de Redes Temáticas (3599- PPCDT), grant SFRH/BD/62608/2009, and the project CMEMS reference UID/EEA/04436/2019.

Governo da República Portuguesa

UNIÃO EUROPEIA
Fundo Social Europeu

STATEMENT OF INTEGRITY

I hereby declare having conducted this academic work with integrity. I confirm that I have not used plagiarism or any form of undue use of information or falsification of results along the process leading to its elaboration.

I further declare that I have fully acknowledged the Code of Ethical Conduct of the University of Minho.

Microelectrodes for Biomedical Devices

Resumo

Os avanços em miniaturização, assim como a introdução de novos materiais tem permitido, e continuará a permitir, a expansão do campo de dispositivos médicos. Frequentemente, as interfaces entre estes dispositivos e o corpo humano tem por base elétrodos de platina e silicones. Todavia, materiais de elétrodo alternativos, como o nitreto de titânio, que não se baseiam em injeção de carga do tipo farádica com potenciais reações irreversíveis, e que são mais acessíveis em salas limpas para processos de CMOS, aumentam o potencial de integração dos dispositivos e a sua segurança para o corpo humano. Desta forma, visionamos um dispositivo médico implantável com elétrodo em nitreto de titânio, com injeção de carga de tipo capacitiva, que tanto possibilita a estimulação de nervos como a leitura da sua actividade.

Esta Tese apresenta a análise, desenho, fabrico e caracterização de elétrodos em nitreto de titânio em substratos flexíveis de poliamida, com o tamanho mínimo de microelétrodo de 80 × 80 μm^2. A análise de flexibilidade dos elétrodos de nitreto de titânio em poliamida assenta em modelos teóricos, previamente validados, que prevêem um raio de curvatura mínimo de 500 μm. A metodologia para o desenvolvimento dos elétrodos de nitreto de titânio combina várias técnicas de microfabrico, como por exemplo, a fotolitografia, a deposição por vapor químico, o *sputtering*, e várias técnicas de remoção de materiais. Os elétrodos em poliamida, obtidos a partir de processo em bolachas de silício, podem daí ser destacados e posteriormente integrados em estruturas em forma de algema (*cuff*). Essas estruturas em *cuff* foram desenhadas, também no âmbito desta Tese, tendo em conta os requisitos anatómicos do nervo vago do rato, onde foram anatomicamente validadas. Depois do fabrico, os elétrodos foram caracterizados através de três métodos eletroquímicos: espectroscopia de impedância eletroquímica, voltamétrica cíclica e medições em transiente de tensão. Os microelétrodos em nitreto de titânio apresentam uma impedância média de 59 kΩ a 1 kHz, mecanismo capacitivo de injeção de carga com *water window* de -0.6 V to 0.8 V, e uma capacidade de injeção de carga equivalente a 154 ± 16 $\mu C/cm^2$, podendo ser usados em aplicações de micro-estimulação cortical ou tomografia por impedância elétrica. Microelétrodos de nitreto de titânio em poliamida, processados de modo compatível com o *back-end CMOS* e obtidos a partir das bolachas de silício, são uma solução promissora para interface neuronal que, no futuro, pode beneficiar da integração de módulos eletrónicos no *chip* de silício.

Palavras-chave: Dispositivos biomédicos, microelétrodos, nitreto de titânio, poliamida

Microelectrodes for Biomedical Devices

ABSTRACT

Advances in device miniaturization as well as the introduction of new materials are enabling and will continue to enable an expansion in the field of medical devices. Interfaces between such devices and the human body are often based on platinum electrodes and silicones. However, alternative electrode's materials, such as TiN, do not rely on faradaic charge injection with potentially irreversible reactions, and are easy to process in CMOS cleanrooms, thus increasing the potential for device integration and safety to human body. Hence, we envision an implanted medical device with TiN as electrode material, with capacitive charge injection that enables stimulation of nerve tissue, as well as readout of its activity.

This Thesis addresses the analysis, design, fabrication and characterization of novel TiN electrodes on flexible polyimide substrates, with the smallest microelectrode size of 80 × 80 μm^2. The analysis of flexibility of polyimide-based, TiN electrodes is based on previously validated theoretical models that predict an allowed bending radius of 500 µm. A methodology for development of TiN electrodes has been developed that combines various microfabrication techniques, e.g., photolithography, chemical vapor deposition, sputtering, and various etching techniques. Polyimide-based electrodes have been released from silicon wafers and then integrated into cuff structures that were designed to target the rat vagus nerve. Assembled cuffs have been imaged by CT scan, and the cuff dummies (no electrode) were validated *in vivo*.

After fabrication, we characterized the fabricated electrodes by three main electrochemical methods: electrochemical impedances spectroscopy, cyclic voltammetry, and voltage transient measurements. TiN microelectrodes exhibit an average impedance of 59 kΩ at 1 kHz, a capacitive charge injection mechanism with water window of -0.6 V to 0.8 V, and charge injection capacity of 154 ± 16 $\mu C/cm^2$, making them suitable for applications like intracortical stimulation or electrical impedance tomography. TiN-on-polyimide microelectrodes, processed as back-end CMOS compatible process and then released from silicon wafers, are a promising solution for neural interfaces targeting at submillimeter nerves, which may benefit from future upgrades with die electronic modules.

Keywords: Biomedical devices, microelectrodes, polyimide, titanium nitride

Contents

Index of Figures

Index of Tables

List of Abbreviations

AIMD – active implantable medical device

AIROF – activated iridium oxide film

CIC – charge injection capacity

CMOS – complementary metal-oxide-semiconductor

CNS – central nervous system

CSC – charge storage capacity

CV – cyclic voltammetry

CVD – chemical vapor deposition

DRIE – deep reactive ion etching

EIS – electrochemical impedance spectroscopy

ESA – electrochemical surface area

FINE – flat interface nerve electrode

GSA – geometric surface area

LIFE – longitudinal intrafascicular electrode

MEAs – microelectrode arrays

MEMS – microelectromechanical systems

PBS – phosphate buffered saline

PECVD – plasma-enhanced chemical vapor deposition

PI – polyimide

PDMS – polydimethylsiloxane

PNS – peripheral nervous system

PVD – physical vapor deposition

SEM – scanning electron microscope

SIROF – sputtered iridium oxide film

TiN – titanium nitride

TIME – transverse intrafascicular multichannel electrode

USEA – Utah slanted electrode array

VTM – voltage transient measuremen

Consiste o progresso no regresso às origens com a plena memória da viagem.

Agostinho da Silva

1 Introduction

Due to the remarkable advances in various engineering fields and medical disciplines, neural prostheses keep growing in numbers and applications, being now offered as a routine clinical treatment for several health conditions. Neural prostheses can be defined as medical devices that activate neural tissue by meaningful electrical stimulation directly delivered onto the nerves, thus help restoring lost body functions. According to European legislation, an active implantable medical device (AIMD) is any device relying for its functioning on a source of electrical energy that is intended to be totally or partially introduced into the human body (article 1.2 c) and d), [1]). Thus, neural prostheses can be considered as a type of active implantable medical device. Throughout this Chapter, these two terms will be used interchangeably.

The first implantation in a human of an electrically-driven medical device to restore function took place in 1958, when Arne Larsson received his first pacemaker at the age of 43 [2]. Important advances in technology have enabled manufacturing of this implantable pacing device, e.g., the newly available planar silicon transistors [3] – Figure 1.1. However, in their first generations, these implantable devices were prone to failure in their electronics and leads, thus requiring several revision surgeries and re-implantations [4]. Throughout his lifetime, Arne was implanted with 26 different cardiac pacing devices until his death in 2001, by the age of 86 years.

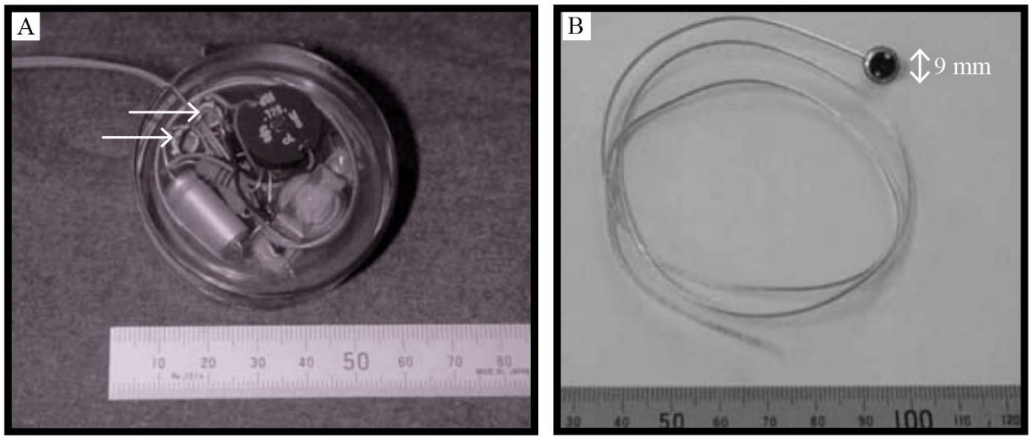

Figure 1.1 The first active implantable medical device, a cardiac pacemaker from 1958 [4]. A) Implantable pulse generator with two silicon transistors (arrows) embedded in epoxy resin. B) Implantable electrode lead consisting of four thin stainless steel strips wound around a thread core. The lead is insulated with soft polyethylene and at the tip, the epicardial stimulating electrode, consisting of a platinum disc with 9 mm in diameter (equivalent area of 63 mm^2), to be sutured to the epicardium through two small holes.

With over 1.5 million devices implanted in 2015 in Europe alone [5], the cardiac implantable electronic devices (pacemakers and defibrillators) are the most used AIMDs and, perhaps, the best known. Today, however, there are successfully marketed AIMDs in many other medical areas to tackle conditions or impairments which have no alternative medical treatment. These include, and to name only a few, cochlear implants for sensorineural hearing loss [6], retinal implants for retinitis pigmentosa [7], deep brain stimulators for patients with Parkinson´s disease and long-term resistance to medication [8], spinal cord stimulators for chronic spinal pain [9], and vagus nerve stimulators for intractable epilepsy and treatment-resistant depression [10-11]. These neural prostheses vary significantly in their technological complexity, materials used and surgical implantation procedure. Three examples of commercially available AIMDs are presented in Figure 1.2 that stimulate different neural populations.

One of the world's largest market research database, the Grand View Research, mentions that, in 2015, the global market of neuroprosthetics worth USD 4.2 billion and expecting to reach the toll of USD 14.6 billion by 2024 [17]. As applications of the already-marketed AIMDs continue to expand and new AIMDs are sought for targeting so far unaddressed medical conditions, the demand for new and advanced implantable materials and technologies will continue to grow. Since the first cardiac pacemaker has been implanted, in 1958, reliability and tolerability of AIMDs have increased significantly thanks to advances in many engineering fields, e.g., implantable materials, batteries and microelectronics. Power consumption in AIMDs has decreased due to miniaturization and low-power integrated circuits [18-19]. Likewise, materials used in implants have improved in performance and resistance to wearing. The epoxy resin encapsulation of the 1958's pacemaker was developed to protect electronic circuits and batteries from body fluid penetration but it has absorbed moisture, swelled and, eventually, dissolved inside the human body [20]. Today, electronic circuits and implanted batteries in AIMDs are protected by titanium cases as shown in Figure 1.2, and biocompatible, non-degradable polymers are used as support materials for electrode arrays and coatings. Since 1958, the size of stimulation and recording electrodes in AIMDs has been downsized, thanks to introduction of new technologies, materials and manufacturing procedures. As new technologies and materials become available, it is possible to realize electrodes for novel applications.

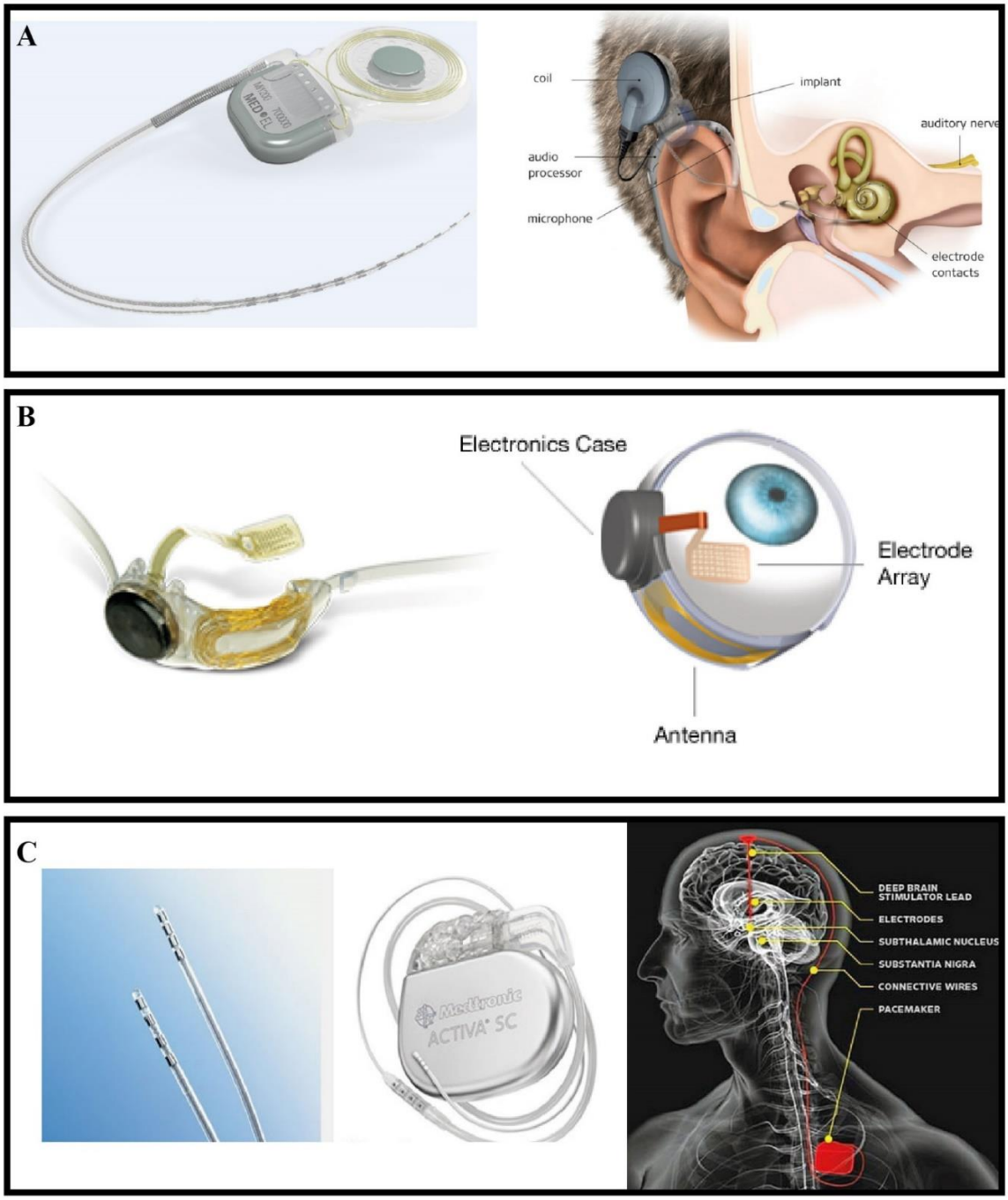

Figure 1.2 Commercially available active implantable medical devices. A) The SYNCHRONY cochlear implant system. The implant comprises an internal coil, titanium-cased electronics and an electrode lead and array. The electrode lead is made of silicone and the array comprises up to 24 platinum electrode contacts (0.14 mm^2 each), being surgically inserted into the cochlea [12]. B) The Argus® II Retinal prosthesis system. The implant comprises an internal coil, the electronics case (which are fixed to the sclera outside of the eye) and a thin film polyimide-based electrode array that is surgically positioned onto the surface of the retina. The electrode grid comprises 60 platinum electrodes (6 x 10 matrix, approx. 0.03 mm^2 each) [13-14]. C) The ACTIVA™ deep brain stimulator. The implant, typically implanted subcutaneously near the clavicle, comprises a titanium case connected to an extension and leads, which are implanted in the brain. The electrode array contains 4 electrode contacts of a platinum/iridium alloy with 6 mm^2 each [15-16].

1.1 Electrode Arrays as Neural Interfaces

The first operation for implanting a pacemaker was done by the surgeon Ake Senning, who performed an open thoracotomy and suturing of a 9 mm diameter electrode (area of approx. 63 mm^2). Today, small sized and lightweight pacemakers with flexible platinum lead coils make implantation possible without an open-heart surgery [20]. Miniaturization in electronics and implantable technology has brought benefits not just for patients with cardiac pacemakers, where a large muscle is targeted but, even more soundly, in treatments where small neural populations need to be stimulated. In fact, emergent areas of medical innovation include the development of near-millimeter and sub-millimeter electrode arrays to be implanted in peripheral nerves or in the central nervous system [21]. Diversity of neural structures in the central and peripheral nervous systems require developing electrodes of various shapes, with varying mechanical and electrochemical characteristics. Advances in vast groups of technologies including microtechnologies, laser cutting, laser welding, biocompatible polymers and connectors, to name a few, have enabled new electrode concepts to be developed, suitable for neural interfaces on the near-millimeter and sub-millimeter scales – Figure 1.3. Examples range from "flat" silicone electrodes for the rectangular-shaped femoral nerve [22], tibial and peroneal nerves [23], to silicone-based cuffs suitable for rather cylindrical-shaped nerves like the sciatic and its branches [24-25], and upper limbs [26-27], highly-invasive Utah electrode arrays, obtained by micromachining and photolithography processes, for the sciatic [28-29], thin film polyimide-based transverse intrafascicular electrodes suitable for median and sciatic nerves [30-32], ultra-flexible, microwire neural probes for the cortex [33], and CMOS, rigid probes with high number of electrode sites for single neuron recordings [34].

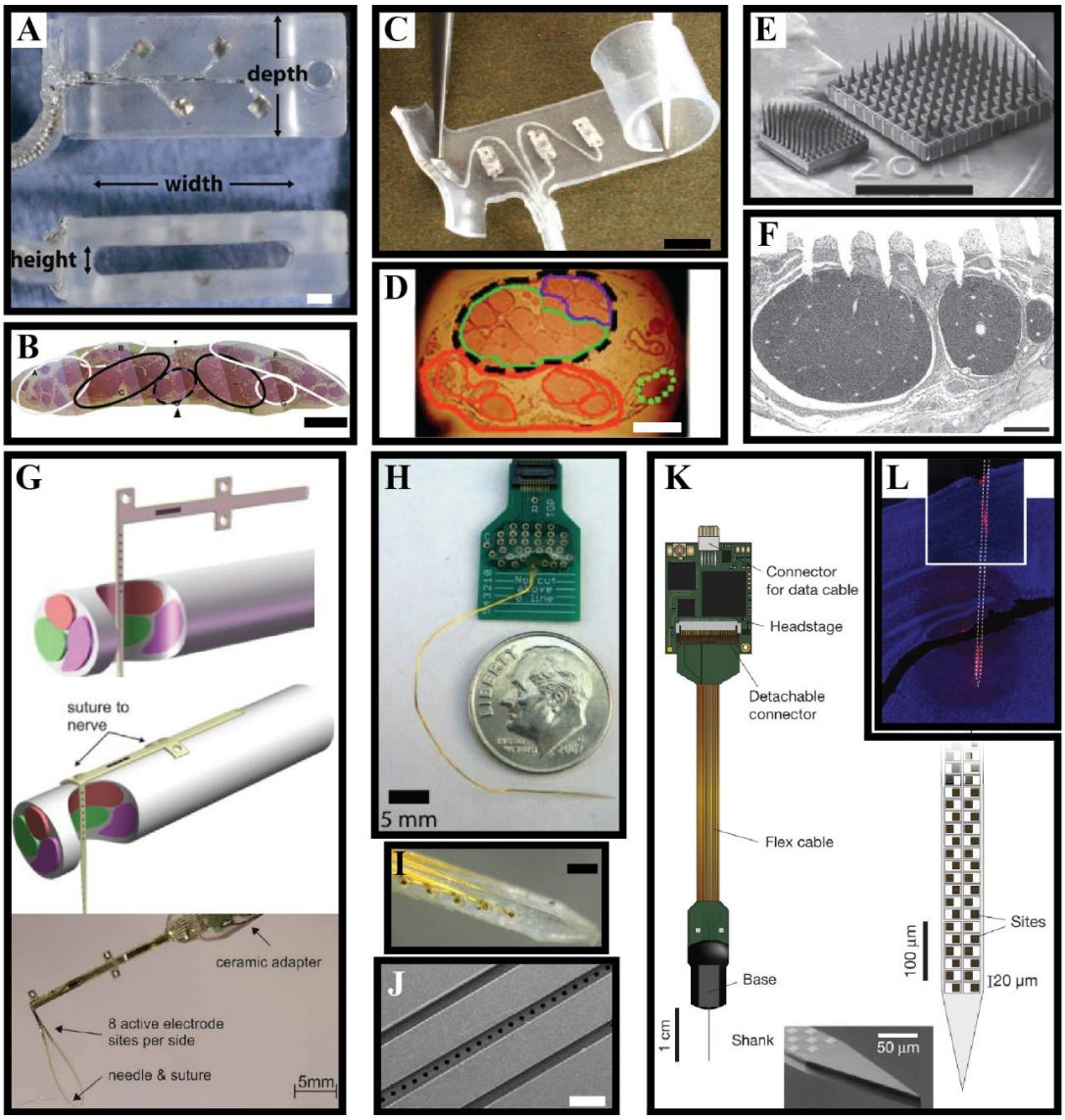

Figure 1.3 Electrode arrays for peripheral and central nervous systems. A) Flat interface nerve electrode. Laser cut, 0.2 mm^2 platinum iridium contacts are welded onto stainless steel leads and embedded in silicone housing. Scale bar: 1 mm [22]. B) Fascicular anatomy of human femoral nerve. Black circles denote fascicles activated for standing. Scale bar: 2 mm [35]. C) Spiral cuff electrode with 4 x 0.5 mm^2 platinum contacts embedded between 2 sheets of silicone rubber. Scale bar: 1 mm [25, 27]. D) Fascicle map of tibial nerve, with fascicles responsible for plantar flexion in red. Scale bar: 1 mm [36]. E) High-density Utah slanted electrode array with 400 electrodes obtained from wafers processed by dicing, wet etching and sputtered with iridium oxide. Scale bar: 3 mm [29]. F) Rat sciatic nerve shows penetration of a row of HD-USEA electrodes into the top portion of fascicles. Scale bar: 200 µm [29]. G) Transverse intrafascicular multichannel electrode. (Top) schematic of the implantation procedure, with fixation tabs on the ribbon part of the electrode available for suturing to nerve. (Bottom) Thin-film polyimide with 8 platinum contacts are processed via micromachining techniques. H) A 32 channel microwire microelectrode array with 500 μm^2 iridium oxide contacts and connector [37]. I) close-up of contacts and gold wires bundled together by epoxy, using vacuum molding. Scale bar: 150 µm. J) Close-up of a micromold used for assembly. Scale bar: 500 µm. K) Neuropixels probe with 960 x 400 μm^2 titanium nitride sites for neuron recording in the brain, obtained by CMOS process [34]. L) Histological reconstruction of the probe track with tip in the thalamus.

1.2 Polymer-based Microelectrode Arrays

Functionality and performance of neural interfaces in modern implantable medical devices, which can deliver electrical stimulation to sub-nerve populations of 1 to few fascicles, or record from single neurons are on the rise. Such requirements demand for increased device complexity with high number and high densities of electrode contacts per device. Applications requiring high density microelectrode arrays (MEAs) include, but are not limited to, the intracortical microstimulation of somatosensory cortex for creating a sensory neuroprosthesis to restore tactile sensation [38-39], electrical impedance tomography (EIT) of peripheral nerves [40-41], and stimulation of upper limb nerves for restoring arm and hand function in people with high level tetraplegia [26, 42].

In addition to electrode contact density, one other requirement that must be fulfilled by microelectrode arrays is about matching of their mechanical properties to that of neural structures. A typical approach for achieving good mechanical compliance between electrodes and neural tissue is by use of flexible or stretchable materials as substrate/support for the electrodes, instead of rigid ones. Indeed, use of polymeric thin films like parylene-C, polydimethylsiloxane (PDMS), polyimide (PI), liquid crystal polymer (LCP), and shape memory polymer (SMP) as substrate materials, approximate Young's modulus of the MEAs to that of neural tissues, when compared to thicker or silicon-based ones [43-45]. Few examples of thin film microelectrode arrays based on micromachining of polymers are the ones based on parylene [46-47], PDMS [40, 48], multi-electrode softening cuffs (MSC) based on thiol-ene/acrylate shape memory polymer (SMP) [49], polyimide-based graphene MEAs [50-51], polyimide-based CNT arrays [52], and polyimide-based micro-LEDs and iridium oxide microelectrodes [53]. Few of the MEAs mentioned above are shown in Figure 1.4.

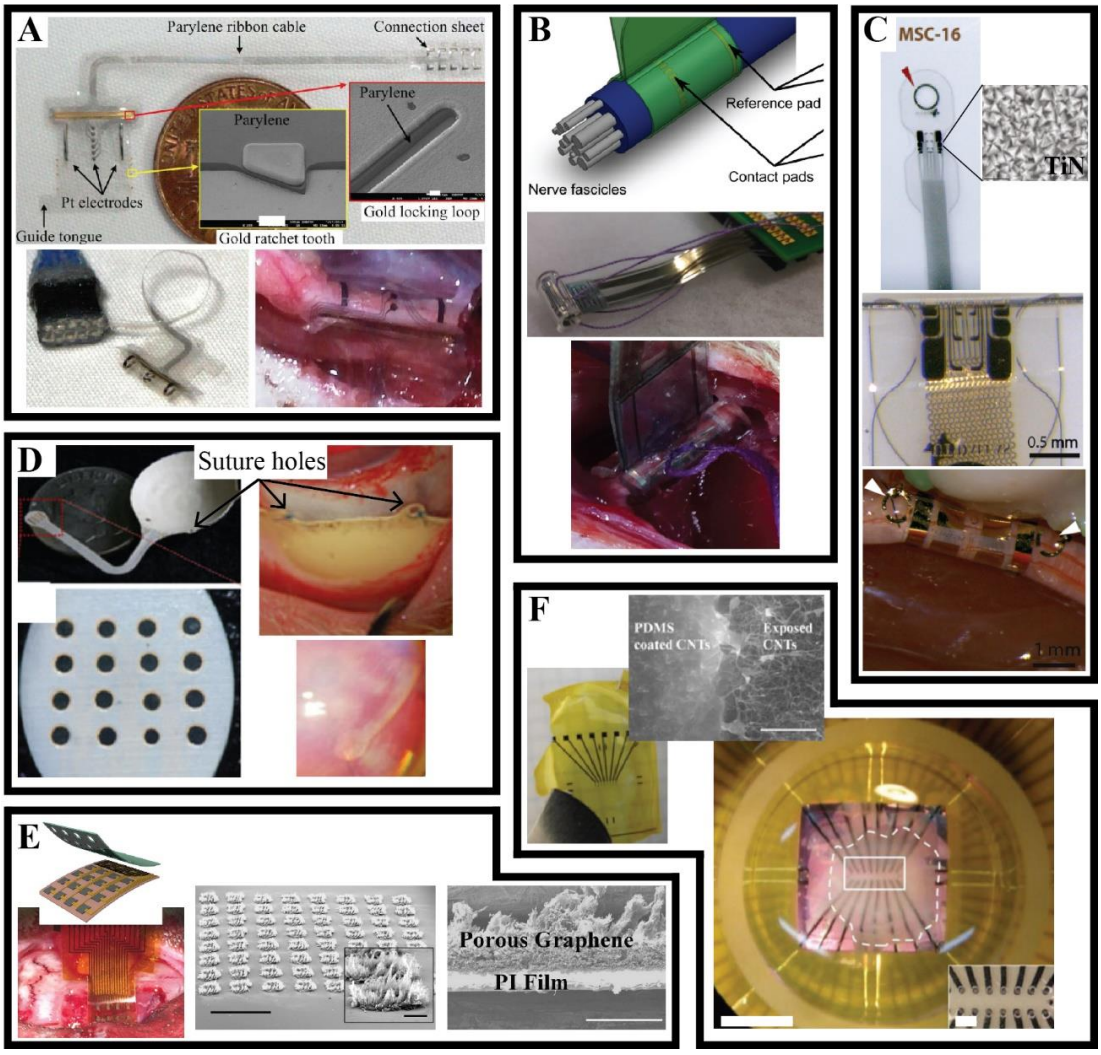

Figure 1.4 Polymer-based microelectrode arrays. A) Parylene-based cuff electrode with 6 x 0.07 mm^2 platinum electrodes. Scale bars: are 100 μm (ratchet) and 10 μm (locking loop). (Bottom left and right) 1.7 mm diameter cuff in a closed state, implanted in rat sciatic [46]. B) PDMS-based cuff electrode with 16 x 0.1 mm^2 platinum MEAs and 1.4 mm inner diameter, used for EIT in the rat sciatic nerve [40]. C) Multi-electrode softening cuffs (MSC) based on thiol-ene/acrylate shape memory polymer (SMP), using titanium nitride (TiN) MEAs with areas from 0.014 to 0.14 mm^2. (Middle) MSCs on a 100 μm diameter metal rod. (Bottom) and on a 1 mm diameter rat sciatic, respectively [49]. D) Liquid crystal polymer-based retinal prosthesis. (Top left) inner surface of the device and comparison with a dime. The device is 14 mm in diameter and 1.3 mm thick. (Bottom left) 16 iridium oxide electrodes. (Top right) prosthesis implanted in the retina and secured with sutures. (Bottom right) detail of microelectrode array [54]. E) Polyimide-based, porous graphene microelectrodes. (Top left) patterned graphene spots (gray squares) on polyimide layer, are subsequently encapsulated with a SU-8 layer. (Bottom left) A 16 electrode array placed at the pial surface of barrel cortex, ready for sensing and microstimulation. (Middle) tilt SEM image of a 64-spot porous graphene array. Scale bars: 1mm (array) and 100 μm (single contact). (Right) SEM image of the cross-section view of porous graphene. Scale bar: 100 μm [50]. F) Carbon nanotubes (CNTs) microelectrodes on flexible substrates. (Left) CNTs on polyimide. (Middle) Cross section of CNTs. (Right) CNT, 16-electrode array on a PCB. Scale bar: 5 mm. An embryonic retina was flattened on the electrode array. The edge of the retina is marked with a dashed line. Inset: enlargement of the electrodes area (area marked with a solid line; scale bar: 200 μm) [52].

1.3 Polyimide as Processing Material

Polymer-based electrode carriers optimize the mechanical and the electrical contact of electrode arrays with delicate soft neural tissues. When using fabrication technologies employed in microelectromechanical systems and integrated circuits for manufacturing of polymer-based microelectrode arrays, one important limitation to consider is the processing temperature. For semicrystalline polymers used in microfabrication of neural electrodes, e.g., PDMS, parylene-C, thiol-ene/acrylate shape memory alloy, liquid crystal polymer and polyimide, the glass transition temperature, T_g, is well below the melting point and marks the temperature range in which, on cooling, the brittleness increases markedly. In practice, when heating above T_g, these polymers become a viscous liquid with freer molecules and, upon cooling down the material, it forms an amorphous, brittle solid of altered chemical and mechanical properties. So, particular attention shall be paid to each processing step and its temperature, when selecting a specific polymer as substrate material for a flexible MEA. Yu *et al.* [46] have used parylene-C as substrate material for their cuff electrode – Figure 1.4 A. As T_g of parylene-C is around 103 °C [55], soft baking of photoresist was done at 98 °C and plating of gold for locking features at 55 °C, in order to avoid brittleness. Glass transition of thiol-ene/acrylate shape memory alloy and PDMS is 40 °C [56] and 150 °C [57], respectively. Melting temperature of liquid crystal polymer is at around 330 °C [54]. Amongst most used polymers in flexible microelectrode arrays, polyimides are the ones with best thermal budgets, as their glass transition temperatures is above 400 °C [58]. Polyimide was chosen as a substrate film for microelectrode arrays in the current Thesis.

1.3.1 Polyimide-to-rigid integrated assemblies

When designing flexible electrodes, one needs to consider how the interface with silicon dies that house IC components will look like. And, apart from the requirements on electrical interfaces, another requirement to consider during the design phase of flexible electrodes, is their mechanical handling by the final user. Electrodes that are based entirely on polyimide foils are extremely difficult to handle in a surgical/*in vivo* environment, as those thin and flexible foils tend to curl in undesired and unpredictable manners. Several approaches to render polyimide-based electrodes interfacing with rigid components for signal conditioning, connection and handling have been reported in the literature – Figure 1.5. Meyer *et al.* [59] have introduced the Microflex interconnect technology (MFI) with rivet-like interconnections through metalized vias on polyimide substrates. By welding of gold studs on top of those vias, silicon dies with IC components, adapters and connectors can be connected to the flexible polyimide foils. Welding is based on the thermosonic ball-wedge bonding process and is done by applying force, temperature, and

ultrasound onto the metal layer, e.g., aluminum, gold, copper, or nickel. Flexible and modular integration are advantages of this approach, however, one disadvantage of the MFI technology are the multiple steps required for integration of electrodes, IC components and connectors. Myllymaa *et al.* [60] have processed polyimide electrodes on glass substrates, delaminated them and cut to their final shape using scissors and knife. Thin film connector pads were designed to fit into a zero-insertion-force (ZIF) connector. In their design, a PCB allows interface with an external preamplifier, and further to the recording instrumentation. Their approach required that thin film pads are soldered to the connector, which may result in short circuits, if small pitch designs are intended. Additionally, in this approach, handling of stand-alone, thin film polyimide foils is necessary when mounting them onto the ZIF. As previously mentioned, this can be extremely challenging (and frustrating) as polyimide films tend to curl randomly. More recently, Tolstosheeva *et al.* [61] have proposed a novel microfabrication method, using silicon wafers as substrates, that renders flexible polyimide electrodes attached to silicon dies. In their approach, the microelectrode array is processed as a free-standing device to enable monolithic integration of a rigid interposer, designed for soldering of fine-pitch SMD-connectors on minimal assembly area. Using a polyimide-metal-polyimide process, a high density array of 128 electrode contacts designed for electrocorticography (ECoG) was achieved. The metal layers used in their work were titanium (for promote adhesion to polyimide) and gold as electrode and bonding material. Silicon dies were used solely as substrates for connector pads. If CMOS processes are to be used in such silicon wafers for monolithic integration of IC components, the use of gold precludes that possibility. It is well known that gold is not CMOS compatible due to its property to quickly diffuse into silicon or silicon oxide layers [62]. One other approach of interest to promote interconnection of polyimide electrodes with rigid components is the use of anisotropic conductive films (ACFs). Baek *et al.* [63] have introduced this technological approach that connects pads on polyimide to pads on PCB by a conductive epoxy activated by temperature and pressure. High precision alignment is key in this process, and the high pressures (4 kgf/cm^2) required can rupture the electrodes or interconnects on polyimide.

Other groups have reported on efficacious technologies to interface polyimide with various rigid materials. Mian *et al.* have obtained bonding of polyimide to titanium by laser welding [60], but that is most beneficial for packaging, as titanium is a state-of-the-art material for packaging of medical devices. Other reference works are the ones where polyimide is used as an interconnect material between rigid, silicon-based neural probes and small connectors [64-65].

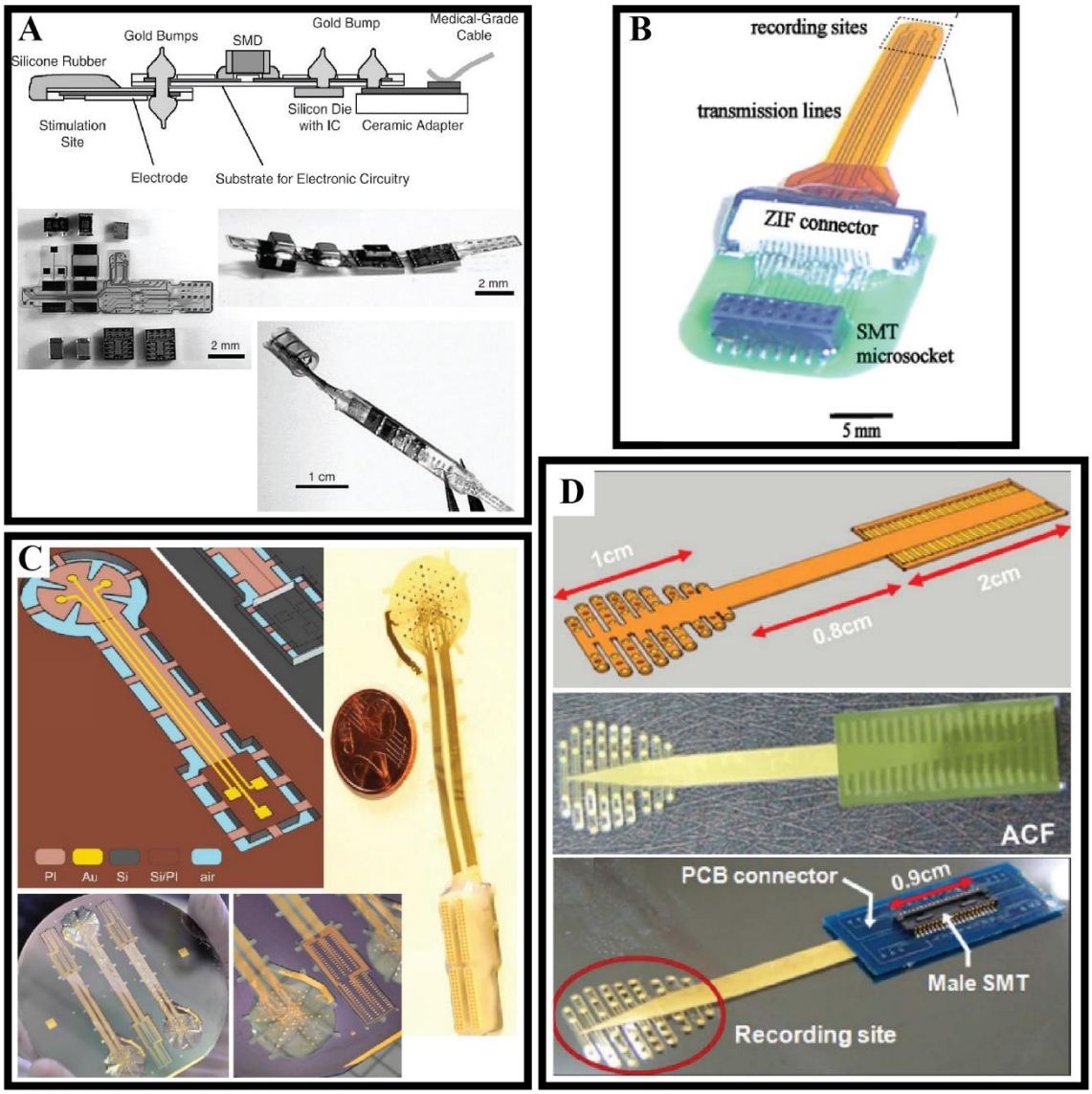

Figure 1.5 Technological approaches to interconnect polyimide-based electrodes with rigid components. A) Microflex interconnect technology. (Top) The system concept of a flexible, modular implant with electrodes, electronic circuitry and cables assembled using different modules. (Middle) substrate and electronic components for a multiplexing unit and multiplexer unit after assembly. (Bottom) integration of the stimulator/multiplexer module in a flexible microimplant with a cuff electrode [66]. B) Polyimide-based array is connected via connector board consisting of a ZIF-type connector and a surface mount microsocket to the recording instrumentation [60]. C) Flex-rigid electrocorticography (ECoG) microelectrode array. (Top left) representation of on-wafer microfabricated device, employing gold as electrode and interconnect pad material. (Bottom left) Picture of a fully processed 4" wafer which contains three flex-rigid free-standing ECoG devices spanned to the wafer. (Right) On-silicon, Omnetics connector assembly obtained by solder paste [61]. D) Interconnection of polyimide-based electrodes using anisotropic conductive films. (Top) Schematic of the thin film polyimide electrode, designed to measure EEG signals from the skull surface of a mouse. (Middle) Prior to the main bonding process, the ACF film was laminated onto the PI electrode by a prebonding process. (Bottom) Fully assembled electrode with the PCB connector, connected by the ACF [63].

1.4 Motivation

A major motivation behind this work lies in the increasing demand for flexible microelectrode arrays (MEAs) with electrode technology that can be straightforwardly integrated with electronic modules for stimulation and sensing, easy to maneuver and to connect to the outside. With expansion of medical applications and indications the demand for high density MEAs is, and will be, on the rise. One way to engineer that is by integrating CMOS-compatible materials for electrode manufacturing. Currently, there is a lack of processes for monolithic integration of IC components and flexible, polyimide-based electrodes. Therefore, this work aims at the development of high density flexible MEAs with micron-scale footprint interconnects that can be realized using complementary metal-oxide semiconductor (CMOS) compatible processes and materials. Integration of titanium nitride (TiN) as electrode material in current work is of utmost importance due to its widespread use in IC technology, hence facilitating future integration of electronics for signal multiplexing, filtering or amplification.

This Thesis will pursue the possibility of integrating TiN micro and macroelectrode arrays (6400 μm^2 and bigger) on polyimide substrates and interfacing them with silicon dies that can be used for integration of electronic components and connection to the outside world. Examples of potential applications for such devices are the intracortical microstimulation [38], electrical impedance tomography [40]. A technical solution for manufacturing and assembly of cuff electrodes has been realized and is also discussed in the current Thesis. This solution is of potential interest for researching on peripheral nerves, e.g., vagus and sciatic.

One important challenge in the Thesis work involved processing of on-wafer polyimide devices in a cleanroom environment that is mostly used for processing of CMOS integrated circuits – this inevitably dictated a significant amount of restrictions to avoid cross contamination of machine carriers with polyimide residues. This challenging issue had to be considered in every process step. Significant efforts were also invested in developing the microfabrication process itself, with several challenging steps to be overcome. Finally, electrodes had to be electrochemically characterized and, so, the immense topic electrochemistry had to be studied and learnt.

1.5 Main Contributions

Contributions of this Thesis are: 1) flexible, polyimide-based electrodes that interface with silicon dies, using CMOS and MEMS compatible technologies and materials, 2) use of those technologies for fabrication of “smooth” TiN micro and macroelectrodes on polyimide substrates, allowing future monolithic integration with electronic modules, 3) assembly of planar polyimide foils onto 3D cuff

electrodes, following requirements for *in vivo* use of such devices in acute experiments of the rat vagus nerve, and 4) electrochemical characterization of electrodes by electrochemical impedance spectroscopy (EIS), cyclic voltammetry (CV), and voltage transient measurements (VTM). Figure 1.6 summarizes the achievements listed above with few highlights of the current Thesis.

Several fields of knowledge intersect in the current Thesis: MEMS and CMOS microfabrication technologies for the development of polyimide-based TiN electrodes; materials science to understand interactions between materials at the micrometric scale; principles of electrochemistry that are crucial for electrode characterization, and, also, general notions of anatomy, useful to derive anatomical requirements.

.

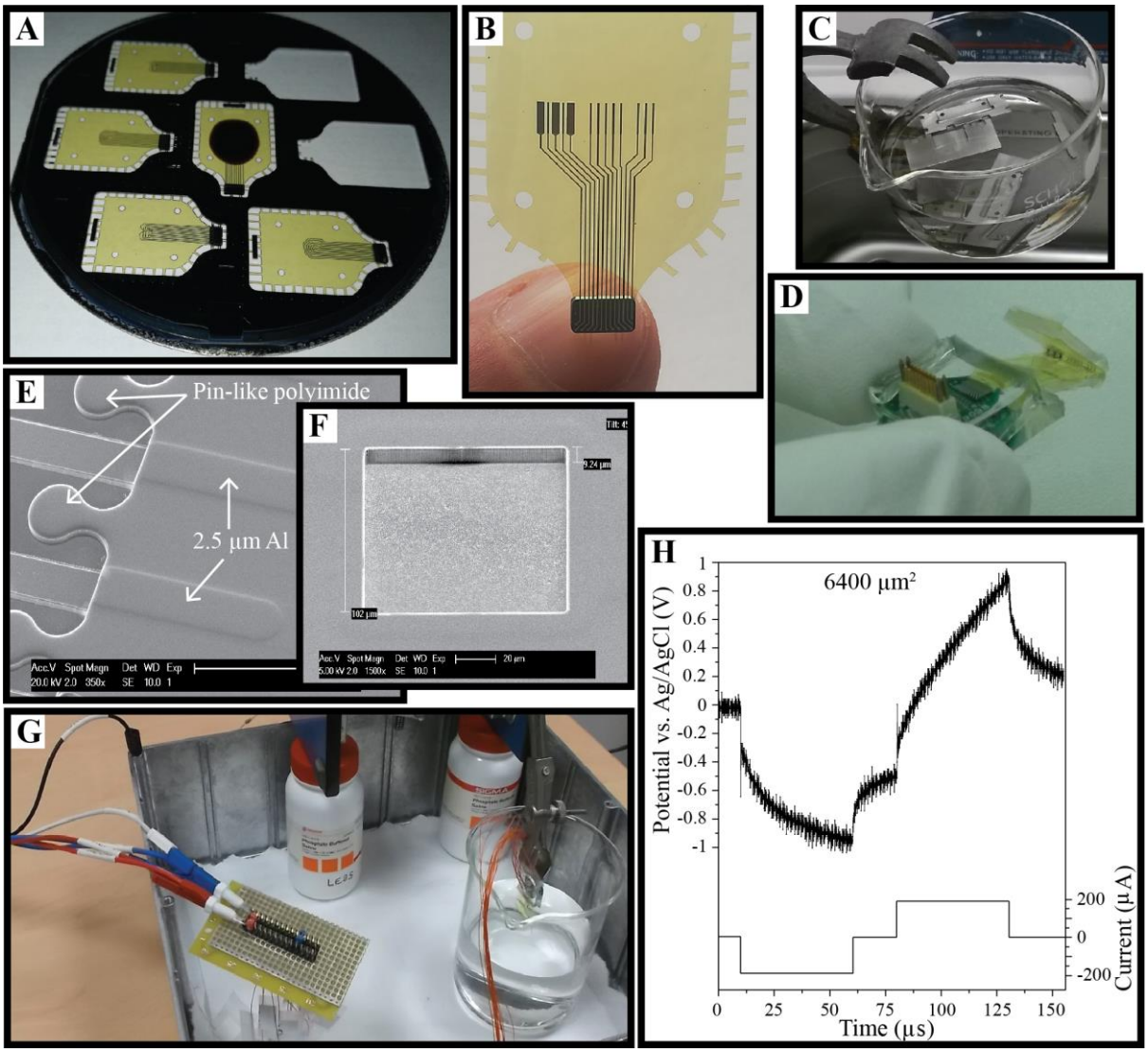

Figure 1.6 A) Silicon wafer after processing with polyimide in yellow – two electrodes have been detached from it, and incomplete silicon etching is observable in the device in center. B) Polyimide-based TiN electrode attached to silicon die with bondpads. C) Stainless-steel mold tools used for cuff molding and assembly, here in isopropanol bath ready for ultrasonic cleaning. D) Split-cylinder cuff after assembly with mold tool. E) SEM picture of a silicon-to-polyimide transition region. Polyimide-free silicon die on the left, and pin-like polyimide structures and metallization are visible on the right. F) SEM picture of an 80 µm × 80 µm TiN microelectrode. G) Experimental setup for electrochemical characterization of electrodes in phosphate buffered solution. H) A voltage transient measurement of an 80 µm × 80 µm TiN microelectrode obtained in PBS with a biphasic, charge-balanced current pulse.

List of publications

F. Rodrigues, P. M. Mendes, L. Gonçalves, M. Bartek, B. Mimoun, R. Dekker, "A Steering Electrode Array for Selective Stimulation of Sacral Nerve Roots" Proceedings ICT.OPEN: Micro Technology and Micro Devices (SAFE 2011), Veldhoven, The Netherlands, pp. 88-91, 2011.

F. Rodrigues, B. Mimoun, M. Bartek, R. Dekker, P. M. Mendes, "Flexible Multipolar Cuff Microelectrode for FES of Sacral Nerve Roots" Proceedings 17th Annual International FES Society Conference (IFESS 2012), Banff, Alberta, Canada, pp. 1-4, 2012.

F. Rodrigues, M. Bartek, P. M. Mendes, "Modeling Workflow for Study of Functional Electrical Stimulation in Peripheral Nerves" Proceedings of the International Conference on Biomedical Electronics and Devices (BIODEVICES 2013), Barcelona, Spain, pp. 178-183, 2013.

F. Rodrigues, P. M. Mendes, M. Bartek, B. Mimoun, A. Fouchard, P. Pham, O. David, "Fabrication and Modeling of a Cuff Electrode for Peripheral Nerve Stimulation" Proceedings 3rd Portuguese IEEE Bio-Engineering Meeting, Braga, Portugal, pp. 1-4, 2013.

F. Rodrigues, P. M. Mendes, "A New Integration Method for Mounting and in vivo Handling of Sub-mm Flexible Cuff Electrode" Proceedings of the International Conference on Biomedical Electronics and Devices (BIODEVICES 2014), Angers, France, pp. 265-270, 2014.

F. Rodrigues, S. Gomes, P. Anacleto, J. Fernandes, P. M. Mendes, "RF CMOS wireless implantable microsystem for sacral roots stimulation with on-chip antenna and far-field wireless powering" Proceedings European Microwave Conference (EuMC 2015), Paris, France, pp. 76-79, 2015.

F. Rodrigues, J. F. Ribeiro, P. A. Anacleto, A. Fouchard, O. David, P. M. Sarro, P. M. Mendes, "Fabrication and characterization of polyimide-based, "smooth" titanium nitride microelectrode arrays for neural stimulation and recording" Journal of Neural Engineering, 17, 1, 016010, 2019.

1.6 Thesis Outline

In this first Chapter, introductory notes concerning several electrode technologies of interest for implantable medical devices are discussed. Here, were presented state-of-the-art solutions for electrodes based on rigid silicon structures, as well as polymer-based arrays. Briefly, some advantages of polymer-based solutions have been discussed in terms of mechanical appropriateness when interfacing with neural tissues. Advantages of using polyimide and titanium nitride as main materials have been discussed. Motivations and main contributions of this Thesis were explained in previous two sections.

Chapter two starts with a brief historical context on the use of electricity to excite nerves. Then we discuss nervous system and early peripheral nerve electrodes. State-of-the-art of electrode technology will be reviewed, being divided in intraneural and extraneural groups. Summaries are provided that put together their geometric features and electrochemical properties.

Chapter three starts with an explanation on why biphasic pulses are typically used in electrical stimulation of nerves and, by inherence, also in electrode characterization. Then, electrodes are discussed in terms of geometric features, e.g., what distinguishes microelectrodes and macroelectrodes, and implications on electrochemical properties. Then, mechanisms of charge injection (from electrode into tissue or electrolyte) are discussed, and a physical rationale is provided for having capacitive profiles being preferred over faradaic ones. Finally, electrochemical methods (EIS, CV, and VTM) are introduced and examples of acquired measurements are given from reference works involving titanium nitride and other materials. It is also discussed how some of these measurements enable discussion and conclusions on the mechanical properties of electrodes like roughness. Works referred in Chapter three are used as references for discussions in Chapter five.

In Chapter four, we will start with studying theoretical limits for bending of polyimide-based films, such as the electrodes in this Thesis. Then, the developed microfabrication process is explained in detail, highlighting the most critical steps and explaining every technical solution that has been engineered. Finally, Chapter four also includes our proposal for manufacturing of cuff electrodes, based on a customized molding process - an imaging of an assembled cuff is shown.

Chapter five is dedicated to electrode measurements. Measurements are provided for micro and macroelectrodes. Throughout this Chapter, various discussions are provided on how our measurements compare with literature on titanium nitride electrodes, what mechanical properties can be inferred from the measurements, and why extreme care is advisable when comparing electrochemical measures among various works. Experimental setups used for the three techniques – electrochemical impedance spectroscopy, cyclic voltammetry, and voltage transient measurements – are explained.

Chapter six will be reserved for final conclusions, and prospects of future work related with this research.

2 Small, Efficient and Adaptive

This Chapter starts with an historical perspective of interaction between nerves and electricity – Section 2.1. Then, basic anatomical principles, important to be considered when designing and developing electrodes for neural stimulation and recording, are presented – Section 2.2. In the same Section, early electrodes for peripheral nerves are discussed. Sections 2.3 – 2.5 are solely dedicated to the state-of-the-art of neural electrodes.

2.1 Nerves and Electricity

The first report on systematic, therapeutic use of electric current for stimulation of nerves is from the mid-1960's, when the creators of the 'gate control' theory of pain, Drs. Melzack and Wall, postulated in their 1965's article in *Science* that innocuous sensory information may suppress the transmission of pain [67]. Although this theory was based on strong experimental findings, clinical confirmation was needed to check its validity. In a follow-up paper called "Temporary abolition of pain in man", published in 1967, Wall and Sweet demonstrated that non-painful electrical stimulation of the peripheral nerve does indeed suppress pain perception in the area that it innervates. In a true spirit of science, they demonstrated it by inserting electrodes into their own infraorbital foramina [68]:

"Needle electrodes insulated except for the tip were applied to our infraorbital nerves; a tingling or buzzing sensation was evoked near threshold in the sensory region of the nerve. It was not unpleasant and always tolerable for an indefinite period. During stimulation and for a few minutes thereafter, pin prick in the tingling area did not feel sharp to either of us."

In their seminal work, few electrode types were tested on different subjects. Apart from needle electrodes inserted in the infraorbital foramina, silastic split-ring platinum electrodes were implanted around the median nerve above the elbow with the leads being run through the skin of forearm.

The electric nature of nervous impulses, as well as the interaction between nerves and electricity, is known since the late 1700's, when Luigi Galvani and his team performed a series of experiments in frogs. By connecting different metals, silver and zinc, to frogs' muscles and nerves, Galvani laid the foundations for two important modern fields in science: electrophysiology and battery technology. Today, educational videos on frog's nerve stimulation, from schools across the globe, may be seen on YouTube.com. One of the most seen is *"The Academy of 21st Century Learning: Electrical Stimulation of Frog Legs"* [69]. It was not until late 1940's and the 1950's, that another set of remarkable experiments

set by the Nobel awardees Alan Hodgkin and Andrew Huxley brought in major advances in the field of neurophysiology. In a series of publications, they have described the mathematical model of the action potential [70]. The voltage-clamp experiments allowed them to record, directly, the ionic currents flowing across the axonal membrane of the giant axon without any resultant change in membrane potential. Another important contribution from them were the mathematical models that predicted excitation of nerve fibers by changing of their extracellular potentials [71].

2.2 Peripheral Nerve Electrodes

2.2.1 The nervous system

Anatomy and physiology of the central and peripheral nervous systems are complex medical topics and surely not subject to a deep analysis in this Thesis. However, as mentioned in Chapter 1, it is of utmost importance to consider anatomical and physiological requirements during the design and development phase of electrodes to interface with structures of the nervous systems. So, a brief introduction to the anatomy of neural structures become of help to demonstrate why and how technologies can be steered to develop innovative neural interfaces.

The nervous system receives information about changes in the body and external environment and transmits messages to the *central nervous system* (CNS). The CNS processes this information and determines what response, if any, is appropriate to the circumstances. The CNS issues commands primarily to muscle and gland cells to carry out such responses. The nervous system has two major anatomical subdivisions – Figure 2.1 A:

- The central nervous system (CNS) consists of the brain and spinal cord, which are enclosed and protected by the cranium and vertebral column.
- The peripheral nervous system (PNS) consists of all the rest; it is composed of nerves and ganglia. A nerve is a bundle of nerve fibers (axons) wrapped in fibrous connective tissue. Nerves emerge from the CNS and carry signals to and from other organs of the body. A ganglion (plural, ganglia) is a knot-like swelling in a nerve where the cell bodies of peripheral neurons are concentrated.

The peripheral nervous system is functionally divided into sensory and motor divisions, and each of these is further divided into somatic and visceral subdivisions. The sensory afferent division carries signals from various receptors (sense organs and simple sensory nerve endings) to the CNS. This pathway informs the CNS of stimuli within and around the body. The motor efferent division carries signals from the CNS mainly to gland and muscle cells that carry out the body's responses. The muscles in the body

are innervated by sensory and motor divisions that arise from spinal nerves and cranial nerves. Spinal nerves arise from the spinal cord and supply branches to muscles below the neck, and cranial nerves arise from the base of the brain and innervate muscles of the head and neck (except for the vagus nerve). The basic functional and also morphological unit of a peripheral nerve is an individual nerve fiber or axon. Each peripheral nerve consists of parallel bundles of nerve fiber, called nerve fascicles. The nerve fibers are protected by Schwann cells and are surrounded and connected by connective tissue (endoneurium, perineurium, and epineurium), what strengthens the peripheral nerves – Figure 2.1 B. One important characteristic of peripheral nerves is their fascicular organization. Fascicles innervating certain muscles are usually bundled together and separated from the neighboring fascicular groups – Figure 2.1 C. These neuroanatomical data have been used to design nerve electrodes for selective control and improve current neural prostheses. In the case of the sciatic nerve that, this is conducive to selective stimulation for isolated and/or balanced dorsiflexion, plantar flexion, eversion, and inversion through a multi-contact nerve-cuff electrode [36].

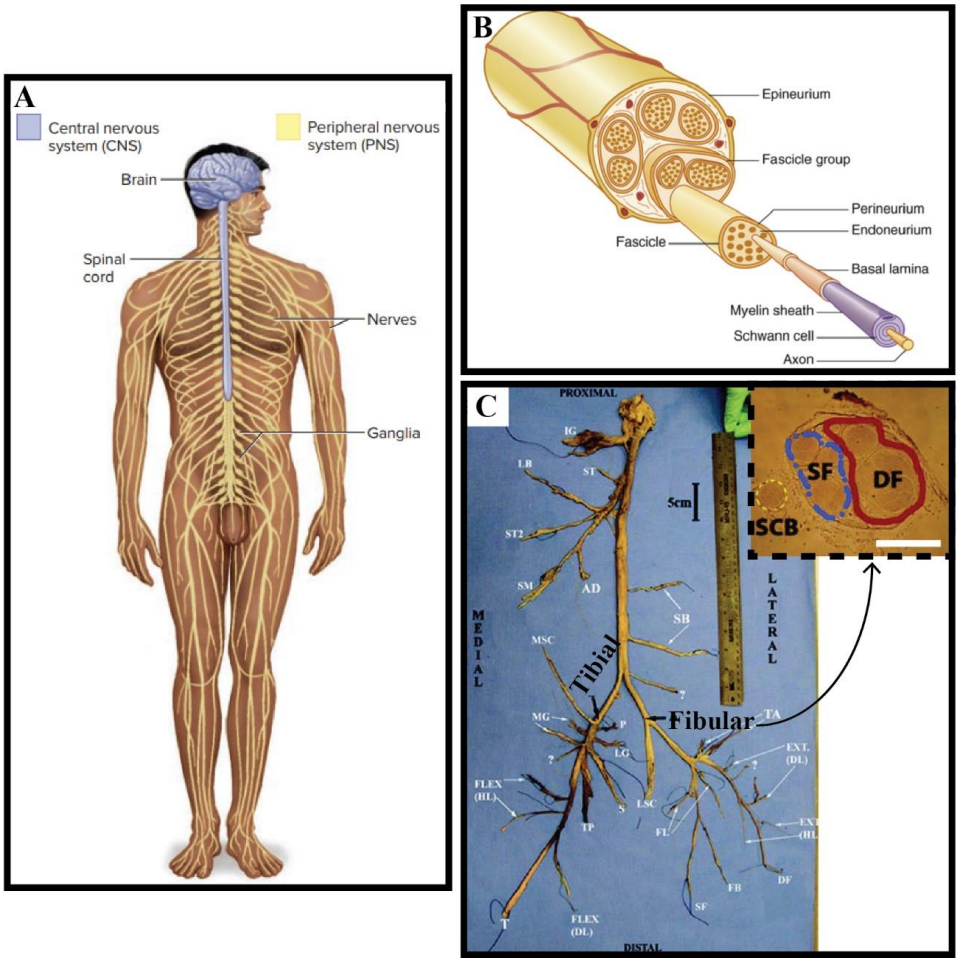

Figure 2.1 The human nervous system. A) Nervous system divided into its central and peripheral components [72]. B) Typical structure of a spinal motor nerve fiber (part of peripheral nervous system). Highlight of the axon as its basic anatomical and

morphological unit, its organization in fascicles, and the 3 layers of connective tissue: endoneurium, perineurium and epineurium [72]. C) Harvested human sciatic nerve with its tibial and fibular branches. (Right) fascicle map of the fibular nerve at the level indicated, showing separation of fascicles corresponding to the superficial fibular (SF) from those of deep fibular (DF). Scale bar: 1 mm [36].

2.2.2 Early PNS electrodes

Unlike the flat, disc-like electrodes in first cardiac pacemakers, mentioned in Chapter 1, initial electrodes for neural stimulation presented a tubular or U-shaped configurations – Figure 2.2 A, B, C. These were developed for clamping or cuffing of large human, peripheral nerves with cylindrical profiles like the sciatic. In its advent during the 1970's, neural stimulation was mainly used for intractable pain, as pointed out in the section above. That was a time when peripheral nerve stimulation surgery could be done only in a few leading centers, primarily due to the lack of commercially available equipment. Although the initial hand-made electrodes have proven effective in many application, they did have drawbacks. Perhaps, the labor intensive to manufacture was one of the most relevant drawbacks. With arrival of silicon and thin film technologies in electrode manufacturing (Figure 2.2 D, E, F) their price went down, and reliability and usability were improved. Number of potential applications has grown dramatically.

2.3 Review and Classification of Electrodes

Fifty years have passed since the experiments of Wall and Sweet, and a wide range of electrodes exist today to interface with the peripheral and central nervous systems, for stimulation and recording. Several review articles have been published over the last fifteen years that offer excellent and diverse overviews on technologies for PNS electrodes. Navarro *et al.* [80] have published a review of interfaces with the PNS focusing on characteristics and suitability of different types of electrodes. They have introduced a useful classification system for PNS electrodes, highlighting the trade-off between selectivity and invasiveness – Figure 2.3. This is discussed in further detail in the next section and examples of electrode technologies are given. In another review of neural interfaces, Grill *et al.* [81] have included the underlying biophysical mechanisms of electrical stimulation and recording at the different levels of the nervous system (PNS and CNS).

They have described different electrode types available and discussed biophysical and biological challenges that are constantly calling for new engineering solutions or adaptation of existing ones. One example of a biological/biophysical challenge given in their study, is the "unforgiving" inflammatory

response of the central nervous system that demands careful consideration about invasiveness and resolution required for a specific application:

"Penetrating electrodes are not always necessary; for example, electroencephalogram (EEG) has been used to obtain signals for a BCI system. Electrocortigram (ECoG) electrodes are placed underneath the skull but above the brain and do not penetrate it; ECoG devices have also been used to gather signals for BCIs. By using surface electrodes to record signals, such arrays may cause a lesser tissue response."

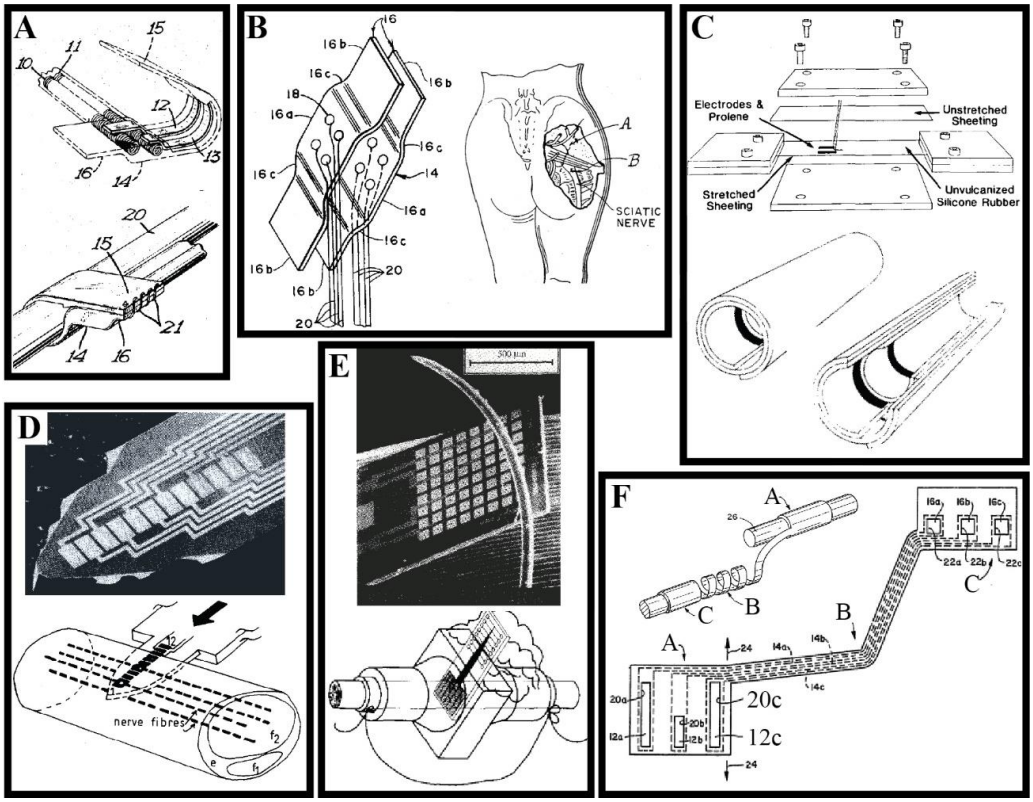

Figure 2.2 Early examples of peripheral nerve electrodes. A) A split-cylinder cuff electrode patented by Hagfors in 1972. Leads (10, 11) connected to independent contacts 12 and 13. Leads and non-exposed parts of contacts are encapsulated in substance (14) inert to body fluids and tissue. Electrode is held in place by sutures (21) [73]. B) Split cuff electrode patented by Avery and Wepsic in 1973, and designed for the sciatic nerve. It is composed of two spacedly opposed strips (16) made of inert plastic material such as dracon mesh reinforced with silicone rubber. Stainless steel wires (20) are coupled to platinum lead wires. Electrode is held by sutures. [74]. C) The Case Western Reserve University (CWRU) spiral cuff electrode designed to facilitate surgical handling without the need for fixation sutures – patented in 1986 [75] and published in 1988 [76]. It is manufactured by bonding together two sheets of flexible insulation with electrodes sandwiched between them. Electrodes are placed on the stretched sheet, and, upon release, the electrodes face interior of the cuff. D) An early rigid, silicon-based microelectrode array with 12 platinum contacts (10 x 50 μm), and using low pressure chemical vapor deposition insulating Si_3N_4 (silicon nitride) between contacts [77]. E) A silicon-based sieve microelectrode array for invasive implantation in the sciatic nerve. It uses iridium as electrode material, Si_3N_4 as insulator, and it has probe pads interconnected [78]. F) Thin film electrode patented by Grill *et al.* A sheet of polymeric material defines a cuff portion (A), a contact portion (B), and an interconnecting elongated lead portion (C). Using physical vapor deposition (PVD), chemical vapor deposition (CVD), or other thin film

deposition techniques, a plurality of electrodes (12), contacts pads, and interconnecting leads are deposited on the base layer. Windows (20) are defined in the elastomeric portion to provide for electrical conduction between the electrode and the nerve tissue [79].

A careful evaluation of which interface to use is done by the personnel involved, e.g., clinician, researcher, electrophysiologist. As pointed out by Grill *et al.* highly selective electrodes that penetrate the neural tissue and are placed very closely to targets are not always desirable. Other reviews of technologies for manufacturing electrodes for neural stimulation focus on state-of-the art polymers and the advantages in using these compliant materials instead of rigid ones [43, 82].

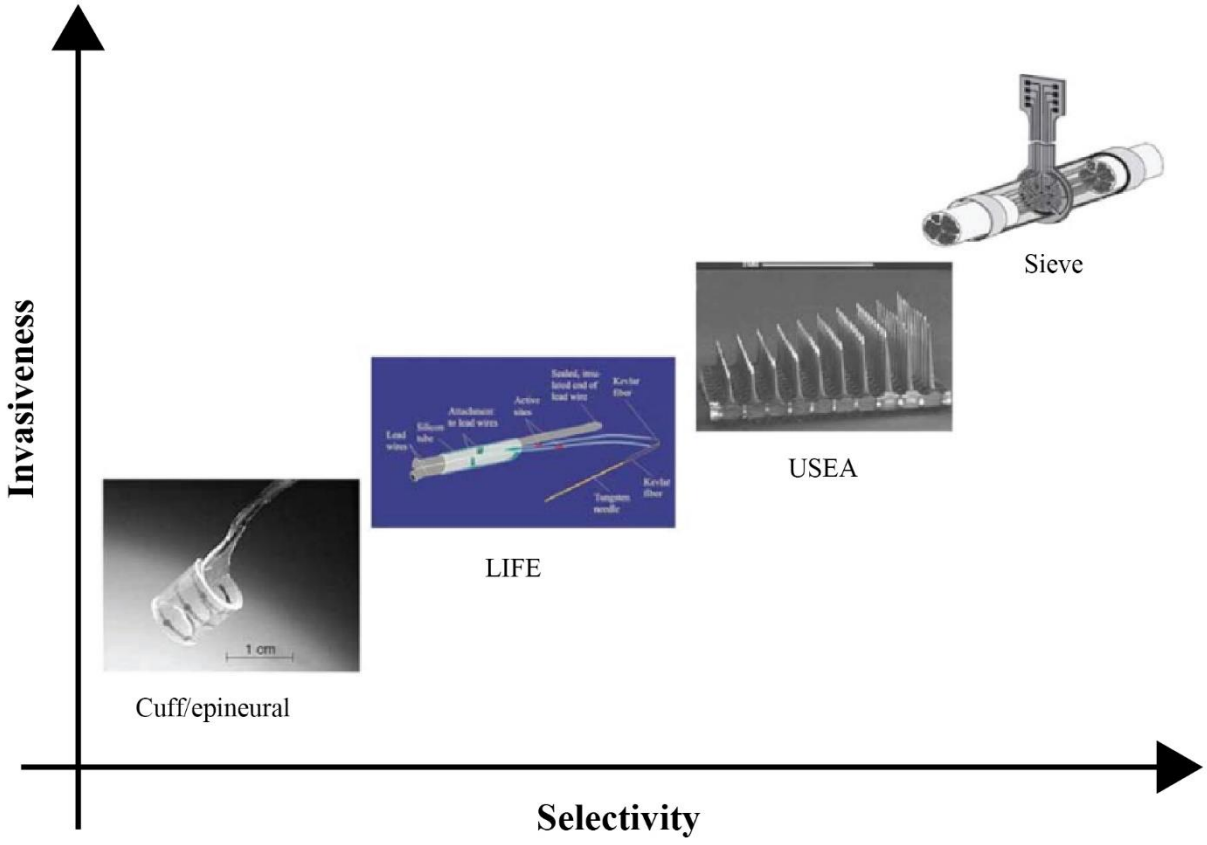

Figure 2.3 Examples and classification of electrodes to interface with the peripheral nerves depending on invasiveness and selectivity. Adapted from [83-84]. In order of increased selectivity and invasiveness: hybrid silicone-polyimide cuff electrode, polyimide thin film longitudinal intrafascicular electrode (tf-LIFE), silicon-based Utah slanted electrode array, and polyimide sieve electrode.

Because selectivity is obtained at the cost of invasiveness, reviews of neural interfaces for the central nervous system usually have a strong focus on tissue responses, where it has shown to be critical [85-86]. Electrodes cannot be easily categorized into CNS or PNS interfaces. Indeed, throughout the history of neural stimulation, electrode designs that have been first proposed as interfaces with the PNS, have later been adapted and used in CNS applications. And vice versa. The silicon-based Utah

microelectrode array with 100 separate channels was first introduced for single unit recording in the cortex [87], but was later adapted to be the Utah slanted electrode array (USEA) and extensively used in PNS applications [28-29]. On the contrary, planar thin film polyimides have first been introduced for sieve electrodes [88] and cuff assemblies [89] that interfaced with the peripheral nerves, but are now used in CNS applications, as substrates for micro-LEDs stimulators [53] or graphene electrodes [50].

In the following two Sections, 2.4 and 2.5, state-of-the-art electrodes are reviewed based on a simplified version of Navarro's classification system: intraneural and extraneural. In the end of each Section, a table summarizes most relevant features of each electrode. Our main goal in the next two Sections is to discuss electrochemical performance of electrodes, based on the following figures of merit: a) impedance magnitude at 1 kHz, and b) charge injection capacity (CIC) or Q_{inj}. These are two commonly accepted ways for assessing recording (impedance) and stimulation (Q_{inj}) capabilities of neural electrodes. *In vivo* uses of intraneural, extraneural and polyimide-based microelectrodes, secondly to our primary goal, will be discussed when necessary. Further details on electrochemical behavior of electrodes for neural stimulation and recording will be discussed in Chapter 3.

2.4 Intraneural Electrodes

Intraneural electrodes are placed within the nerve and are in direct contact with the tissue they are intended to activate or record. Stimulation through them has the potential to active target fascicles with minimum cross-talk to adjacent and non-target fascicles. Intraneural electrodes penetrating the epineurium can go to as far as penetrating the perineurium (intrafascicular) or not (interfascicular). Examples of intraneural electrodes include the Utah microelectrode array, the longitudinal intrafascicular electrode (LIFE), the transverse intrafascicular electrode (TIME), and the regenerative sieve electrode.

2.4.1 Utah microelectrode arrays

The Utah MEA (or UEA), introduced in 1996 for single unit recording from the cortex [87] and later used in electrical stimulation of peripheral nerves [28, 90], is a matrix of "needles" that project out of a common substrate. Each needle is one electrode contact and it is electrically isolated from its neighboring electrodes by a glass "moat". Utah microelectrode arrays are formed by micromachining and photolithographic techniques (e.g., dicing, metallization, wet etching), but their design (number and length of contacts, pitch) and materials used vary among different studies. The device presented in 1996 by Nordhausen *et al.* [87] had a 10 × 10 grid of needles equally projecting 1.5 mm above a 4.2 × 4.2 × 0.2 mm^3 thick substrate. The inter-electrode spacing (pitch) in the array was 0.4 mm. The needles were insulated with polyimide except for the tips that were metallized with platinum to form contacts, yielding

average impedances of 80 kΩ at 1 kHz. In 2010, Negi *et al.* [91] have proposed a similar 10 × 10 grid with 1.5 mm long needles as UEA design, however using parylene-C as insulator, and sputtered iridium oxide (SIROF) and activated iridium oxide (AIROF) as electrodes – Figure 2.4 A. Impedances at 1 kHz of 5000 μm^2 microelectrodes were found to be 8 and 10 kΩ, respectively for the SIROF and AIROF. Charge injection capacity was 1 mC/cm^2 and 0.5 mC/cm^2, for SIROF and AIROF respectively. The work of Negi *et al.* is part of a summary state-of-the-art of microelectrode arrays for neural stimulation and recording presented in Table 2.1. In 2013, Wark *et al.* [29] presented a high-density Utah slanted electrode array (HD-USEA) characterized by needles of varying lengths (from 300 to 800 μm long) and with smaller pitch (0.2 mm) – Figure 2.4 B. Impedances of SIROF tips were 440 ± 340 kΩ and 179 ± 216 kΩ, for electrode areas of 297 and 4367 μm^2, respectively. The UEA has been developed by Blackrock Microsystems® into a commercial, off-the-shelf product for neuroscience research in humans, non-human primates and rodents [92]. In their 2016 study in humans with amputation of upper extremities, Davis *et al.* [93] have used the 100-needle Blackrock's UEAs to elicit hand sensory feedback by microstimulation (4-12 nC/phase) of the ulnar and median nerves. Impedance at 1 kHz of electrodes ranged 20-130 kΩ (*in vitro*) and 70-350 kΩ (*in vivo,* 30 days post-implantation). In 2018, a study with 16-needle Blackrock's SIROF UEAs implanted in the cortex of rodents has shown that after a one week implantation, electrodes exhibited a 1 kHz impedance magnitude of 425 kΩ (12 kΩ *in vitro*) and were able to deliver a charge of 4 nC/phase [94].

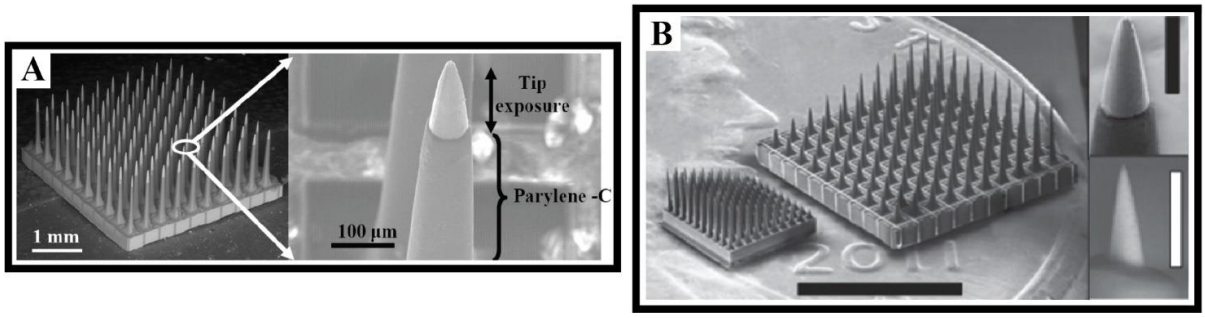

Figure 2.4 Utah microelectrode arrays. A) Scanning electron micrograph of a UEA used for studying electrochemical properties of SIROF and AIROF. The UEA is encapsulated by an insulating Parylene-C layer, with the exception of the tip of the electrode which forms the active site for stimulation and/or recording of neural signals. Electrically active areas in the tips range between 3100 and 6200 μm^2 [91]. B) A scanning electron microscopy (SEM) image of the conventionally spaced USEA with 0.4 mm pitch and needles ranging between 200 and 1500 μm (larger device atop a US penny). The HD-USEA with 0.2 mm pitch and needles ranging between 300 and 800 μm (left). Scale bar = 3 mm. (Top right) inset SEM parylene-C insulation removed using an oxygen plasma etching on 50 μm (geometric surface area, GSA = 4367 μm^2. Scale bar = 50 μm. (Bottom right) removal of parylene-C using a hybrid excimer laser and plasma etching technique (GSA = 297 μm^2). Scale bar = 25 μm [29].

2.4.2 Longitudinal intrafascicular electrodes (LIFEs)

The longitudinal intrafascicular electrode (LIFE) is an intraneural electrode that penetrates the perineurium (connective tissue around each fascicle) and it can be set inside individual fascicles of a given nerve. In 1991, Nannini and Horch have introduced LIFE for selective stimulation in a peripheral nerve [95]. By inserting a 25 μm diameter tube, with two stimulation points with areas of 0.8 mm^2, inside the largest fascicle of a cat sciatic nerve, graded muscle recruitment could be achieved with an average charge of 4 nC per phase. The first LIFEs were constructed using platinum or platinum-iridium core wires with outer insulation that is locally removed for creating electric contacts, and were found to produce mild degrees of nerve damage [96]. LIFEs based on polymer core fibers (e.g., Kevlar fibers) instead of on Pt or PtIr wires, and known as PolyLIFEs, used sputter-deposition of titanium, gold and platinum and were insulated with silicone for better mechanical fit to the fragile peripheral nerves [97] [98]. A significant step forward in implantable LIFEs happened with the development of thin film LIFEs (tfLIFE) based on polyimide [99-100] – Figure 2.5. The main advantages of polyimide-based LIFEs over wire-based or polyLIFEs (Kevlar) are flexibility and lower mechanical mismatch between nerve and electrode, high number of stimulation/recording contacts, and miniaturization. As LIFEs are implanted along the nerve trunk and are therefore parallel to fascicles and individual nerve fibers, they are not particularly effective in delivering selective stimulation to different muscle groups. Not surprisingly, Kundu *et al.* [100] have reported in their comparative study from 2014 that the transverse intrafascicular electrode (TIME) is able to recruit more muscles with higher selectivity than tfLIFE. Clinical relevance of LIFEs has been almost exclusively linked to restore the natural tactile sensory feedback through peripheral neural interfaces. In their breakthrough study from 2010, Rossini *et al.* [101] have used tfLIFEs with 8 platinum contacts with area of 4000 μm^2 to elicit hand sensory feedback by stimulation of the median and ulnar nerves. Electrochemical characterization of these tfLIFEs have shown impedances at 1 kHz between 5.5 and 7.5 kHz, and a charge injection capacity of 750 $\mu C/cm^2$ [102] – part of summary in Table 2.1.

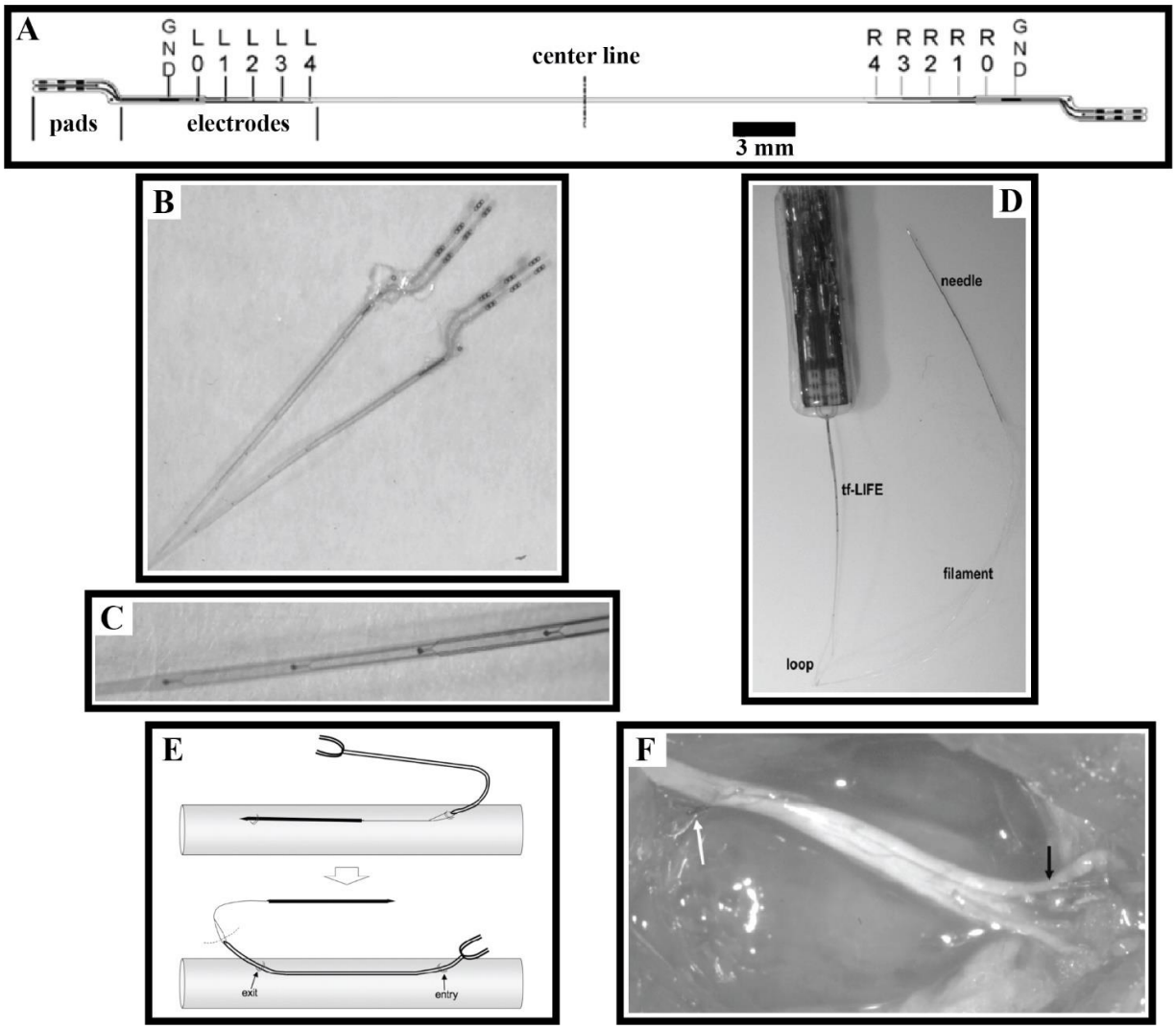

Figure 2.5 Thin film longitudinal intrafascicular electrode (tfLIFE) [99]. A) Schematic of the tfLIFE. Each half of the structure has a ground electrode (GND), an indifferent electrode (L0, R0) and four recording sites (L1-4, R1-4). B) The tfLIFE is folded by the central line, so both branches can be closely apposed. C) Higher magnification view showing the four active sites made by platinum sputtering. D) Photograph of the whole system. The tfLIFE is attached proximally to a ceramic connector for nerve recording/stimulation and distally to a tungsten needle used for surgical implantation. E) Schematic illustrating the surgical implantation of a LIFE. The tungsten needle is threaded along the nerve and then used to pull the electrode linked by the Kevlar filament. The tungsten needle is pulled out leaving the electrode inside the nerve. The needle is removed by cutting the Kevlar filament (dashed line). F) Photograph of the rat sciatic nerve with a tfLIFE implanted. The portions of the LIFE at the entry (black arrow) and exit (white arrow) were secured in place by means of suture to the epineurium.

2.4.3 Transverse intrafascicular multichannel electrode (TIME)

The transverse intrafascicular multichannel electrode (TIME) was first introduced in 2010 by Boretius *et al.* [30]. TIMEs were designed to be implanted into the nerve transversally, thereby accessing different subgroups of nerve fibers – Figure 2.6 A, B. To minimize mismatches in mechanical properties between device and nerve tissue, TIMEs are made flexible by using polyimide and parylene-C as substrate materials – Figure 2.6 C, D, and E. TIME by Boretius *et al.* had 10 contacts on polyimide substrates with 60 µm diameter, and platinum and platinum black were used as electrode contact materials. Platinum presented an impedance of 27 kΩ *in vitro* (CIC between 60 and 80 µC/cm^2) and 39 kΩ *in vivo*, while the platinum black exhibited 11 kΩ in both conditions (CIC between 201 and 230 µC/cm^2). In their study, acute experiments in rat sciatic nerves have shown selective stimulation of different fascicles, and maximum muscle force could be achieved with charge densities below 70 µC/cm^2 (20 µs pulsewidth). TIME properties are summarized in Table 2.1. In their 2014 study, Raspopovic *et al.* [103] have used the TIMEs described above to stimulate the median and ulnar nerve fascicles and physiologically appropriate sensory information could be provided to an hand amputee during the real-time decoding of different grasping tasks to control a dexterous hand prosthesis. This feedback enabled the participant to effectively modulate the grasping force of the prosthesis with no visual or auditory feedback. In 2012, Boretius *et al.* [104] have proposed polyimide-based TIMEs with sputtered iridium oxide (SIROF) as electrode material, and much higher charge injection capacities could be achieved (2.3 mC/cm^2) – Table 2.1. Injection capacities of different electrode materials are discussed in Chapter 3. In 2017 Mueller *et al.* [105] have proposed a new microfabrication method to manufacture TIMEs based on parylene-C substrates, and using platinum iridium alloy (with and without platinum coatings) as electrodes. The coating applied was platinum nanograss and it was deposited using a chemical reduction reaction [106], and enabled an increase in CIC of from 198 (PtIr) to nearly 753 µC/cm^2 (PtIr with Pt nanograss), nearly a four-fold increase.

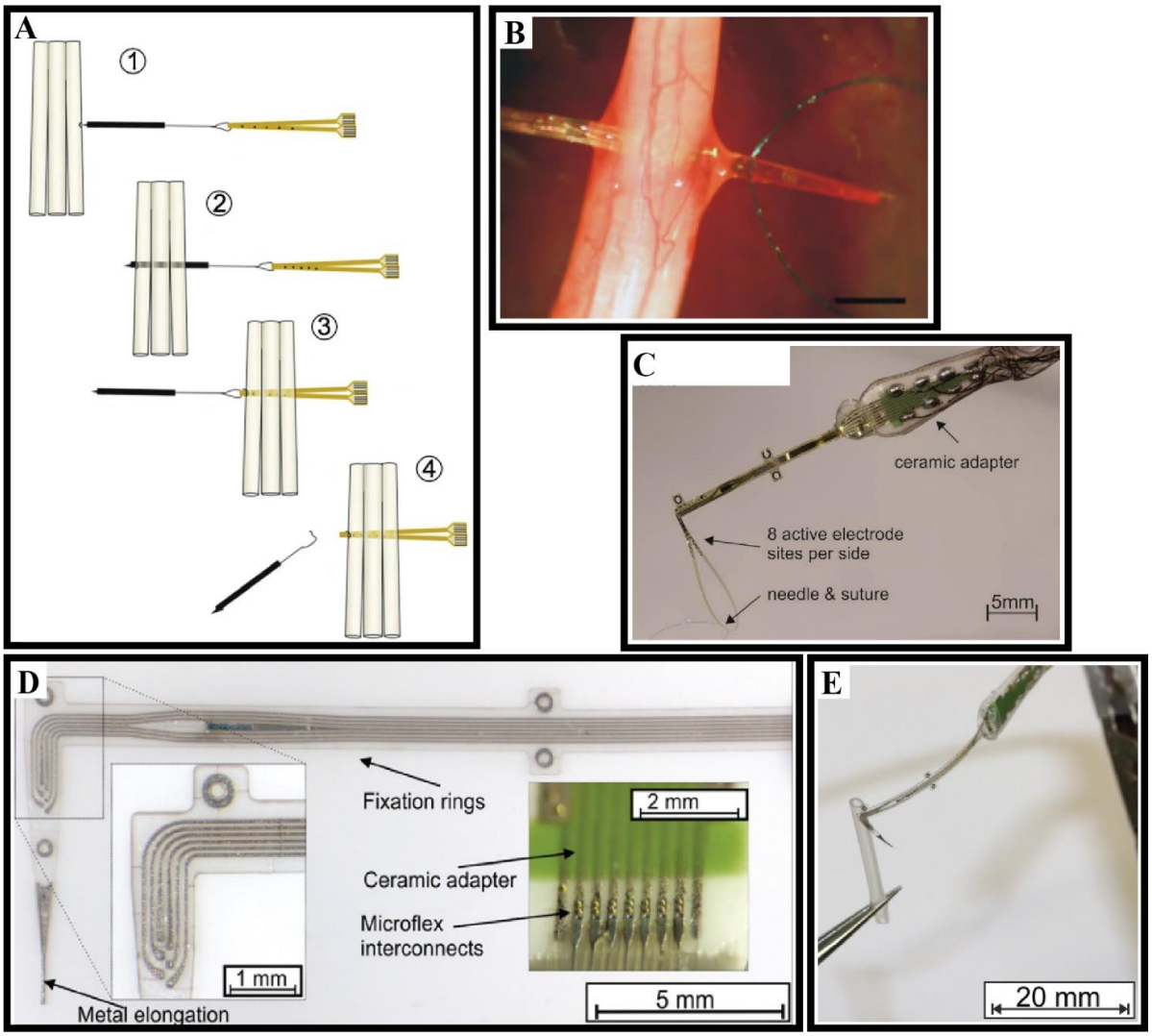

Figure 2.6 Transverse intrafascicular multichannel electrode (TIME). A) Schematic view of the implantation procedure of a TIME: (1) the folded device is passed around the loop of suture; (2) the needle is inserted transversally through the three branches of the sciatic nerve and (3) is used to pull the electrode through it; (4) after positioning the electrode in the nerve tissue, the substrate is fixed via a droplet of fibrin glue [30]. B) Photograph of the rat sciatic nerve with a thin film polyimide-based TIME device transversally implanted. Scale bar = 1 mm [30]. C) Detailed picture of a thin film polyimide-based TIME, its ceramic adapter, needle and suture [104]. D) Optical image of a parylene-C based intrafascicular electrode array with 6 electrode contacts and one ground electrode. Close up of the Microflex interconnects to a ceramic adaptor. Metal elongation is used to pierce through the nerve [105]. E) Photo of the assembled device shown in D.

2.4.4 Regenerative electrodes

A slightly different approach to interfacing with nerves involves the ability of peripheral nerves to regenerate following deliberate or traumatic transection. The basic idea is to provide a mechanical (and biocompatible) structure that outgrowing nerve fibers can grow into or through. Such structures are known as regenerative electrodes and can have two different shapes: sieves and microchannels. A sieve electrode, as the name implies, consists of an array of holes or channels that are formed on a thin substrate that is positioned at the end of a transected nerve. Some or all of the holes are surrounded by an electrode contact for recording and/or stimulation. Ideally, the severed axons of the nerve regenerate through the holes of the sieve, and, in so doing, become well anchored to the sieve structure to provide an enduring, stable neural interface. Sieves are typically fabricated from micromachined silicon [107], or polyimide [108-109]. The low amplitude extracellular currents that the nerve action potentials generate are strongest at the nodes of Ranvier. When using sieve devices much of the activity present can go unrecorded, because nodes of Ranvier fall outside of the device. This drawback can be mitigated by allowing nerve fibers to regenerate through much longer holes which are generally referred to as microchannels and which physically separate and electrically isolate the fibers in one channel from those in neighboring channels – Figure 2.7. A major advantage of the microchannel approach is that electrodes can be located within each channel, and because the action potential currents are constrained to travel within the electrically insulated channels, the recorded signal amplitudes are greatly increased. Likewise, the increased extracellular resistance enhanced by confinement of axons in microchannels is very beneficial for their stimulation. Several substrate materials have been used for microchannel arrays like polyimide [110], PDMS [111-112] , or combination of polymers like PDMS and SU-8 [113]. In their 2009 study, FitzGerald *et al.* [111] have shown that very low charge (1 μA over 50 μs = 0.05 nC) is required to stimulate action potentials within 110 μm diameter microchannels. This means that a microelectrode as small as 10 μm × 10 μm (area 100 μm^2) in the wall of a microchannel would require a CIC of just 50 $\mu C/cm^2$. This charge requirement is well within the capability of "purely" capacitive electrode materials such as anodized tantalum [114]. Because stimulation currents delivered inside an insulated microchannel are restricted to that microstructure and to its axons (limited spread to other structures), selectivity of regenerative microchannels is maximized for stimulation as well as for recording.

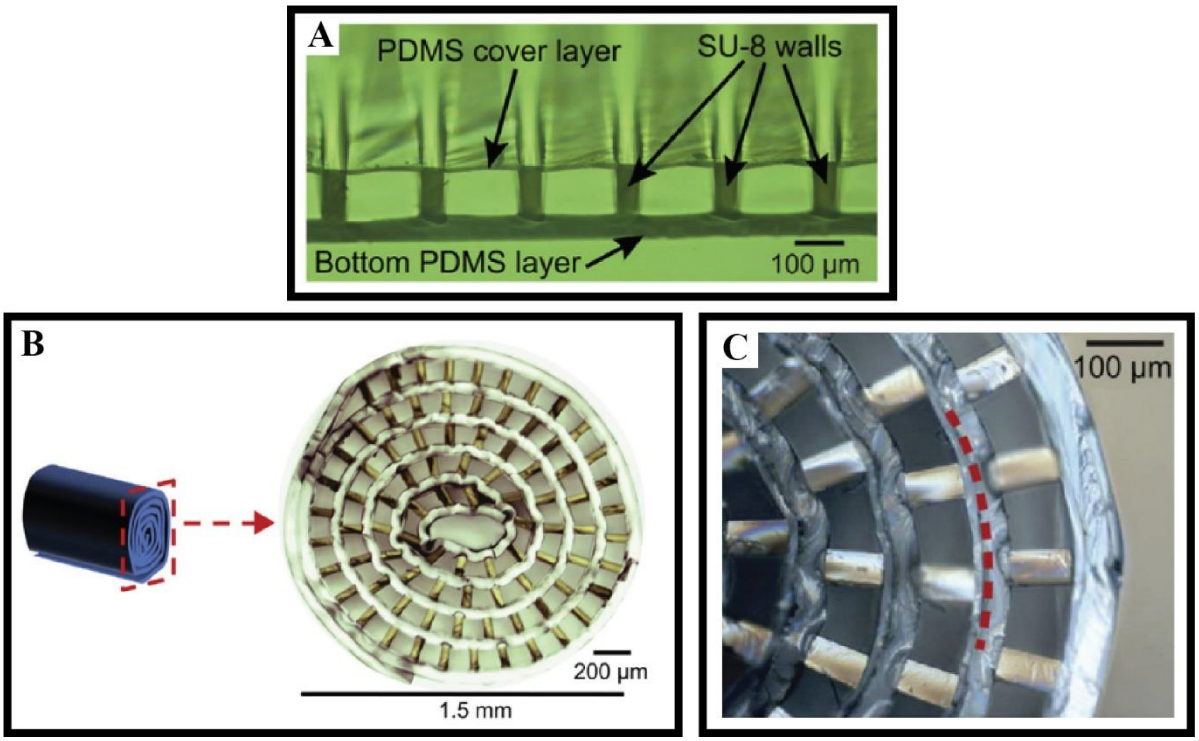

Figure 2.7 Regenerative microchannel electrode [113]. A) Image of microchannels with the PDMS cover layer adhered to the SU-8 walls. B) Cross-sectional view of 100 µm × 100 µm microchannel scaffold rolled for implantation in a rat sciatic. C) Close up of rolled microchannel scaffold showing neighboring microchannel layers delineated by a red line.

Table 2.1 Intraneural microelectrode arrays for neural stimulation and recording: State-of-the-art.

Electrode design	Number of contacts Geometric surface area (GSA)	Materials: electrode and insulator	Impedance @ 1 kHz	Charge injection capacity (CIC) or Q_{inj}	Year
Utah	100 contacts 3100 - 6200 μm^2	Contacts AIROF, SIROF Insulator Parylene-C	10 kΩ PBS	SIROF 1 mC/cm^2, AIROF 500 $\mu C/cm^2$ (600 µs pulsewidth)	2010 [91]
tfLIFE	8 contacts 40 µm × 100 µm = 4000 μm^2	Platinum Polyimide	5.5 – 7.5 kΩ *in vitro*	75 $\mu C/cm^2$ (300 µs pulsewidth)	2010 [102]
TIME	10 contacts Ø 60 µm = 2826 μm^2	Platinum, Platinum-black Polyimide	Pt 27 kΩ *in vitro* 39 kΩ *in vivo* Pt-black 11 kΩ	Pt 60-80 $\mu C/cm^2$, Pt-black 201-230 $\mu C/cm^2$ (20 µs pulsewidth)	2010 [30]
TIME	16 contacts Ø 80 µm = 5024 μm^2	SIROF Polyimide	~ 10 kΩ PBS	2.3 mC/cm^2 (200 µs pulsewidth)	2012 [104]
TIME	6 contacts Ø 80 µm = 5024 μm^2	PtIr alloy, alloy + coating Parylene-C	44 kΩ alloy no coating, 6 kΩ coating PBS	198 $\mu C/cm^2$ no coating, 753 $\mu C/cm^2$ coating (200 µs pulsewidth)	2017 [105]

2.5 Extraneural Electrodes

Surgically implanted outside the nerve epineurium, extraneural electrodes are considered as non-invasive neural interfaces. The non-invasive denomination originates in the fact that extraneural electrodes are designed to preserve the connective tissues that encompass peripheral nerves. However, it is known that extraneural electrodes exert pressures on nerves and tissue damage can occur via compression and blood flow occlusion, resulting in degeneration and demyelination of axons [115]. The two types of extraneural electrodes to interface with peripheral nerves are the cuff electrodes and the flat interface nerve electrodes (FINEs).

2.5.1 Flat interface nerve electrodes (FINEs)

Functionality of FINEs is based on their ability to reshape peripheral nerves into rectangular, flat shape [116]. In fact, nerves can withstand application of small forces, as long as the electrode is able to expand or reshape to accommodate the increased nerve size. The FINE applies forces only on two sides of the nerve, reshaping the nerve into an elongated oval, which has a much larger surface area for any

given volume of nerve tissue. The FINE allows swelling by changing from an oval to circular shape. This simple change in geometry accommodates a larger volume of tissue and fluid without changing the overall electrode circumference, and increases the surface area of the exposed nerve, offering greater access to fascicles which would otherwise be surrounded by adjacent fascicles. In 2002, Tyler and Durand introduced the concept of a flat interface nerve electrode (FINE) [116], and have shown that reshaping of cat sciatic nerves is possible as well as selective stimulation of individual fascicles with independent contacts. Later, FINEs have been used for selective stimulation in other peripheral nerves like the hypoglossal [117], femoral [22], tibial and peroneal [23], ulnar and median nerves [118]. Housings are molded with a low viscosity silicone rubber, and depending on nerve dimensions, the height, width and depth of FINEs can be adapted – Figure 2.8A. For the femoral nerve and nerves of upper extremities (ulnar and median), FINEs are 10 mm wide × 1.5 mm high, while for the tibial and peroneal nerves, FINEs of different (width × length): 15 mm × 1.5 mm, 10 mm × 1.5 mm, 10 mm × 1.0 mm were used. Platinum iridium contacts are laser cut and secured to independent multistranded stainless steel Teflon-insulated lead wire [22-23]. Electrode contacts in the FINEs have areas around 0.2 mm^2, i.e. 200 000 μm^2, which makes them macroelectrodes. The distinction between macroelectrodes and microelectrodes is addressed in the Chapter 3. Recently, in 2017, an updated version of FINEs has been presented, based on a composite silicone with PEEK polymer reinforcements (C-FINE) – Figure 2.8 B.

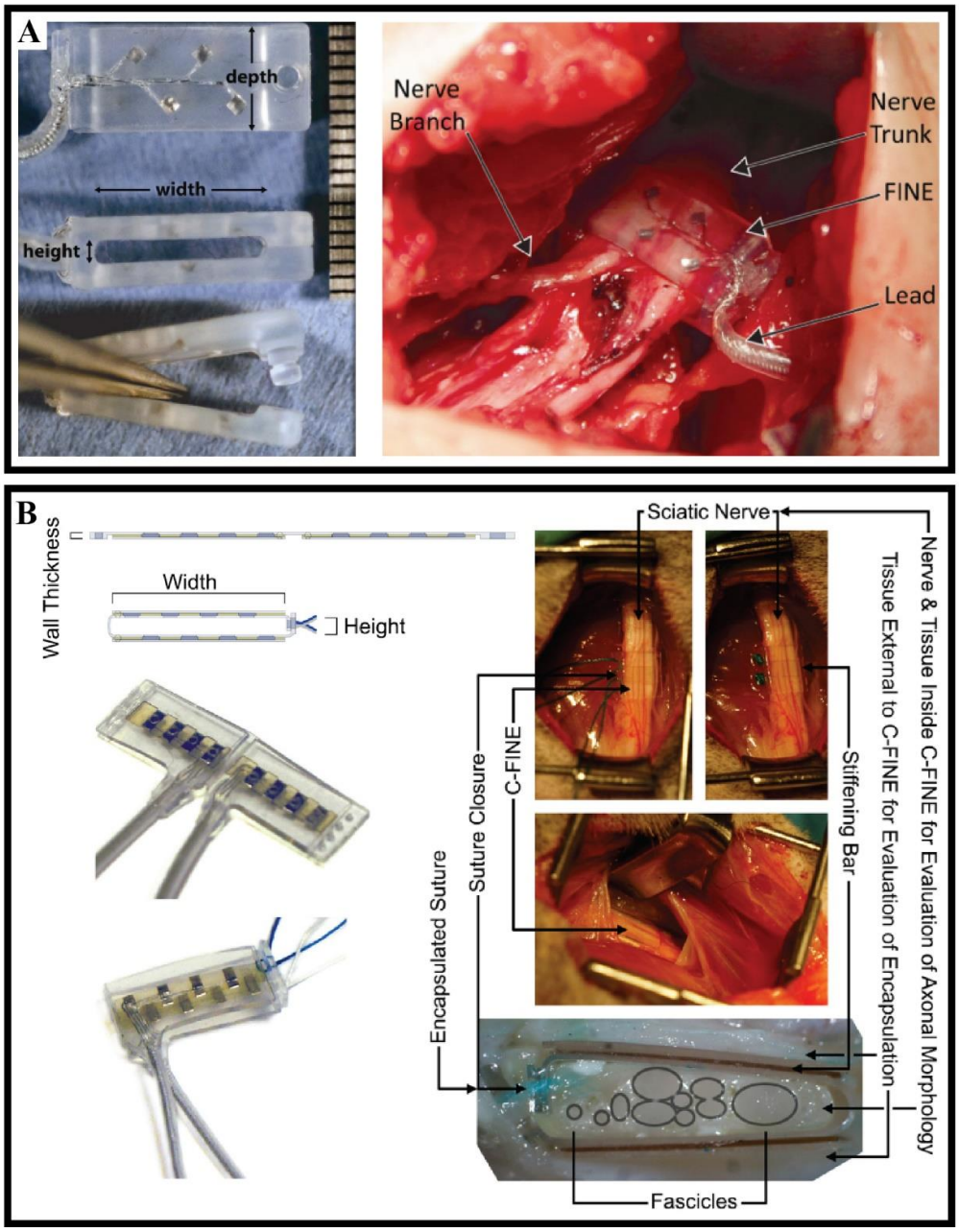

Figure 2.8 Flat interface nerve electrodes (FINEs). A) (Top left) contacts are offset to maximize the spatial volume that can be stimulated. (Middle) side view shows the lumen through which the nerve passes. (Bottom) shows the open FINE and the button designed to keep the FINE closed. Scale on right is in mm. (Right) A 10 mm × 1.0 mm FINE placed around the left peroneal nerve [23]. B) Diagrams and pictures of C-FINEs. (Top left) diagram of an open C-FINE from a side view. (Middle) closed C-FINE from a side view. (Bottom) examples pictures of the C-FINE, open as well as closed. (Right) surgical pictures of C-FINE implant, explant, and cross section. Examples show implant on cat sciatic nerve (top) as well as the same cuff at explant (middle) and a cross section after fixation (bottom) [119].

2.5.2 Cuff electrodes

Cuff electrodes have been successfully used as an interface with the peripheral nerves for nearly 50 years now, as shown in the Subsection 2.2.2 of this Chapter: "Early PNS Electrodes". In general, cuffs consist of several stimulation sites, or electrode contacts, of various sizes embedded within 2 sheaths of a biocompatible and insulating polymer material. As shown in Section 2.3, first cuff electrodes were designed in a split-cylinder configuration, usually comprising two halves or two parts that are brought closely together and fixed during surgery. In 1988, Naples *et al.* [76] have introduced a new concept of cuff electrode called spiral, designed to be expandable so that it could be sized to fit snugly around a nerve and/or accommodate neural swelling. Cuff electrodes can then be classified in two types or designs, according to their geometry: split-cylinder and spiral [76] – Figure 2.9. In an important study, Cuoco and Durand have determined that cuff electrodes (spirals and split-cylinders) could not generate enough pressure to occlude blood flow even if the nerve swells to 133% of its resting diameter [120]. This was an important finding because encapsulation and scar tissue that can grow between the nerve and the cuff after implantation can cause increases in nerve diameter up to 133% of the nerves pre-implantation diameter [76]. In their study from the year of 2000, Cuoco and Durand have also summarized a set of equations that predict build-up pressures on nerves due to cuff structures (split-cylinders and spirals), and have validated them with experimental data. These equations are shown below.

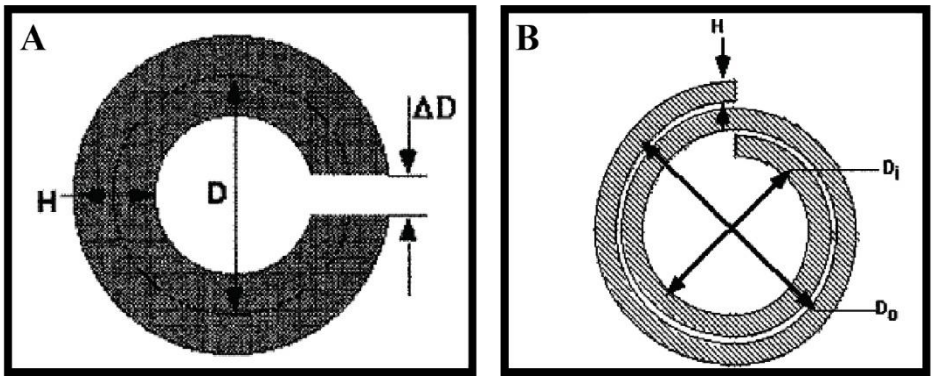

Figure 2.9 Cuff electrodes. A) Split-cylinder cuff. B) Double wrap spiral cuff [120].

$$\Delta P_{\text{split-cylinder}} = \frac{EH^3 \Delta D}{2.25 D^4} \tag{2.1}$$

$$\Delta P_{\text{spiral}} = \frac{EH^3 \Delta D}{2.25\left(D_i^4 + D_o^4\right)} \tag{2.2}$$

where ΔP is the pressure exerted by the cuff, and it is directly proportional to the Young's modulus (E) of the cuff material, electrode's wall thickness (H), and the difference between the nerve diameter and the

cuff internal diameter (ΔD). In 2.1, D is the cuff mean ring diameter, whereas in 2.2, D_i is the cuff mean inner ring diameter and D_o is the cuff mean outer ring diameter. Cuff materials – insulating and conductive layers – their thicknesses and Young's moduli are therefore important parameters to consider when designing cuff electrodes. From this, it is highlighted the importance of matching these properties, by using flexible or stretchable materials, like polyimides or PDMS as electrode materials.

As shown earlier, early spiral cuffs by Naples *et al.* [76] were manufactured by bonding together two pieces of silicone rubber sheets having different natural resting lengths. The shorter piece is fixed in a stretch state until it can be bonded to the longer and un-stretched piece. In 2000, a new process for realizing spiral cuffs based on polyimide thin films has been introduced by Rodriguez *et al.* [89]. Microfabrication techniques were employed to realize flexible polyimide sheets with embedded platinum contacts. The whole structure had a thickness of 10 μm and a weight of 5 mg. The curling of polyimide sheets into 3D cuff structures was obtained by using a heating/tempering process with a customized tool for giving polyimide a spiraling shape. After tempering, cuffs can be released from the tool. In their work, polyimide-based spiral cuffs were manufactured with 1.7 mm diameter, a length of 12 mm, and 3 round, 360° contacts spaced by 5 mm – Figure 2.11A. After curing of first layer of polyimide, the metallization (30 nm titanium, 300 nm platinum) for the contact pads, the interconnect lines, and electrode sites was deposited by sputtering. Reactive ion etching (RIE) was used to open the sites where the platinum must remain exposed, i.e. the electrode sites and the contact pads. The work of Rodriguez *et al.* represents a pinnacle in the history of peripheral nerve electrodes, as polyimide cuffs have lower volume (and lower thicknesses) and higher reproducibility than silicone cuffs, and can be micromachined in a variety of sizes and lengths, suitable for implantation in small nerves, which could enhance the choices for selective stimulation, recording and other neural applications. In fact, polyimides became extremely successful as insulating and support materials for various electrode types, including electrodes for central nervous system, as shown in Figure 1.4 E.

As already discussed, one important aspect in the geometry of cuffs is their inner diameter. One other feature of cuffs, very relevant in several neural applications, is the number of transversal or radial contacts, i.e. contacts that are placed around the nerve. Longitudinal currents, i.e. currents that flow along the nerve, are the most effective in stimulation of neurons. Sweeney *et al.* [121] have, however, proven that by using sub-threshold transversal currents (low-amplitude, cross-sectional currents), excitation fields could be *steered*, thus increasing selectivity compared to solely using longitudinal currents. This technique, known as field steering, has proven to be effective in selective and independent activation of the 4 fascicles in large sciatic nerves using 4 transversal or radial contacts [25]. The

commercially available ActiGait® uses a 2.3 mm diameter cuff with 4 transversal contacts applied to common peroneal nerve to control foot dorsiflexion without activation of afferent sensory fibers [122]. Works by Polasek *et al.* [26, 123] on arm's small radial nerves have highlighted that for achieving spatial selectivity in sub-mm or near-mm nerves, multipolar cuff electrodes with a high number of transversal contacts (higher than 10 transversal contacts) are necessary. Neural applications requiring sub-millimeter or near-millimeter multipolar cuff electrodes (n>10) represent a huge challenge in terms of integration, and include research in small animals [124], and the new field of electrical impedance tomography [41].

Literature on cuff electrodes for peripheral nerve stimulation is rich and growing, and the need for higher number and higher density of contacts is fueling new cuff designs and technological solutions. Table 2.2 presents a selection of designs of cuff electrode arrays proposed for various peripheral nerve applications. These works make use of different technological approaches for cuff formation, e.g., split-cylinder by clip-on method, self-locking with ratchet teeth, spiral by pre-stressing, spiral by tempering with metal rod, and manual closure with suturing. In that summary table, relevant geometrical features are also included, like inner diameters, number of contacts (specifically number of transversal contacts, if present) and their geometric surface areas; electrochemical measurements, like impedance magnitudes and charge injection capacity are provided. Details on some of these works are provided below and representative figures are shown in Figure 2.11. In 2011, Korivi and Ajmera [125] have presented a micro-cuff electrode design with a clip-type feature that allows for easy opening of the cuff, its placement on nerve tissue, and subsequent closure – Figure 2.11 B. This consists of two, 25 µm thick stainless steel foil electrodes sandwiched between a thin layer of Silastic silicone elastomer (obtained by spin coating), and a molded liquid silicone, that is poured over the pre-molded foil electrodes. A metal wire is used for giving the stainless steel foils their cylindrical shapes, allowing this approach to manufacture cuffs in the sub-mm region. Silicone molding is used to obtain the pinch-hinge structures, and the cuff opening is defined by manually making a slit or cut on the cured structure. The stainless steel electrodes present a GSA of 0.3-0.4 mm^2, or 3 to 4 × 10^6 μm^2, and an impedance varying between 1.8 and 20 kΩ at 120 Hz. In 2015, Kang *et al.* [126] have introduced a self-closing cuff electrode based on parylene-C for peripheral nerves, whose curliness and closeness is realized by the difference in self-stress of different parylene layers due to the heat treatments – Figure 2.11 D. By taking advantage of pre-stressed parylene-C layers, a spiral cuff electrode with an inner diameter of 3 mm is formed. One advantage of this design is that the self-closed structure has no additional locking structure, thus keeping mechanical complexity of the cuff electrode minimum. Metallization consists of a three layer stack composed by chromium, platinum and electrodeposited iridium oxide film (EIROF), yielding an impedance magnitude at 1 kHz of

2kΩ in electrode contacts with an area of 7850 μm^2. Features of the spiral cuff electrode based on parylene-C, by Kang *et al.*, are summarized in the Table 2.2. In 2018, González-González *et al.* [49] have introduced the use of a shape memory polymer (SMP) to fabrication of multi-electrode softening cuffs (MSC) – Figure 2.11 F. Shape memory polymers (like the thiol-ene/acrylate used in their work) present a lower Young's modulus compared to polyimides (1-50 MPa *vs.* 2.5 GPa). A 300 nm of Au is deposited using electron-beam evaporation and then a layer of SMP is synthesized on top, by mixing stoichiometric quantities of different monomers, and cured with UV light and vacuum. After that a 220 nm thick TiN layer is deposited over the Au by RF sputtering. The TiN and Au interconnects are patterned by standard photolithography and wet etching methods. A second layer of SMP is deposited by spin coating and again photo-polymerized. In some electrode samples TiN is not sputtered, so electrochemical properties of Au and TiN could be compared. Electrode designs have been manufactured to target final diameter between 100 μm and 1 mm. with varying number of contacts. For TiN contacts of GSA between 13500 and 139500 μm^2, impedances are between 1 and 3 kΩ, and CIC is 500 μC/cm^2; Au contacts with GSA of 3300 μm^2 exhibit impedances of 750 kΩ.

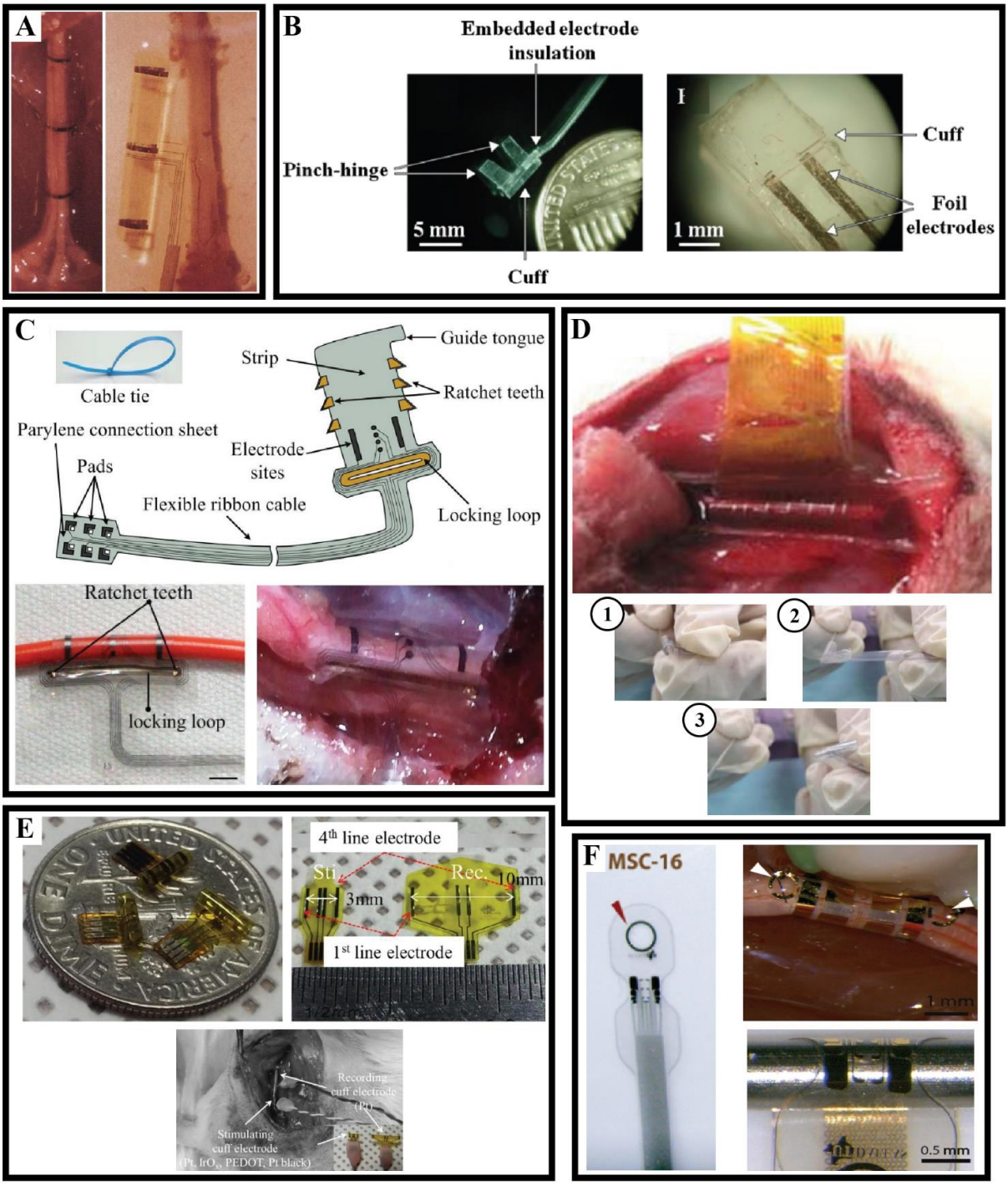

Figure 2.10 Cuff electrode arrays. A) Polyimide-based cuff formed by tempering with metal rod [89]. Left: micrograph of one cuff implanted around the rat sciatic nerve. Right: explanted cuff electrode next to the nerve, showing its cuff shape. Electrode array is composed of 3 ring contacts. B) Microscope images of the clip-on split-cylinder micro-cuff with pinch-hinges [125]. C) Self-locking cuff electrode based on parylene-C, and using a "cable tie" locking mechanism with ratchet teeth (top) [46]. (Bottom left) Cuff wrapped around a hook-up wire with 1.3 mm in diameter. Scale bar = 2 mm. (Bottom right) Cuff snuggly implanted around a rat sciatic nerve. Note the small, 300 µm in diameter contacts in the middle row, and long reference contacts on the sides. D) Self-closing, parylene-C based cuff electrode with 3 mm in diameter and implanted around rat sciatic nerve (Top) [126]. (Bottom) Free stretching of the self-closed parylene-C cuff electrode. 1) start position of free stretching

process, the bonding pads region are fixed between thumb and index fingers; 2) microelectrode sites circle rolling on the quartz tube; and 3) quartz tube slips off the microelectrode sites structure, highlighting the self-closing feature of this electrode. E) Polyimide-based, 1 mm in diameter cuffs formed by tempering with metal rod (top left) [127]. (Top right) Highlight of stimulation and recording configurations of these electrodes. (Bottom) photograph of the rat's surgery after implantation of the stimulating and recording cuff electrodes. The inset shows the photograph of the stimulating/recording cuff electrodes before implantation. F) (Left) Photograph of a multi-electrode softening cuff (MSC) based on thiol-ene/acrylate shape memory polymer (SMP) [49]. The arrow indicates the eyelids included for suture. On the right, MSC with 16 contacts is shown as implanted snugly in a rat sciatic nerve and adapted to a metal rod of 1 mm in diameter.

Table 2.2 Cuff electrode arrays for neural stimulation and recording: State-of-the-art.

Cuff design and forming method	**Inner diameter**	**Number of contacts (transversal), pitch, geometric surface area (GSA)**	**Materials: electrode and insulator**	**Impedance @ 1 kHz**	**Charge injection capacity (CIC) or Q_{inj}**	**Year**
Split-cylinder, clip-on	300 µm	2 contacts 0.3 – 0.4 mm²	Electrode: stainless steel Insulator: silicone elastomer	1.8–20 kΩ (measured at 120 Hz)	-	2011 [125]
Self-locking, ratchet teeth	1.5 – 2 mm adjustable	8 contacts (6 transversal) Ø 300 µm = 70650 µm²	Platinum Parylene-C	8.3 kΩ	-	2014 [46]
Spiral self-closing, pre-stressed	3 mm	20 contacts (4 transversal) 2 mm pitch Ø 100 µm = 7850 µm²	EIROF Parylene-C	2 kΩ	1.91 mC/cm² (200 µs pulsewidth)	2015 [126]
Spiral, tempering with metal rod	1 mm	4 contacts 250 µm × 4 mm = 1 mm²	4 electrode materials: Pt, IrOx, PEDOT, Pt black Insulator: polyimide	Pt 547 Ω IrOx 2635 Ω PEDOT 211 Ω Pt black 191 Ω	Pt 50 µC/cm² IrOx 30 µC/cm² PEDOT 200 µC/cm² Pt black 200 µC/cm² (1 ms pw)	2016 [127]
Manual closure and suture	100 µm – 1 mm	16 contacts (4 transversal) 8 x TiN 13500 – 139500 µm² 8 x Au 3300 µm²	2 electrode materials: Au and TiN Insulator: thiol-ene/acrylate shape memory polymer	TiN 1–3 kΩ Au 750 kΩ	TiN 500 µC/cm² (200 µs pulsewidth)	2018 [49]

3 Electrodes for Neural Stimulation and Recording

Electrical stimulation initiates a functional response by depolarizing the membranes of excitable cells. Depolarization is achieved by the flow of ionic current between two or more electrodes, at least one of which is in close proximity to the target tissue. In most neural applications, electrical stimulation is applied as a series of biphasic current pulses. A typical biphasic pulse waveform with pulse parameters is shown in Figure 3.1. A cathodal current means reduction at the stimulation electrode, with the direction of electron flow being from the electrode to the tissue or electrolyte. Anodal indicates an oxidizing current with electron flow from tissue or electrolyte to the electrode. The charge delivered is the time integral of the current, which is simply $i_c \cdot t_c$, for a cathodal constant-current pulse of magnitude i_c and pulse width t_c. Current pulses are defined in terms of the charge delivered in the leading phase (q), the charge density in the leading phase (CIC or Q_{inj}), the current density (I), the pulse width in each phase, and the pulse frequency.

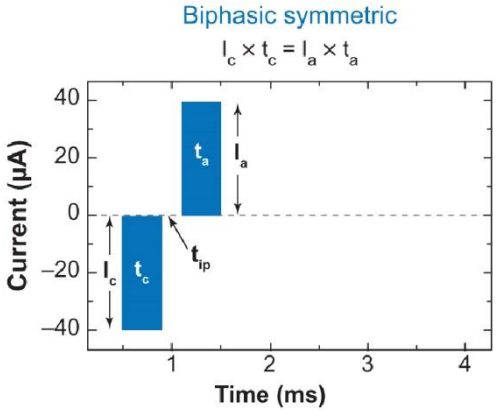

Figure 3.1 Typical charge-balanced, biphasic symmetric current waveform used in neural stimulation and in electrode characterization. The parameters vary widely depending on the application and size of the electrode. Waveform parameters usually falling in the range of I_c (cathodic current), 1 μA – 10 mA; I_a (anodic current), 1 μA – 10 mA; t_c (cathodic half-phase period), 50 μs – 4 ms; t_{ip} (interphase gap), 0 – 1 ms; and t_a (anodic half-phase period), 50 μs – 10 ms [150].

The geometric surface area (GSA) of the electrode is used to define the charge and current densities. The electrochemical surface area (ESA) can vary greatly depending on the methods employed in manufacturing of electrodes and also on the conditions used in its measurements. ESA is the real surface area of an electrode, and factors like surface roughness can make it larger or much larger than GSA.

The activity of neurons or neural populations is recorded as extracellular potentials, or action potentials, when the recorded signal identifies the firing of single neurons or groups of neurons. Recording electrodes are typically characterized by their impedance at 1 kHz, which can be quite variable – as seen in Chapter 2 – depending on electrode material, size, and fabrication technologies. The reason why impedance magnitude at a frequency of 1 kHz is widely accepted as a good proxy of an electrode's ability to record neural activity, is mainly because this is the fundamental frequency of a neuronal action potential, which has a time period of approximately 1 ms. Indeed, it has been shown that large differences in cell reactive responses result in larger impedance values at 1 kHz [151].

3.1 Macro and Microelectrodes

The electrodes, part of neural stimulators present in the Figure 1.2 of Chapter 1, have geometric surface areas of 0.03 mm^2 (30000 μm^2), 0.14 mm^2 (140000 μm^2) and 6 mm^2 (6000000 μm^2), respectively part of the retinal, cochlear and deep brain implants. From the perspective of charge injection reactions at the electrode-tissue interface, the cochlear and deep brain stimulation (DBS) electrodes are typically considered as macroelectrodes (GSA > 100000 μm^2), and the retinal electrodes, with a GSA between 10000 μm^2 and 100000 μm^2, are considered as being in a transition region between micro and macroelectrodes [150]. Macroelectrodes exhibit high-charge/phase thresholds and low-charge density thresholds, whereas microelectrodes (GSA < 10000 μm^2) have the opposite behavior, exhibiting low-charge/phase thresholds and high-charge density thresholds. As discussed in Chapter 2, one important advantage of microelectrodes is their ability to stimulate or record small sub-neural populations from within a nerve trunk (and also from the brain). If a high number of contacts is provided in one electrode array that can result in improved selectivity and spatial resolution, with gains in functional responses. A short summary of macro and microelectrodes and respective charge/phase and charge density thresholds for given applications, are presented in Table 3.1.

3.2 Mechanisms of Charge Injection

Electrodes for neural stimulation and recording are usually composed of several electro-active contacts surrounded by a biocompatible and bio stable insulation material. Contacts in electrodes are metallic (or metallic-like) conductors, and reactions at the electrode-tissue interface are required to mediate the transition from electron flow in the electrode to ion flow in the tissue. Beyond chemical and biological inertness, the metallic structures carrying out the stimulation have to be electrochemically stable over a wide range of electrical loading to deliver the required charge.

Table 3.1 Charge/phase and charge density threshold requirements for neural applications with macro and microelectrodes

Application	Electrode area	Threshold charge/phase (nc/phase)	Threshold charge density (μC/cm²)	Pulse width (μs)	Reference
Cochlear	0.38 mm² 3.8×10^5 μm²	50 – 100	12 – 26	100	[152]
DBS for Parkinson's	6 mm² 6×10^6 μm²	92 – 206	1.5 – 3.4	30	[153]
Bladder sensory reflex	2000 μm²	2 – 5	100 – 250	200	[154]
Cortex for tactile sensation	5000 μm²	7	140	500	[38]

Neural responses (usually in form of an action potential) should be elicited, ideally, without inducing irreversible electrical corrosion reactions in the physical material, and without damaging the tissue. Macroelectrodes, with their modest charge injection densities, do not typically corrode or exhibit degradation, but can lead to tissue damage because of high-charge/phase. For microelectrodes, charge densities are high and electrode degradation as well as tissue damage are encountered [155]. The charge/phase and charge density each contribute to stimulation-induced tissue damage and both must be known to predict whether stimulation might be harmful to tissue [156]. Tissue damage mechanisms are not part of this Thesis, but the works of McCreery, Agnew and Shannon can be used as references [155-158].

Some of most used materials in electrode arrays for delivering electric stimulation to the excitable neural tissue include, but are not limited to:

- noble metals, such as platinum [30, 89], platinum-iridium alloys [22], and gold [159-160]
- stainless steel [161-162]
- other alloys based on iridium (e.g., SIROF) [29]
- other metals: TiN [163-166]

Aforementioned materials inject charge into the biological tissue by two possible mechanisms: capacitive and faradaic. Faradaic reactions involve the transfer of an electron across the electrode-

electrolyte interface and require that some chemical species, on the surface of the electrode or in electrolyte, undergo a change in valence, i.e., are oxidized or reduced. Instead, capacitive charge transfer involves a purely double-layer ion-electron charge separation at the electrode-electrolyte interface, with no transfer of electrons between the electrode and electrolyte (transfer of electrons can occur transiently). Capacitive, non-faradaic reactions include redistribution of charged chemical species in the electrolyte. These two primary mechanisms of charge transfer at the electrode/electrolyte interface are illustrated in Figure 3.2. In Figure 3.2 A, a representation of both faradaic and capacitive charge injection mechanisms highlights the direct transfer of electrons involved in the former.

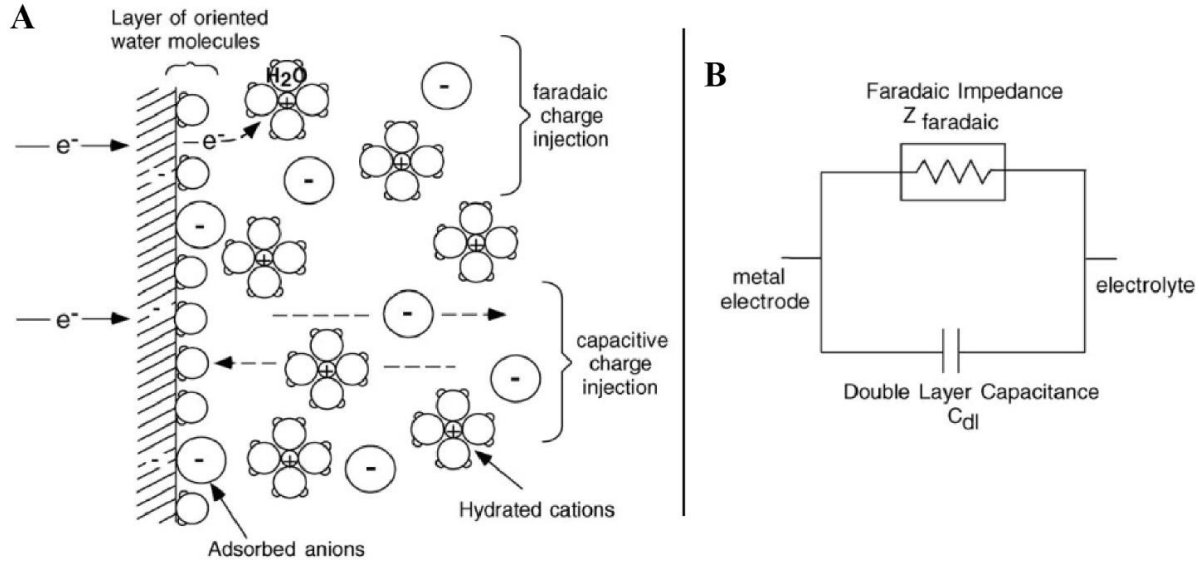

Figure 3.2 The electrode/electrolyte interface, illustrating faradaic charge transfer (left, top) and capacitive redistribution of charge (left, bottom) as the electrode is driven negative (cathodic): A) physical representation; B) two-element electrical circuit model for mechanisms of charge transfer at the interface. The capacitive process involves reversible redistribution of charge. The faradaic process involves transfer of electrons from the metal electrode, reducing hydrated cations in solution (symbolically $O + e^- \rightarrow R$, where the cation O is the oxidized form of the redox couple O/R). An example reaction is the reduction of iridium oxide into iridium (equation 3.5). Faradaic charge injection may or may not be reversible [167].

3.2.1 Capacitive charge injection

If only non-faradaic redistribution of charge occurs, the electrode/electrolyte interface may be modeled as a simple electrical capacitor called the double layer capacitor C_{dl} – Figure 3.2 B. The double layer at the electrode-electrolyte interface comprises an inner layer of absorbed water molecules and specifically absorbed ions, and an outer layer of hydrated ions which form a diffuse layer. The total thickness of the double layer in physiological saline is less than 10 nm. Besides the electrolyte composition, the capacitance of the double layer (C_{dl}) depends on the electrode material and potential,

although the potential dependence is difficult to model theoretically. A simplistic model of the double layer is the parallel plate capacitor:

$$C_{dl} = \frac{\varepsilon_0 \varepsilon_r ESA}{t} \tag{3.1}$$

where ε_0 and ε_r are the permittivity of free space and dielectric constant of the absorbed water layer (inner layer), respectively, ESA is the electrochemical surface area of the electrode, and t the thickness of the inner layer. The weakness of this model is that it predicts capacitance as a constant. As pointed by Bard and Faulkner [168], that does not reflect reality, and variations in capacitance with potential and concentration of ions suggest that either ε_r or t depends on these variables. A more complex, better model of the interface is discussed in the next Section. The dielectric constant of the primary layer of absorbed water at the surface of a metal is 6 – dielectric constant of water at 37 °C is around 74. There is also a significant contribution to the capacitance from the less aligned water molecules in the outer layer, for which the estimated average dielectric constant is about 40. The double layer capacitance is the series sum of these two capacitances. Equation 3.1 predicts that a larger C_{dl} can be obtained by increasing the ESA of an electrode and by increasing the dielectric constant at the interface. Both approaches are effective in increasing the available capacitance of an electrode for charge injection. An interesting example of increasing charge capacity by increasing ESA is that of porous/rough TiN, sometimes called fractal TiN [163].

Several phenomena can be considered to be at the basis of a double layer capacitor. First, when a metal electrode is placed in an electrolyte, charge redistribution occurs as metal ions in the electrolyte combine with the electrode. This involves a transient transfer of electrons between the two phases, resulting in a plane of charge at the surface of the metal electrode, opposed by a plane of opposite charge in the electrolyte. A second explanation for the formation of the double layer is that some chemical species such as halide anions may specifically adsorb to the solid electrode, acting to separate charge. A third explanation is that polar molecules such as water may have a preferential orientation at the interface, and the net orientation of polar molecules separates charge [167]. During electrical stimulation, the net charge varies on the metal electrode, thus a redistribution of charge occurs in the solution. If two metal electrodes are immersed in an electrolytic salt solution, and a voltage source is applied across them that means one electrode is driven to a relatively negative potential and the other to a relatively positive potential. At the negatively-driven electrode, an excess of negative charge will attract positive charge (cations) from solution to it, and repel negative charge (anions). In the interfacial region, there will be net electroneutrality, because the negative charge excess on the electrode surface will equal the positive charge in solution

near the interface. The bulk solution will also have net electroneutrality. At the second electrode, the opposite process occurs, i.e., the repulsion of anions by the negative electrode is countered by attraction of anions at the positive electrode. If the total amount of charge delivered is sufficiently small, only charge redistribution occurs, there is no transfer of electrons across the interface, and the interface is well modeled as a simple capacitor. If the polarity of the applied signal is then reversed, the current direction is reversed, the charge redistribution is reversed, and charge that was injected from the electrode into the electrolyte, and stored by the capacitor, may be recovered. In principle, capacitive charge-injection is more desirable than faradaic charge-injection because no chemical species are created or consumed during a stimulation pulse – if the electrode is cycled within its water window. The capacitive behavior of an electrode can be identified, as opposed to a resistive one, when characterizing it with electrochemical characterization methods, like electrochemical impedance spectroscopy and cyclic voltammetry. That will be subject of analysis in the next Section.

3.2.2 Faradaic charge injection

Charge may be injected from the electrode to the electrolyte by faradaic processes of reduction and oxidation, with electrons being transferred between the two phases. Reduction, which requires the addition of an electron, occurs at the electrode that is driven negative (cathodic phase in Figure 3.1), while oxidation, requiring the removal of an electron, occurs at the electrode that is driven positive (anodic phase in Figure 3.1). Unlike the capacitive mechanism, faradaic charge injection leads to formation of products in the solution that cannot be recovered upon reversing the direction of current if the products diffuse away from the electrode [167]. Figure 3.2 B illustrates a simple electrical circuit model of the electrode/electrolyte interface, consisting of two elements as described by Randles [169]. C_{dl} is the double layer capacitance representing the ability of the electrode to cause charge flow in the electrolyte without electron transfer, whereas $Z_{faradaic}$ is the faradaic impedance representing faradaic processes of reduction and oxidation where electron transfer occurs between the electrode and electrolyte. One may generally think of the capacitance as representing charge storage, and the faradaic impedance as representing charge dissipation.

The following are illustrative examples of faradaic electrode reactions that may occur. Cathodic processes, defined as those where reduction of species in the electrolyte occur as electrons are transferred from the electrode to the electrolyte, include such reaction as [167]:

$$2H_2O + 2e^- \rightarrow H_2 \uparrow + 2OH^- \text{ reduction of water} \quad (3.2)$$

$$PtO + 2H^+ + 2e^- \rightleftarrows Pt + H_2O \text{ oxide formation and reduction} \quad (3.3)$$

$$Pt + H^+ + e^- \rightleftarrows Pt\text{-}H \text{ hydrogen atom plating} \quad (3.4)$$

$$IrO_2 + 4H^+ + 4e^- \rightleftarrows Ir + 2H_2O \text{ oxide formation and reduction} \quad (3.5)$$

Anodic processes, defined as those where oxidation of species in the electrolyte occur as electrons are transferred to the electrode, include:

$$2H_2O \rightarrow O_2 \uparrow + 4H^+ + 4e^- \text{ oxidation of water} \quad (3.6)$$

$$Pt + 4Cl^- \rightarrow [PtCl_4]^{2-} + 2e^- \text{ corrosion of platinum} \quad (3.7)$$

$$2Cl^- \rightarrow Cl_2 \uparrow + 2e^- \text{ gas evolution} \quad (3.8)$$

Reactions 3.2 and 3.6 are, respectively, the irreversible reduction and oxidation of water. In first case, it leads to formation of hydrogen gas and hydroxyl ions, which raises the pH of the solution. Oxidation of water is an irreversibly oxidation reaction, forming oxygen gas and hydrogen ions, and thus lowering the pH. Examples of reversible reactions, where species remain bound or close to the electrode surface, are demonstrated by reactions 3.3, 3.4, and 3.5. These reactions are the reversible formation and subsequent reductions of an oxide layer on platinum (3.3) and iridium (3.5). Reaction 3.4 is reversible adsorption of hydrogen onto a platinum surface, responsible for the sometimes called pseudocapacity of platinum. However, these three reactions are electrochemical, as opposed to electrostatic, as in the case of double layer charge storage, and when the consumption or generation of H^+ and OH^- ions occurs. Reaction 3.7 is the irreversible corrosion of a platinum electrode in a chloride-containing media, such as the saline solutions used for *in vitro* tests or the animal's body. In reaction 3.8, chloride ions in solution are oxidized, forming chlorine gas. Rose & Roblee determined the charge injection limit of 150 $\mu C/cm^2$ for platinum, in order to avoid irreversible reactions, such as the reduction or oxidation of water, i.e., to stay within water window limits [170].

3.3 Electrochemical Characterization Methods – Theory and Reference Works

The common techniques for electrochemical characterization of electrodes for neural stimulation and recording are electrochemical impedance spectroscopy (EIS), cyclic voltammetry (CV), and voltage transient measurements (VTM). This characterization provides information about electrochemical function

of electrodes and ensures that the electrochemical behavior is always within safe limits. The setup for these electrochemical tests is usually a 3-electrode cell with saline solution, a reference electrode of Ag|AgCl, and a platinum counter electrode of large dimensions (at least 100 times larger than the working electrode) and low impedance.

An insight into the basics of these techniques is provided below. This is not intended to be an exhaustive and detailed description of such electrochemical methods, as that is not the goal of this Thesis. Some examples from available literature on electrodes based on platinum and TiN are discussed, as this will provide the necessary support to analyze the experimental data, discussed in Chapter 5.

3.3.1 Electrochemical impedance spectroscopy

Electrochemical impedance spectroscopy (EIS) involves measuring the electrical impedance and phase angle obtained with sinusoidal voltage or current excitation of the electrode. The measurement is made over a broad frequency range, typically <1 Hz to 10^6 Hz, and the magnitude of the excitation is sufficiently small that a linear current-voltage response is obtained at each frequency. For voltage excitation, the root-mean-square magnitude of the excitation source is typically ~10 mV, and generally not more than 50 mV. EIS spectra are a lot valuable in assessing the recording capabilities of electrodes and, typically, the value of impedance magnitude at 1 kHz is usually used as a proxy value. Impedance spectroscopy can be used to investigate both tissue and electrode properties. The resistive contribution of tissue or saline conductivity (depending if measurement is *in vivo* or *in vitro*) to the overall electrode impedance is estimated from the impedance measured at high frequency, where the contribution to the impedance due to charge transfer at the electrode-tissue interface is negligible. High frequency (>10^4) impedance increases with decreasing electrolyte conductivity, whereas at the lower frequencies (<10^3) impedance magnitude is unchanged [150].

When interpreting results from EIS, a Randles-type equivalent circuit, as shown in Figure 3.2 B is often used to model the electrode-electrolyte interface. To that, an electrolyte resistance (R_e) element is connected in series to the interfacial, double layer capacitance (C_{dl}) in parallel to the impedance for faradaic reactions (Z_f). However, a more realistic model has been adopted by Norlin *et al.* [171] and it is shown in Figure 3.3. The faradaic impedance element is assigned to polarization resistance, R_p, and a constant phase element (CPE) is used instead of the pure capacitance (Equation 3.1). The CPE element accounts for the non-ideal capacitive behavior of the electrochemical double layer and its frequency dependency.

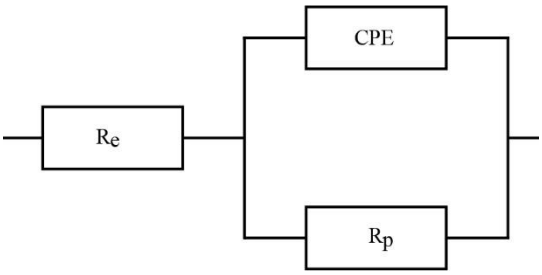

Figure 3.3 Equivalent circuit used in this Thesis to fit EIS experimental data with a model of electrode-electrolyte interface. Adopted from Norlin *et al* [171].

The CPE impedance is represented by:

$$Z_{CPE} = \frac{1}{Q(i\omega)^{\eta}} \tag{3.9}$$

Where i is the imaginary number, ω the angular frequency, Q is a constant, and η is a mathematic expression ($0 \leq \eta \leq 1$). In the case of an ideal capacitor, $\eta = 1$ and Q is the capacitance. Roughness and porosity of electrodes give rise to the non-ideal capacitive behavior (also termed frequency dispersion), and the CPE can be used to describe and model that. Depending on how deep the rough structure extends into the material, it will resemble a porous structure. For porous electrodes, the total impedance will depend on the pore size, depth and pore size distribution.

A brief analysis of the profiles of impedance magnitude and phase relative to TiN films, available in literature, provide good insight about porosity effects, as well as a good basis for later analysis of experimental data. Bode plots of smooth and porous TiN electrodes are shown in Figure 3.4. In both works presented, smooth and porous TiN electrodes exhibit the same high frequency impedance, whereas a marked reduction in low frequency impedance is observed with the porous coating. Near resistive phase angle (approaching 0°) and impedance modulus that is almost entirely solution resistance is observable in the work of Cogan [150] – Figure 3.4 A.

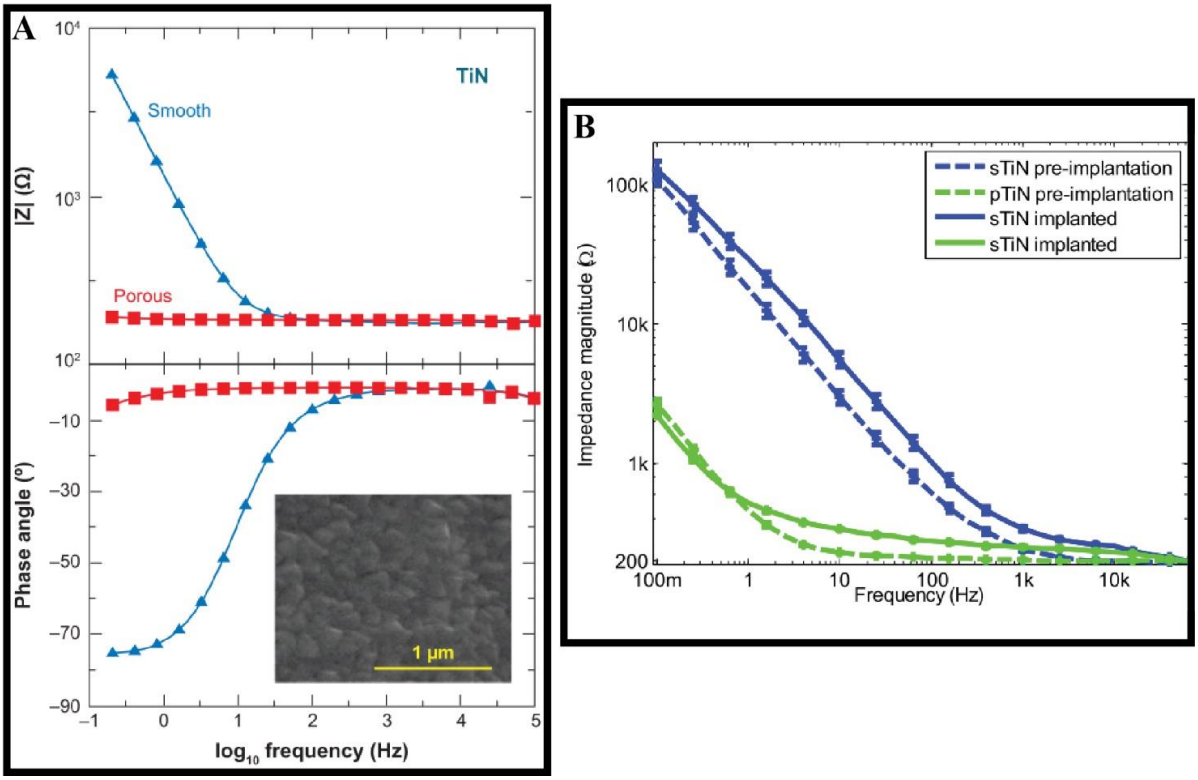

Figure 3.4 Comparison of the impedance of a smooth and porous TiN films demonstrating the difference in impedance magnitude at low frequencies. A) Cogan's work [150] with GSA of 1.4 cm^2, porous coatings remain nearly purely resistive throughout the impedance spectra – also indicated by the phase angle graph approaching 0°). B) Meijs *et al.* [172] work with GSA of 6 mm^2.

3.3.2 Cyclic voltammetry

Cyclic voltammetry (CV) is a three-electrode measurement in which the potential of a test (or working) electrode, with respect to a noncurrent-carrying reference electrode (e.g., Ag|AgCl), is swept cyclically at a constant rate between two potential limits while allowing current to flow between the test electrode and a large, low impedance counter electrode. CV is a useful tool to identify the presence of electrochemical reactions and provides information on the reversibility of the reactions, and on the stability of the electrode. The CV response of a given electrode material can appear very different depending on the sweep rate parameter, and the geometric or electrochemical surface areas, even though the electrochemical reactions remain essentially unchanged. The cathodal charge storage capacity (CSC_c) has become one important electrode parameter to characterize: it is calculated from the time integral of the cathodic current in a slow sweep rate cyclic voltammogram (e.g., 20 or 50 mV/s), over a potential range that is just within the water electrolysis window. For platinum and iridium oxide electrodes, the water window is typically taken as -0.6 V to +0.8 V versus Ag|AgCl, obtained for a very wide range of GSA

between 1000 and 100000 μm^2 [173-175]. For sputtered TiN microelectrodes, water window or safe potential limits were likely found to be within -0.6 V and +0.8 V (GSA = 4000 μm^2) [163].

Figure 3.5 A, also taken from the work of Cogan [150], shows 3 cyclic voltammograms obtained in PBS from identically sized macroelectrodes of platinum (Pt), sputtered iridium oxide film (SIROF), and a smooth sputtered TiN film. The TiN voltammogram has the approximately rectangular shape that is expected for an electrode exhibiting only double layer capacitance (no distinctive peaks from redox reactions). The Pt CV exhibits distinct peaks associated with the oxidation and reduction of a surface oxide (peaks 1 and 2, respectively) and hydrogen-atom plating and stripping (peaks 3 and 4, respectively). Double layer charging also contributes to the capacity of Pt around -0.2 V. The significantly higher charge storage capacity obtained with the SIROF is attributed to its 3D profile (ESA >> GSA). CSC_c of the electrodes are 250 $\mu C/cm^2$, 550 $\mu C/cm^2$, and 2.8 mC/cm^2 for TiN, Pt, and SIROF, respectively. In Figure 3.5 B, it is shown a cyclic voltammogram of a "rough" TiN electrode, taken from the work of Norlin *et al.* [171]. It is important to highlight the capacitive-like behavior at slow sweep rates (50 and 100 mV/s, bottom), similar to that of a "smooth" TiN electrode shown in Figure 3.5 A – the near-rectangular curve shape within the water electrolysis potential range (-0.6 V to + 0.8 V). However, unlike in Figure 3.5 A, small current peaks are visible in the anodic sweep, which could indicate some oxidation process. At high sweep rates (Figure 3.5 B top), the current response of the "rough" TiN electrodes becomes Ohmic-like and independent of sweep rate. The reason for the linear current-potential relationship at high sweep rates is most likely due to the rough surface structure of TiN that resembles a porous electrode. An example of an irreversible reaction occurred in the electrolyte is shown in Figure 3.5 C. When cycled above its water window upper limit (+0.8 V), the platinum electrode gives rise to oxidation of water and oxygen evolution happens – Equation 3.6. This is how to determine the anodic limit of the water window; and a symmetric event happens at the cathodic phase, with water reduction and formation of hydrogen – Equation 3.2. The hydrolysis limits are, therefore, represented in a CV curve as large current peaks (dissolved gas) and indicate the rage for the working polarization voltage.

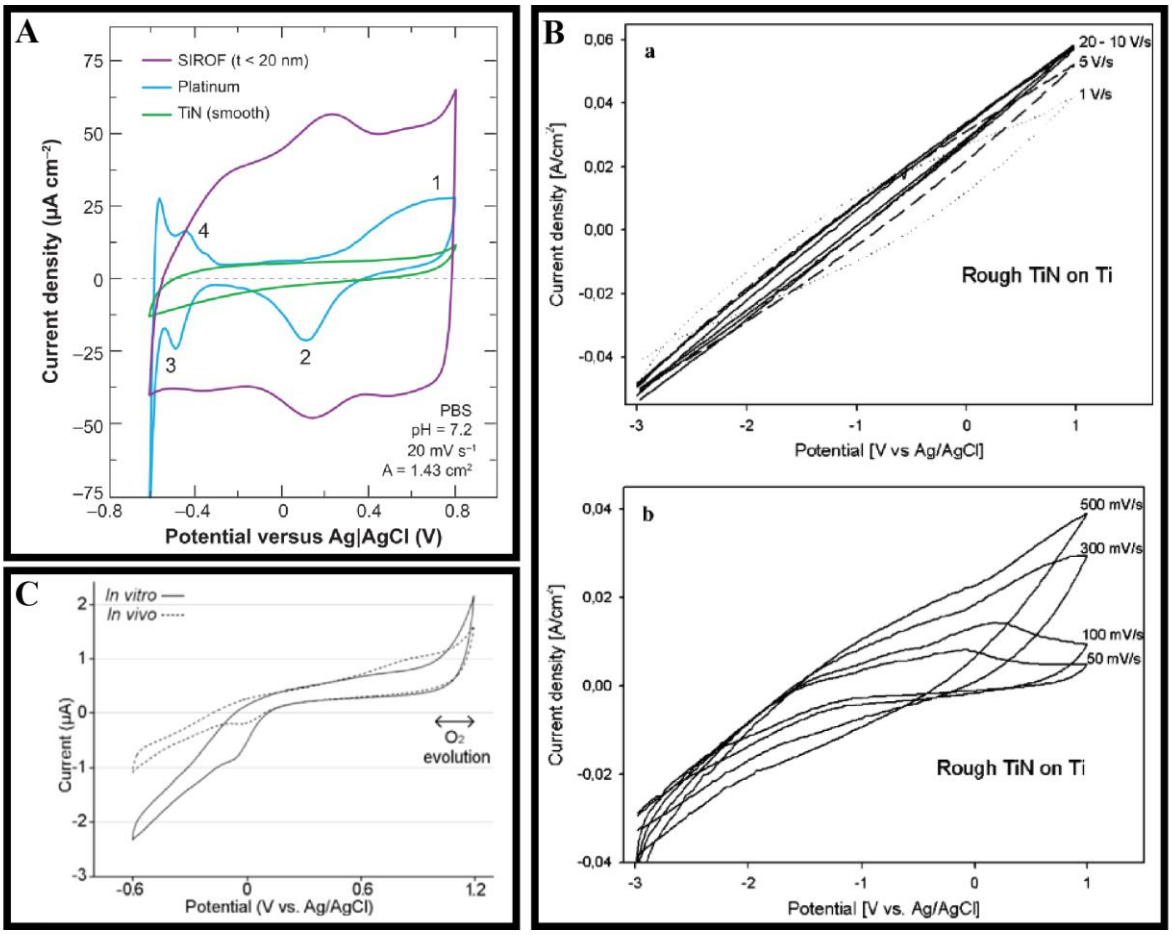

Figure 3.5 Examples of cyclic voltammograms. A) Comparison of cyclic voltammograms of platinum, SIROF, and "smooth" TiN macroelectrodes (GSA = 1.4 cm^2) in PBS at a sweep rate of 20 mV/s. 1, 2 indicate Pt oxidation and reduction; 3, 4 indicate hydrogen-atom plating and stripping on Pt, respectively. The cathodic charge storage capacities (CSC_c) of the films are 250 µC/cm^2, 550 µC/cm^2, and 2.8 mC/cm^2 for TiN, Pt, and SIROF, respectively [150]. B) Cyclic voltammograms of rough TiN at 1, 5, 10, and 20 V/s (top), and 50, 100, 300, and 500 mV/s (bottom) [171]. C) CVs of a Pt macroelectrode performed in PBS and *in vivo* with a sweep rate of 50 mV/s. The sudden increase in current at potentials more positive than 0.9 V indicates oxygen evolution (corresponding to Equation 3.6). No hydrogen evolution is observed in the cathodic phase, as the electrode was cycled at lowest -0.6 V (lower limit of water window) [176].

3.3.3 Voltage transient measurements

A different test is necessary to quantify the charge injection capacity that is accessible for stimulation during electrode use. This will be the sub-portion of the storage capacity which can be achieved when injecting charge with the intended stimulus waveform (e.g., charge-balanced biphasic current pulses). The charge injection capacity (Q_{inj} or CIC) – often referred to in Chapter 2 – is the limit where the charge delivery waveform polarizes the electrode within voltage limits for irreversible reactions (such as hydrolysis). CIC is defined as the charge density that causes the working electrode potential to reach the water window limits. This is a widely accepted method of measuring CIC [163, 173, 177]. The

voltage transients are analyzed to determine the maximum polarization, both the most negative (E_{mc}) and most positive (E_{ma}), across the electrode-electrolyte interface [150]. These potentials extremes are then compared with established, or determined, maximum potentials beyond which it is considered unsafe to polarize the electrode (water hydrolysis). Examples of maximum potential limits were given in previous Section for the Pt, Ir, and TiN films. An example of a voltage transient in response to a biphasic, symmetric current pulse is shown in Figure 3.6. There are several elements that contribute to the voltage transient, and it is not within the scope of this Thesis to analyze them thoroughly. Roughly, for a cathodal current pulse:

$$E_{mc} = E_{ipp} + \Delta E_p = E_{ipp} + (\Delta V - V_a) \tag{3.10}$$

Where the access voltage V_a is taken as the near-instantaneous voltage drop at the onset of either current pulse or immediately after the current pulse is terminated, and E_{ipp} is the potential of the electrode at the onset of the current pulse, or interpulse potential.

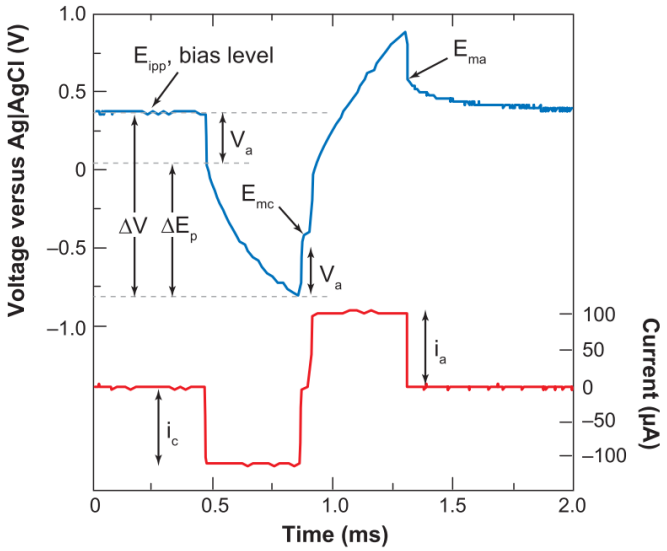

Figure 3.6 A voltage transient of an AIROF microelectrode in response to a biphasic, symmetric ($i_c = i_a$) current pulse.

4 Electrodes Project and Fabrication

As seen in Chapter 2, applications of small cuff electrodes in the sub-millimeter range is still limited by some technological challenges, such as requirements for high density of contacts, and use of materials that are compatible with CMOS processes. A multilayered system, such as the TiN electrodes on polyimide substrates presented in this Thesis, can be influenced by residual stresses. This is particularly important when the multilayered device is intended to be micro-assembled. A brief analysis of the expected strains when curling a polyimide-based microelectrode array (into a cuff) is discussed in Section 4.1. In Sections 4.2 and 4.3 the development of the microfabrication method is presented. In Sections 4.4 and 4.5 a proposal for manual assembly of split-cylinder cuff electrodes is introduced and discussed.

4.1 Stress-Strain Modeling of Polyimide Devices

As mentioned above, the polyimide-based, microelectrode arrays developed as part of this Thesis are multilayered systems. Functionality and reliability of such systems are influenced by residual stresses on the films, after manufacturing. When critical values of stress are exceeded, this may lead to failure of the device. Peeling-off or buckling due to respectively tensile and compressive stresses are typical failure modes. In the case of flexible devices, stresses induced during applied bending can be considerable, especially for small bending or curling diameters. It is therefore obvious that stresses occurring during fabrication and bending of flexible applications must be taken into account in the designing step.

4.1.1 Stoney formula for modeling stress *vs.* curvature

Stoney was the first to formulate an analytical relationship between stress in a thin film and the curvature of a thick and stiff substrate [128]:

$$\sigma_f = Y_s \frac{h_s^2}{6R} \tag{4.1}$$

In the above the subscripts f and s denote the thin film and substrate, respectively, σ_f is the stress in the film, $Y_s = (E/1-\upsilon)$ is the biaxial modulus of the substrate (with E and υ being the Young's modulus and the Poisson's ratio, respectively), h_s is the thickness of the substrate, and R is the radius of curvature of the multilayer system. The Stoney formula has been extensively used in the literature to infer film stress changes from experimental measurement of system curvature changes. Stoney's formula is based on the assumption that the bending stiffness of the film is much smaller than the one of the substrate ($Y_f \cdot h_f \ll Y_s \cdot h_s$), Y_s and h_f are the biaxial modulus and thickness of the thin film, respectively. Flexible

devices are, however, usually very thin and based on polymeric substrates, so that $Y_f \cdot h_f \sim Y_s \cdot h_s$. The main assumption in the Stoney formula is then violated. When the bending stiffness of the thin films cannot be ignored, the film thickness must be included in the analytical solution [129]. Closed-form analytical models are available, in which no assumption is made on the relative thickness of the films and substrate [129-131]. Figure 4.1 shows the differences between the classical model based on the Stoney formula and the exact solution without approximations. Considering a TiN layer on a silicon substrate ($Y_{TiN} / Y_{Si} \sim 1$), both models agree up to a ratio of $h_{TiN} / h_{Si} \sim 0.1$; meaning that for a 500 µm thick silicon substrate (a typical thickness of a silicon wafer), both models agree for a TiN film with a thickness up to 50 µm. However, when this TiN layer is on top of a polyimide substrate ($Y_{TiN} / Y_{PI} \sim 100$), both models agree only up to a ratio of $h_{TiN} / h_{PI} \sim 0.001$. For a polyimide layer thickness of 10 µm, both Stoney model and the model without approximations agree only for a TiN layer with a thickness up to 10 nm. When dealing with very thin or flexible devices, the classical model based on Stoney formula is not accurate enough for relevant film thicknesses, and the model without approximations has to be used.

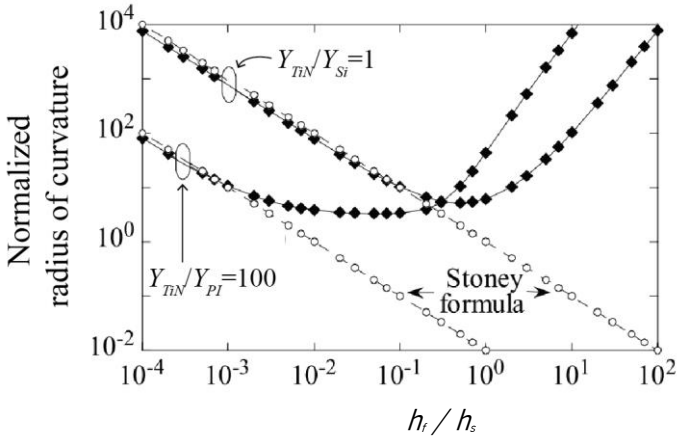

Figure 4.1 Normalized radius of curvature as a function of film/substrate thickness ratio. TiN is illustrated as film layer and two different substrate types are illustrated: silicon and polyimide, respectively ratios of 1 and 100. Full lines represent the exact solution with no approximations, and dashed lines represent the approximation based on the Stoney formula. Graph adapted from [132].

4.1.2 "Flexible" models for modeling stress *vs.* curvature

A Matlab-based program named Flexible StressStrain (FleXss) that has been previously developed and validated [133] [134], was used for modeling the elastic deformation of polyimide-based electrodes due to residual stresses and applied external bending. In general, when using this modeling tool, the user can choose from 5 available models – a model based on the Stoney formula, so-called "classical", plus 4 additional models with fewer assumptions called "flexible" models. As an input to the software, the user must define the material properties of each layer such as the Young's modulus E, the Poisson's ratio

υ, and the coefficient of thermal expansion (CTE) α. Additionally the user can edit the fabrication process of the multilayer electrode by stating the order and thickness of each layer, together with their built-in strains and deposition temperatures. Figure 4.2 shows the FleXss' GUI that is composed of four main panels where the user can create, edit, visualize and delete materials and devices. The panel "Library of MATERIALS" lists the mechanical properties of each layer, the panel "Library of DEVICES" is where the user can create, edit or delete new devices, define their thicknesses, deposition temperature, built-in strain and possible annealing temperature of each layer.

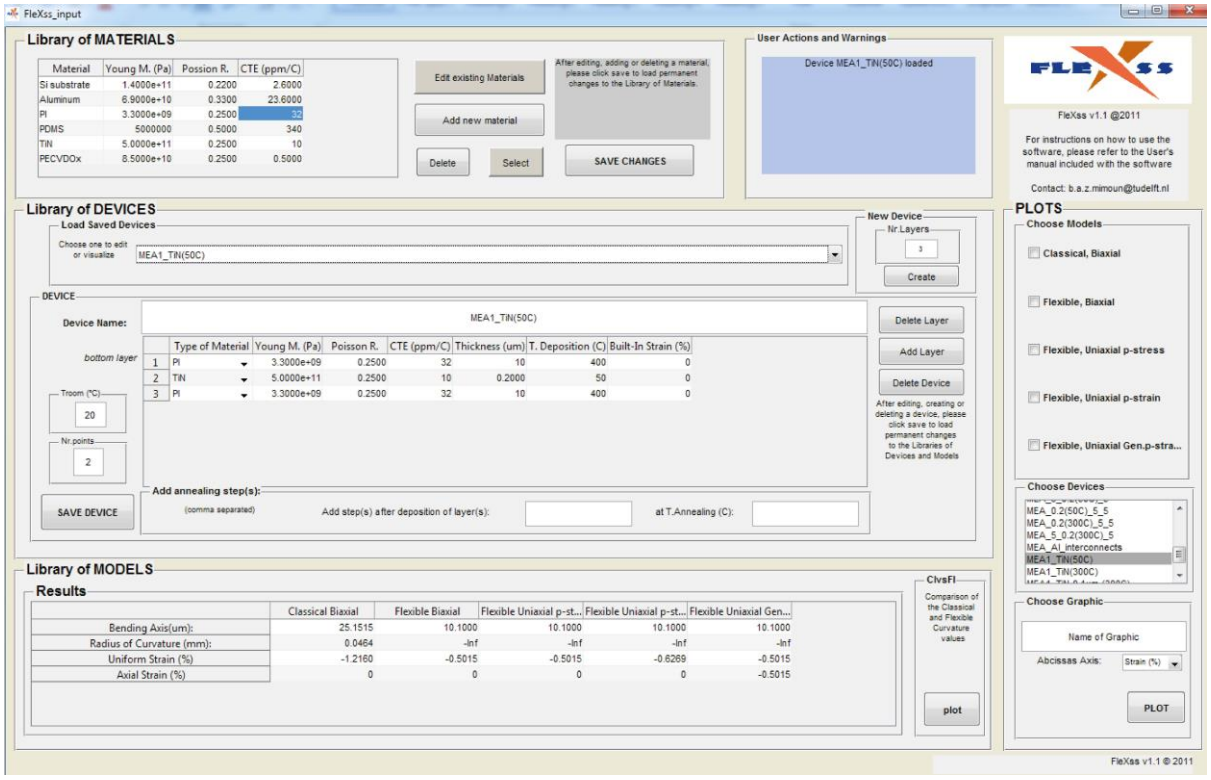

Figure 4.2 Graphical user interface of the FleXss software with a polyimide-based TiN in the "Library of DEVICES". Each polyimide layer is 10 µm thick, and the TiN layer is 200 nm thick.

When a newly created device is saved, its radius of curvature after fabrication, the position of bending axis, and strains are displayed in the "Library of MODELS" panel for each of the five available models. It is possible to determine whether the "classical" Stoney model is accurate enough or if one of the "flexible" models (with fewer approximations) has to be used, by using the *ClvsFl* (classical vs flexible) function, which can be found in the GUI's bottom right (Figure 4.2). The bending stiffnesses of the thin layers are compared with the bending stiffness of the substrate. The difference between the classical and flexible models is then plotted. The critical thickness ratio is defined as the thickness ratio between the layers and the substrate at which the difference between the classical and the flexible models is of 10%. Above this 10% deviation, the classical model is not considered as accurate anymore, and one of the

flexible models has to be used. Figure 4.3 shows a polyimide-TiN-polyimide device and the corresponding *ClvsFl* analysis.

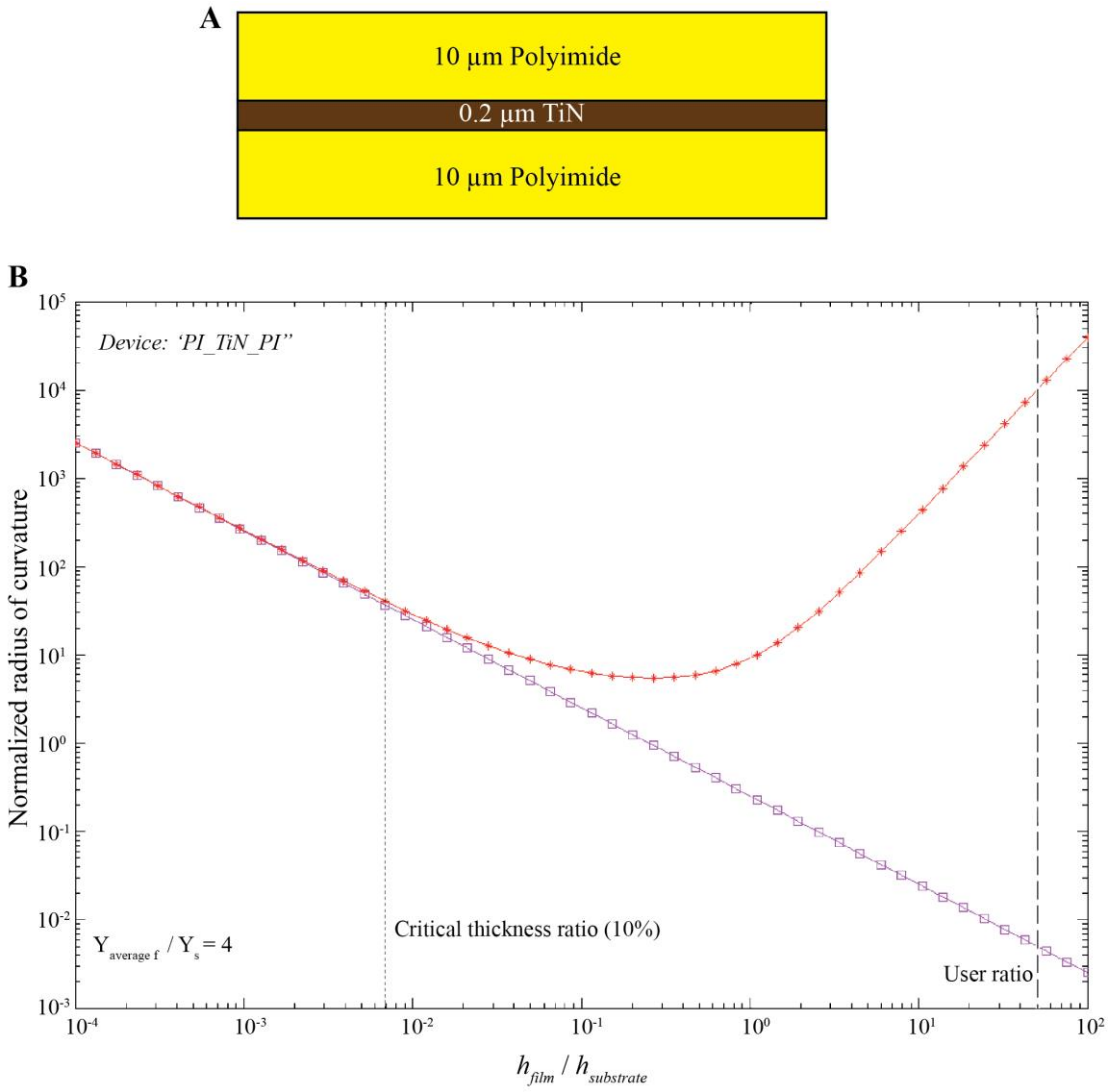

Figure 4.3 A) Schematic cross-section of the "PI_TiN_PI" device in analysis. B) *ClvsFl* analysis for the "PI_TiN_PI" deivce. The user's ratio (10 µm / 0.2 µm = 50) is well above the 10% critical ratio.

It is clear from Figure 4.3 that for the device discussed, both models only agree up to a critical ratio of around 0.007 (7%). That means, for a 10 µm thick polyimide substrate, the classical model is only valid for TiN layers up to 70 nm. As, in the current Thesis, the target thickness for TiN is 200 nm, it turns obvious that one of the "flexible" models has to be used in this case.

4.1.3 Predicting radius of curvature of polyimide-based multilayered devices

Strains in thin films are mainly originated from a built-in component ε_0 and a thermal component ε_{th}. Built-in stress in a film usually results from the growth and/or microstructure of the layer and can be tuned to a certain extent. The thermal stresses arise from the mismatch of coefficient thermal expansion

(CTE) between the films and the substrate. Residual stresses have to be taken into account when designing or studying a mechanically flexible device as they can be the cause of failure of the device. Thin films are reported to be generally more resistant to compressive rather than tensile strains. Approximate critical failure strains of 0.5 % in tension and -2 % in compression have been reported for brittle layers [132]. In the case of metal films, there is a huge spread in the reported failure strains, from less than 1 %, up to more than 50 % in tensile mode [135]. Figure 4.4 shows the strain distribution in two types of devices bent to a diameter of 500 μm. It appears that at 500 μm bending diameter, the strain in the neutral stress plane is -0.5 % and -0.25 %, respectively in the "PI_TiN_PI" and "PI_Ti_TiN_Al_PI" devices. Considering the critical failure strains mentioned above, at 0.5% and higher, these two devices are considered feasible for microfabrication, as well as for bending to sub-millimeter diameters (to a minimum diameter of 500 μm).

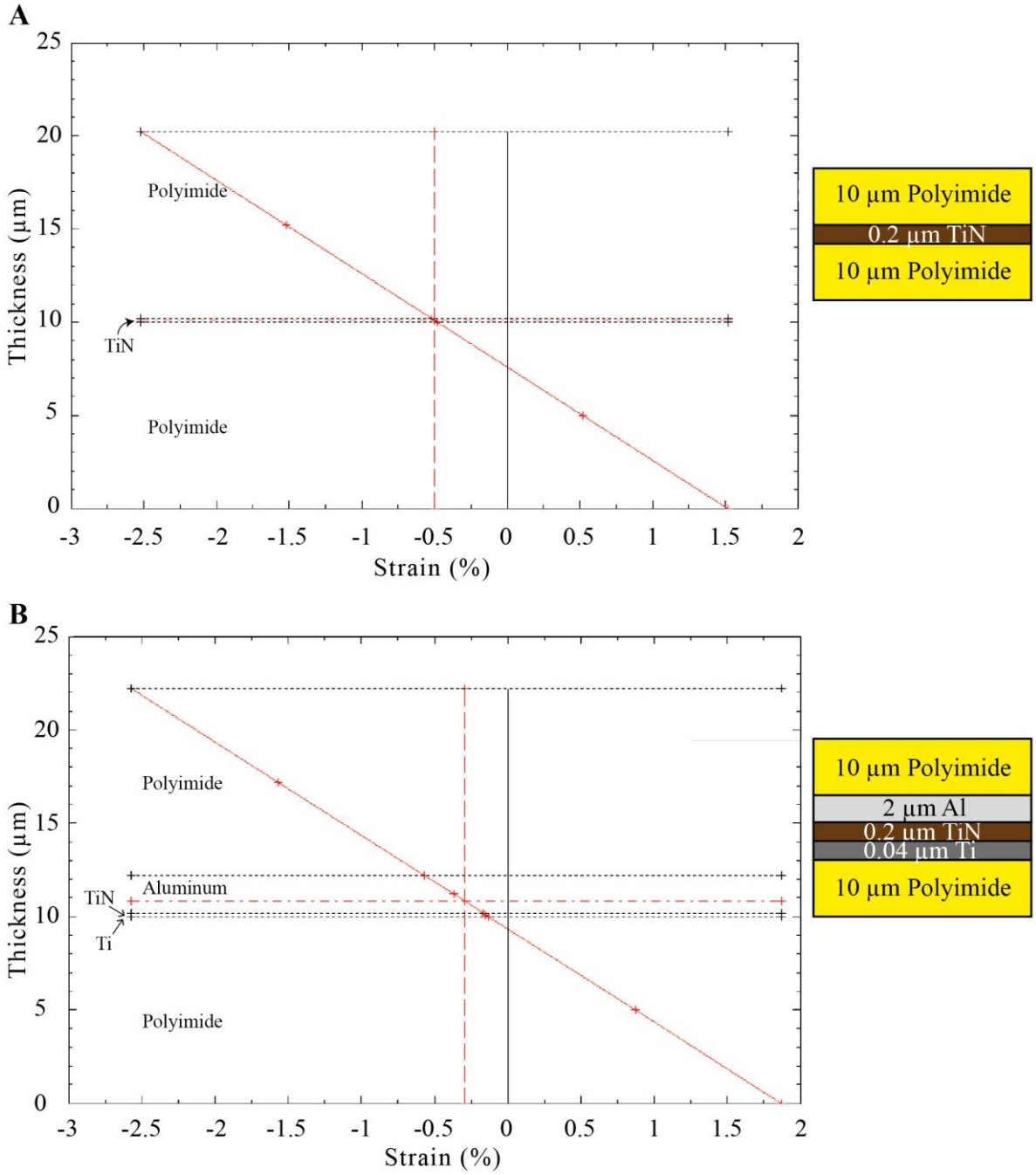

Figure 4.4 Strain distribution upon bending to 500 µm diameter of polyimide-based structures with infinite metal layers. Two devices were modeled: A) "PI_TiN_PI", B) "PI_Ti_TiN_Al_PI". Thicknesses of each layer are indicated on the schematic cross-sections on the right side. Horizontal red, dashed line indicates the neutral stress plane. Vertical red, dashed line indicates the corresponding strain value at the neutral stress plane.

4.2 On-wafer Microfabrication Process

A microfabrication process was developed and conducted in a class 100 cleanroom, at the Else Kooi Laboratory in Delft, the Netherlands. 100 mm diameter, 525 μm thick, single sided polished silicon wafers were used as substrate. Figure 4.5 shows a schematic of the microfabrication steps. A 6 μm thick silicon dioxide (SiO_2) layer was deposited on the back side of the silicon wafer using plasma-enhanced chemical vapor deposition (PECVD). Then, a 1 μm SiO_2 layer was deposited, also by PECVD, on the front side – Figure 4.5 A. The 6 μm SiO_2 backside layer was patterned using 3 μm thick photoresist as masking layer for plasma etching. Etching of SiO_2 was done with a plasma containing CF4 (50 sccm), CHF3 (25 sccm) and He (40 sccm). Backside SiO_2 will be used as a hard-etch mask during a deep reactive ion etching (DRIE) step at a later stage of the process – Figure 4.5 B. A base layer of polyimide (PI2611, HD MicroSystems) was spin coated on the front side of the wafer to yield a thickness of approximately 16 μm. Soft bake of polyimide was done for 7 minutes on a hot plate at 140 °C, followed by a 2 hours curing at 400 °C in a low pressure nitrogen environment. After soft baking and curing of this polyimide layer, its thickness ranges between 9 and 10 μm. Subsequently, a 200 nm thick TEOS (tetraethylorthosilicate oxide) layer was deposited by PECVD at 300 °C. Then, this layer was patterned using 2 μm thick photoresist as masking, combined with plasma etching. The PECVD TEOS will later be used as a hard mask during polyimide dry etching. A two-step approach was followed for dry etching of polyimide. First, a pure oxygen plasma was used to etch an initial thickness of approximately 6 μm, due to its fast etch rate: 2-5 μm min^{-1}. Etch rate of polyimide in such barrel etcher was found to be highly dependent on temperature (the longer it stays, the faster the etch rate). Polyimide etching was concluded using a plasma with 80% of O_2, 13% of N_2 and 7% of CF_4 in order to minimize silicon residues [136]. Then, the TEOS mask layer was removed by wet etching using buffered hydrofluoric acid (BHF) 7:1 – Figure 4.5 C. After patterning and etching of polyimide, a stack of three metals was sputtered at 300 °C without breaking vacuum: 40 nm titanium layer as an adhesion layer on polyimide, 200 nm of TiN as electrode material, and 2.5 μm of aluminum, used to form bond pads on silicon chip and to promote good interconnects. Patterning of the 2.5 μm thick aluminum was done by thinning it down to 250-300 nm using a chlorine-based plasma. After that, wet etching with a PES-type etchant is done for etching of the remaining aluminum. This approach guarantees that the TiN layer is not etched by the chlorine-based plasma. After etching of the 2.5 μm thick aluminum and patterning of bond pads, another aluminum layer (100 nm thick) is deposited at room temperature. This layer is used for protection of TiN surface in subsequent steps like dry etching of the second polyimide layer. TiN and the 100 nm thick aluminum are then patterned using again a chlorine-based plasma – Figure 4.5 D. A second polyimide layer is then spin

coated, soft baked and cured following the same process parameters described for the first layer. After curing of the second polyimide layer, a 200 nm thick TEOS layer was deposited by PECVD, and used as a hard mask layer for the polyimide dry etching step – Figure 4.5 E, F.

The back side process consists of an anisotropic silicon deep reactive ion etching (DRIE) using the Bosch process shown in Figure 4.5 G, plus a dry etching of the 1 μm thick SiO_2 deposited on front side and used as an etch-stop layer in the DRIE. After the two-step backside process, silicon islands with bond pads are fully defined and attached to the free-standing 20 μm thick polyimide foils with contact openings and interconnects. Finally, etching of the protective, 100 nm thick aluminum layer on top of TiN contacts can be done using a timed wet etching step in a PES-type etchant (selective to TiN). The entire microelectrode on a flexible foil remains attached to the wafer by polyimide tabs that can be easily cut to mechanically remove the device – Figure 4.5 H. Additional to silicon dies with bond pads, bare silicon dies were patterned on opposite extremity of the device. These prevents polyimide foils from curling, and facilitates assembling onto the cuff.

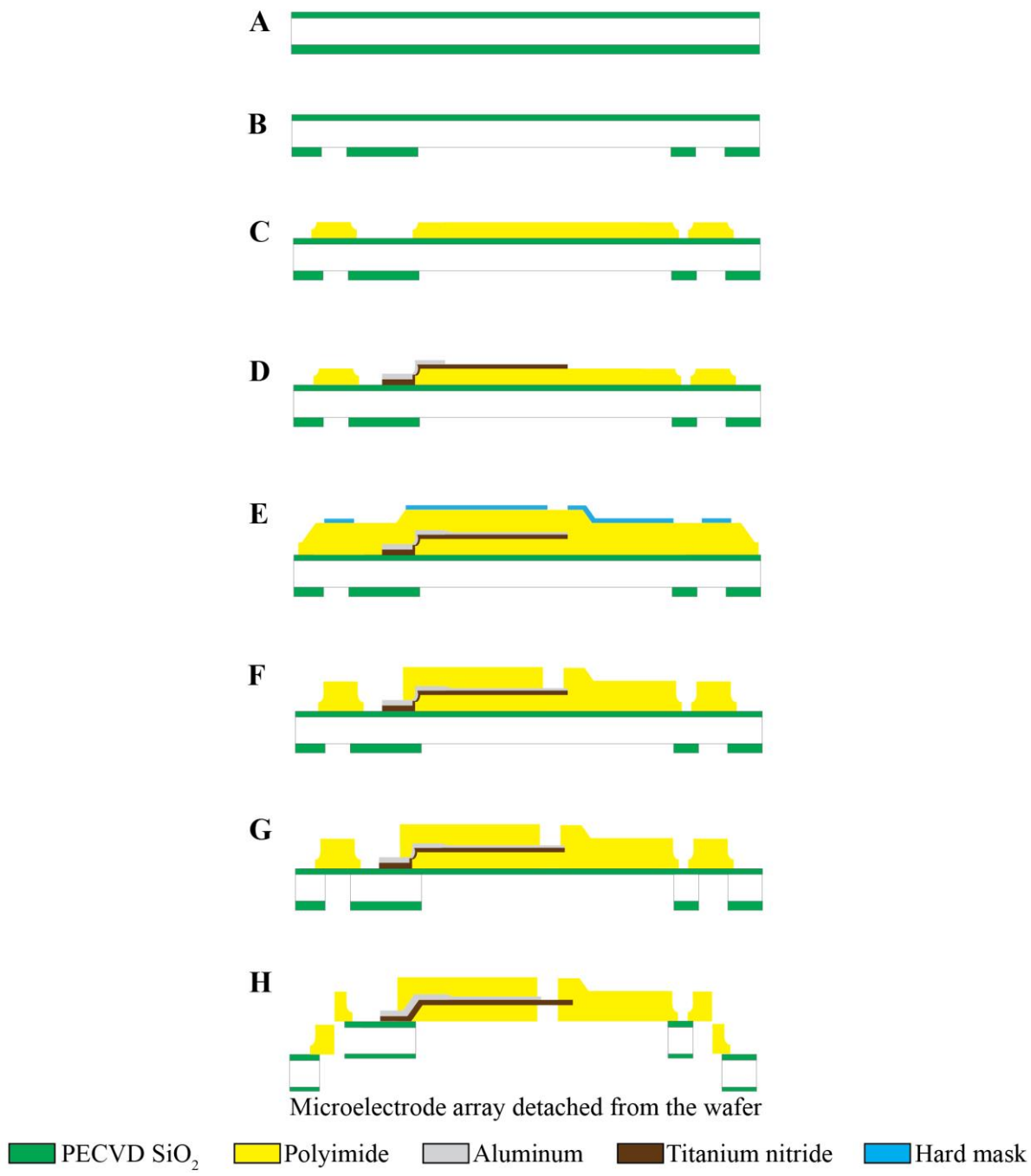

Figure 4.5 Schematic representation of the microfabrication process. The silicon wafer is represented in white color. A) Deposition of back/frontside PECVD oxide layers. B) Patterning of backside oxide layer. C) First polyimide layer coating, curing and patterning (using a TEOS hard etch mask). D) Sputtering and patterning of metals – TiN is exposed after patterning of Al in bondpads. Sputtering and patterning of a thin protective layer of aluminum on top of TiN layer. E) Second polyimide layer coating and curing. Sputtering and opening of frontside hard mask. F) Second polyimide layer etching and front hard mask removal. G) DRIE step landing on PECVD oxide layer. H) Dry etching of oxide layers. Etching of protective aluminum layer using a PES-type etchant – expose TiN contacts. Release of device by cuting the polyimide tabs.

4.2.1 Designing photolithography masks

In order for the microfabrication process to be carried out five photomasks were necessary. Four masks are applied on the front side of the wafer and one is applied on the back side. The five masks are shown in Figure 4.6 A-E. The first photomask is used to pattern the back side SiO_2 that is, in turn, used as a hard mask for etching of bulk silicon, thus defining free-standing polyimide regions; second photomask is used to pattern the first polyimide layer; third photomask is used to pattern the 2.5 µm thick aluminum layer that defines the bond pads on silicon dies and guarantees a good step coverage of metal between silicon dies and polyimide regions – this will be covered in more detail in Subsection 4.2.4; fourth photomask defines the outer edges of TiN contacts and interconnects to close to polyimide's edge on silicon die; fifth photomask defines the second polyimide layer and the actual size of electrode contact openings. The successful fabrication of the microelectrode arrays starts with careful application of mask design rules such as alignment between masks, e.g., openings in polyimide layer that should be accurately centered on top of the underlying TiN layer. L-Edit tool was used to design the masks, as different layers can be represented by different colors and patterns – Figure 4.6 F.

One important aspect considered during the design phase of lithography masks was the size of electrode contact openings, of particular relevance to the fourth and fifth masks. Aiming at characterizing electrode contacts both within the micro and macroelectrode range, two distinct areas have been chosen for electrode contacts: 6400 μm^2 (microelectrode) and 1000000 μm^2 (1 mm^2, macroelectrode). One additional contact area has been chosen in between: 160000 μm^2.

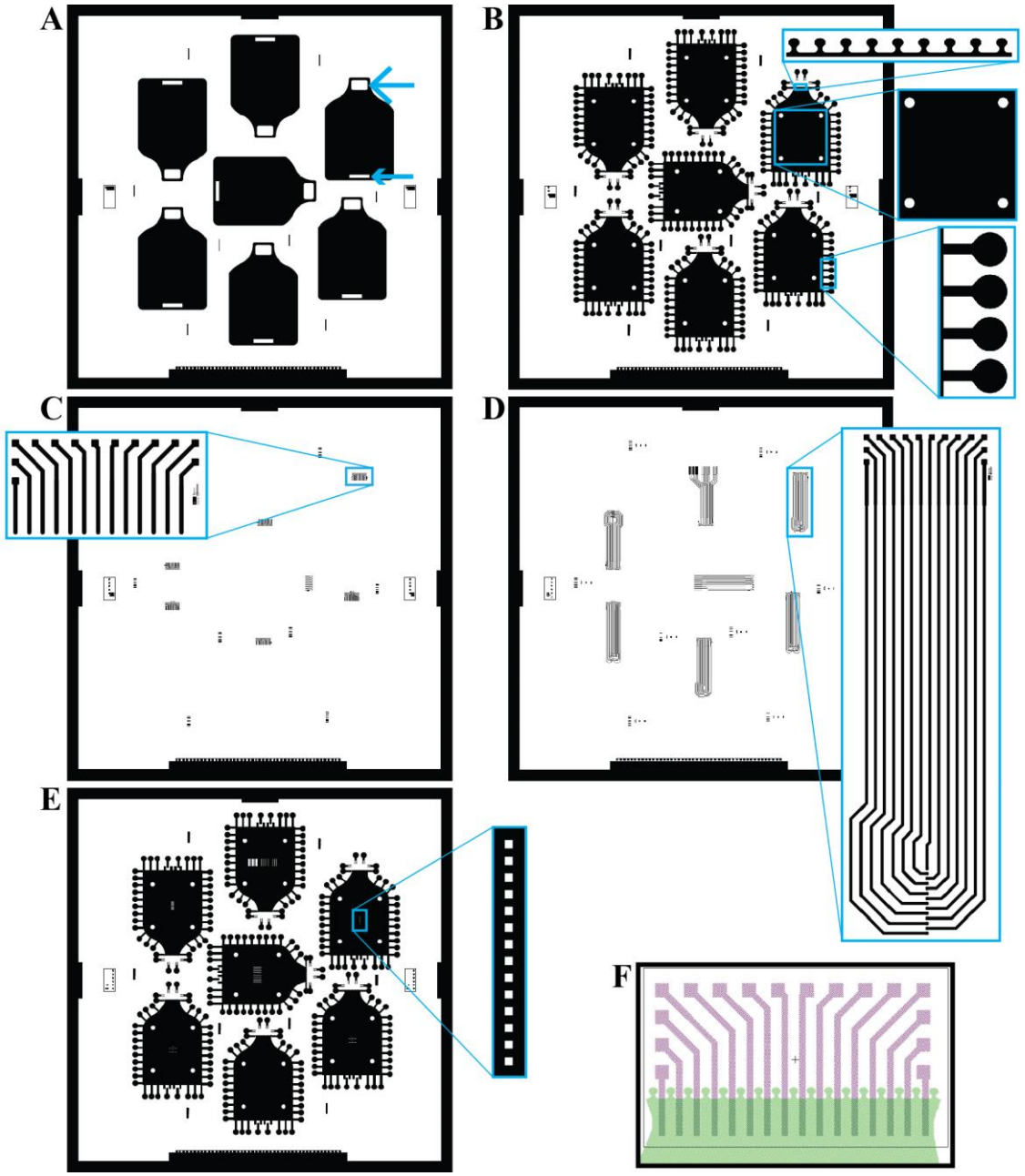

Figure 4.6 Photomasks used in the microfabrication process. Seven devices can be processed in one wafer with 100 mm in diameter. A) First photomask used to pattern the backside SiO_2. Black areas correspond to areas where silicon will be etched. White area indicated by the large arrow corresponds to a silicon die with bond pads, and the small arrow indicates a silicon piece with mechanical function only, thus no electrical function. B) Second photomask used to pattern the first polyimide layer. Black areas are polyimide areas, white areas are etched. Three design features are highlighted: top) pin-like structures on top are used in transition region between silicon dies and polyimide; center) 4 holes in polyimide foils are used for assembly and alignment of microelectrode arrays; bottom) pin-like structures are also used all around the polyimide foils to guarantee good mechanical stability after etching of bulk silicon. C) Third photomask used to pattern aluminum layer forming bond pads and initial portion of interconnects. D) Fourth photomask used to pattern interconnects and TiN contacts. E) Fifth photomask is used to pattern the second polyimide layer, thus defining contact openings. F) A screenshot from L-Edit highlights bond pads and interconnects in purple and polyimide in green.

4.2.2 Spin-coating and curing of polyimide

After etching of back side silicon dioxide, photoresist was removed from the wafers by using a pure oxygen plasma, rinsing in nitric acid (HNO_3), rinsing in deionized (DI) water and dried. Before applying polyimide, silicon wafers were coated with the aminosilane based adhesion promoter VM-652 from HD Microsystems, which proved to significantly improve adhesion and prevent undesired delamination throughout the process. After application of the primer, polyimide was spin-coated using a program in 3 steps: 15 sec at 350 rpm, 45 sec at 1000 rpm, and 2 sec at 4000 rpm (to level edge bead thickness). Polyimide was applied onto the center of the wafer by manually pouring it from a glass beaker containing a volume of 4 mL. The program of the manual spin coater was initiated right after. Soft baking of polyimide was done for 7 minutes at 140 °C, in an in-line hot plate on the coater track. Timing of soft bake was prolonged as compared to recommended by the manufacturer (90-180 sec), since a carrier wafer was used to prevent back side contamination and sticking. As mentioned earlier in Section 4.2, thickness of soft baked polyimide layer was of about 16 µm, measured by profilometer. The polyimide was then cured in a Heraeus vacuum oven, at 400 °C for 2 hours in a 200 mbar nitrogen environment. Cooling down was allowed over-night at room temperature. Cleaning of polyimide layers after curing was done in acetone, isopropanol, and rinsing with deionized water. The curing step produced fully imidized 9-10 µm thick polyimide layers. Next, the masking layer was deposited.

4.2.3 Etching of polyimide

Silicon oxides and metals can be used as masking layers for dry etching of polyimide. In the present work, 200 nm thick PECVD TEOS (tetraethyl orthosilicate, $Si(OH)_4$) layers, deposited at 300 °C, were used. The hard mask was subsequently covered with resist and patterned using lithography and dry etching. After opening of the $Si(OH)_4$ layer, the polyimide coatings were ready to be etched using different recipes. The photoresist covering the hard masks was removed during polyimide etching, since resists and polyimides were etched by that same plasma chemistries.

Etching profile of polyimide layers is one critical processing step in the fabrication of flexible microelectrode arrays. Polyimides can be etched isotropically or anisotropically. A schematic representation of the polyimide etching profiles, used in the current work, is shown in Figure 4.7. Depending on which polyimide layer is being etched – first or second – distinct etching profiles may be chosen. In the first polyimide layer (Figure 4.7 A), semi-slopped profiles are preferred in order to facilitate a good step coverage with sputtered metals and photoresist for patterning of interconnects. In the second polyimide layer (Figure 4.7 B), vertical walls are preferred in order to expose the contact openings. Semi-

slopped profiles were achieved with a combination of isotropic and anisotropic etching chemistries, whereas vertical profiles were achieved by using anisotropic etching only.

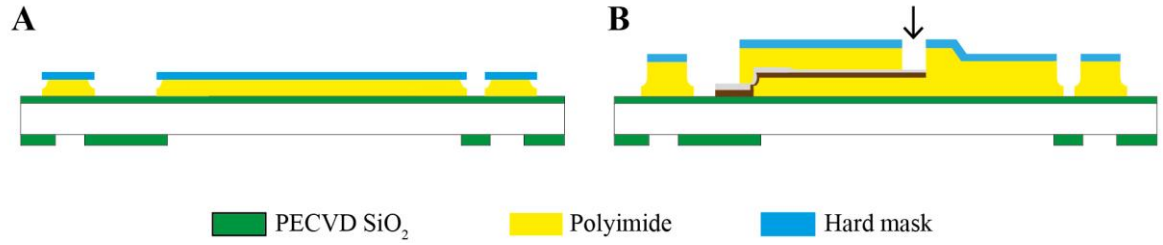

Figure 4.7 Schematic representation of polyimide etching profiles, after spin coating and curing of corresponding polyimide layers. Hard mask layers have also been deposited and patterned. A) Semi-slopped profile of polyimide wall comprising a combination of isotropic and anisotropic etching. B) Vertical polyimide wall achieved with anisotropic-only etching. Downward, vertical arrow indicates contact openings.

Several studies have been published on characterization of polyimide dry etching using different plasma chemistries, etching methods and parameters [137-140]. In this work, two types of plasma etchers were used, a barrel-type etching tool (TEPLA IPC 9200) and an inductively coupled plasma-reactive etching (ICP-RIE) tool (Trikon Omega 201).

In a barrel-type etching tool, the plasma etching is done by ionizing a gas mixture inside a chamber to obtain ions that will react with the material to be etched. The ionization of the gases is done by RF excitation with an electrode at the top of the chamber. The wafer to be etched is placed on an electrode connected to ground. Through random motion, the ions inside the chamber reach the target resulting in a purely chemical etching process.

In an ICP-RIE etcher, the etching principle is similar to that of a barrel etcher, but in this case the chamber's top electrode is connected to ground, and the wafer is placed on the excitation electrode. Since the wafer is now connected to the RF signal instead of ground, electrons are statistically more often in contact with the target than the positive ions (which are heavier). Electrons are highly reactive species and are easily adsorbed by the target material, polarizing it negatively. Simultaneously, the loss of electrons in the plasma results in a globally positively charged ion "cloud", thereby producing an acceleration of the ions towards the wafer. The velocity of the ions results in an etching mechanism called physical etching. The molecules of the layer to be etched are sputtered-off as a result of the impact of the ions on the wafer. The objective is to achieve a high ionization rate in the plasma in order to enhance the RIE effect. As a result, the chemical etching process occurs in combination with the physical process.

Atomic oxygen is the main etchant of polyimide by abstraction and/or addition of oxygen atoms to unsaturated groups. Addition of atomic fluorine in the plasma chemistry has been proven to enhance the

production of atomic oxygen [137], thus increasing the etching efficiency. Also nitrogen (N_2) has also been reported to increase the production of atomic oxygen when added to the plasma chemistry.

In the barrel-type etcher, TEPLA IPC 9200, isotropic etching of polyimide was achieved with a gas composition of 95% O_2 and 5% CF_4 and a power of 1000 W. The etch rate of the polyimide in the barrel etcher was highly variable, starting out at 2 μm/min in initial 60-90 sec, and then increasing up to a maximum of 5 μm/min. The etching time in the TEPLA barrel etcher was set to 3 minutes, which corresponded to total etching between 6-7 μm. The etch rate of the hard mask, $Si(OH)_4$, was found to be ca. 50 nm/min. Indeed, it is known that O_2/CF_4 plasmas etch silicon oxides [141]. In Figure 4.8 A, B show two examples of isotropic etching used in semi-slopped profiles.

The remaining 3-4 μm in first polyimide layer, as well as the second polyimide layer, were etched, anisotropically, using the ICP-RIE etcher, Trikon Omega. Chamber pressure was set to 20 mTorr and the plasma power was set to 500 W. Again, a small amount of CF_4 was added to the O_2 gas mixture in order to increase etch rate, and also N_2 was added to increase production of atomic oxygen. The exact gas composition used for the anisotropic recipe was 80% O_2, 13% N_2 and 7% CF_4. The etch rate of polyimide in the ICP-RIE tool was approximately 1 μm/min, while the etch rate of PECVD $Si(OH)_4$ was about 50 nm/min. Figure 4.8 C, D show examples of anisotropic etching of polyimide layers.

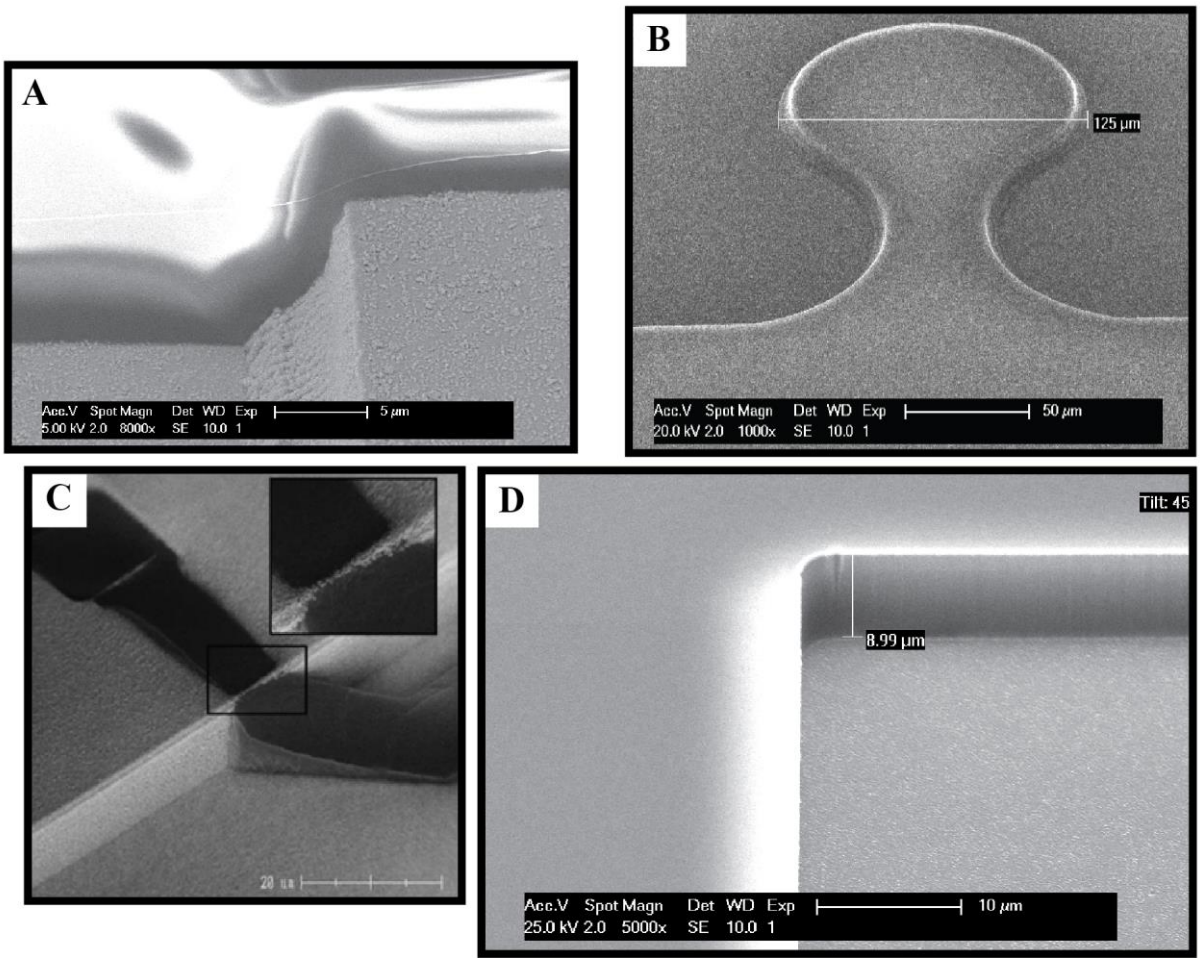

Figure 4.8 Scanning electron microscopy of semi-slopped and vertical polyimide profiles. A) Good resist step coverage on a semi-slopped polyimide profile obtained with isotropic and anisotropic etching. Picture obtained after etching of aluminum interconnects. B) Isotropic etching highlighted in pin-like structures. C) Poor resist step coverage on top of a 10 µm polyimide layer anisotropically etched with a 1.5 µm Al layer sputtered on top for interconnect patterning. D) Anisotropic etching in contact opening.

4.2.4 Sputtering of metal stack

A metal stack comprised of 40 nm of titanium, 200 nm of TiN, and 2.5 µm aluminum was sputter deposited at 300 °C and without breaking vacuum. Titanium and TiN were deposited by DC magnetron sputtering, using a titanium target of 332 mm diameter with 99.999% purity, and using a Sigma 204 SPTS deposition system. The distance between target and silicon wafer was 27.5 mm, at a base pressure of 1.33 x 10^{-7} mbar. At this pressure the chamber was purged with pure argon (20 sccm) and nitrogen (70 sccm). The working pressure during deposition of titanium and TiN ranged between 0.007 and 0.013 mbar. Sputtering of 40 nm thick titanium was done in 30 seconds, and sputtering of 200 nm thick TiN was done in 10 minutes, both at a target power of 6 kW.

The 2.5 μm aluminum layer was patterned using the third photomask, and so it is used for forming bond pads and for achieving a good electrical connection in the transition region between silicon dies and polyimide foils. Figure 4.9 shows a detail of the transition between regions without polyimide to regions with polyimide, on a silicon die. The concept behind the pin-like polyimide structures is to maximize overlapping area of the polymer on silicone, thus increasing mechanical resistance against delamination.

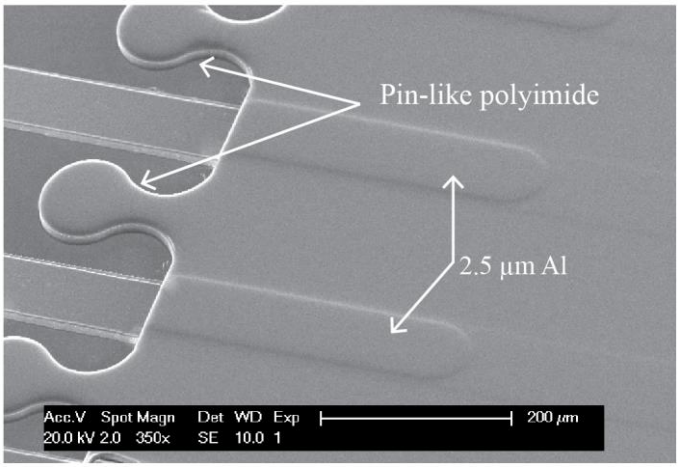

Figure 4.9 Silicon-to-polyimide transition region. Polyimide-free silicon die on the left. Pin-like polyimide structures and the 2.5 μm thick aluminum are visible. Less visible the continuation of Ti and TiN interconnects can be seen on the right side. This SEM picture was taken after spin coating, patterning and curing of the second polyimide layer.

Titanium and TiN were patterned using the fourth photomask, thus producing the interconnects and the electrode contacts. Titanium is known to be a good adhesion layer to polyimide [142], so it was decided to include it in the process. Sheet resistance of the Ti/TiN (40 nm/200 nm) film was of 73.5 Ω/sq. Morphology of the sputtered TiN films was characterized by atomic force microscopy (NTEGRA Aura AFM) – Figure 4.10. The AFM scan was carried with semi-contact mode on sputtered TiN for a scan area of 5 μm × 5 μm on the surface. The TiN surface is comprised of densely packed nodules and tapered crystallites that are approximately circular with a diameter of <100 nm. No hillocks and pyramidal-shaped structures have been identified.

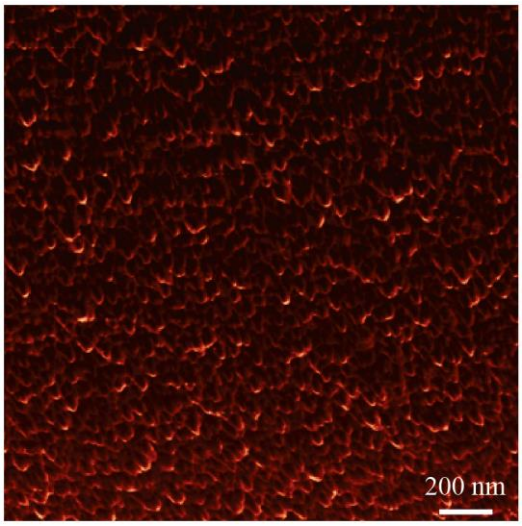

Figure 4.10 Atomic force microscopy (AFM) phase image of a 200 nm thick titanium nitride coating, obtained by magnetron sputtering at 300 °C. Tapered crystallites of up to 100 nm in diameter, separated by voids.

4.2.5 Protecting the titanium nitride surface

As mentioned in the description of the microfabrication process, earlier in Section 4.2, and also shown in Figure 4.5 D, TiN surface in electrode contacts was protected with a 100 nm thick aluminum layer. In particular, two process steps are of criticality: anisotropic etching of second polyimide layer and the deep reactive ion etching (Bosch process) of bulk silicon wafer. It is know that TiN can be dry etched in fluorine containing plasmas, with its surface being changed into a fluorinated titanium compounds (mainly TiF_3, titanium (III) fluoride) [143].

As mentioned in Section 4.2.3, anisotropic etching of second polyimide layer was achieved with a plasma containing O_2 (80%), N_2 (13%), and CF_4 (7%). The Bosch process, used for DRIE of the bulk silicon, is a high-aspect ratio plasma etching process, consisting of the cyclic isotropic etching and fluorocarbon-based protection film deposition by quick gas switching. The SF_6 plasma cycle etches silicon, and the C_4F_8 plasma cycle creates a protection or passivation layer.

In wafers processed without a protective aluminum layer, little impact on surface modification of the TiN layer has been found when performing anisotropic etching of the second polyimide layer. Perhaps, the small modifications in TiN surface during polyimide etching are linked to the relatively low ratio of fluorine in the plasma. However, when processing those wafers without the protective aluminum with the Bosch process, the TiN surface seems to undergo substantial transformation. In Figure 4.11 A, it is shown the TiN surface of a wafer processed with protective aluminum, whereas B depicts that surface without any protective layer after DRIE. It is important to note that apart from modifications in surface roughness

(from crystallites to a uniform layer) and color (darkening), also electrical measurements were substantially affected, with a substantial increase in line resistance, between contact and bond pad.

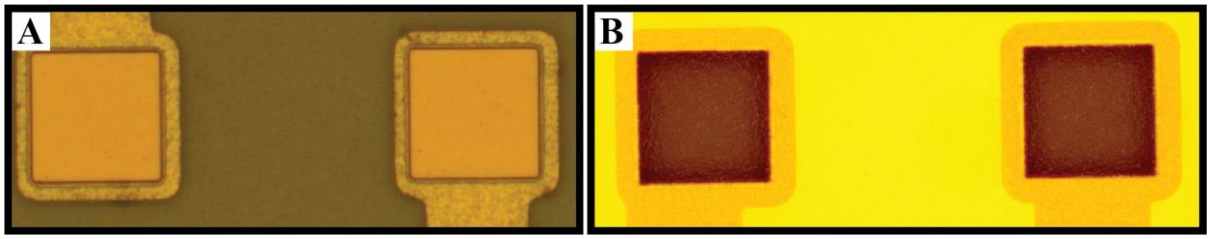

Figure 4.11 TiN surface after DRIE, with protective layer (A), without protective layer (B)

4.2.6 Customizability and CMOS compatibility

Microelectrode arrays of varying configurations and with contacts of different dimensions were fabricated. Arrays and electrode contacts can indeed be customized when designing the fourth and the fifth photomasks, respectively patterning metal layers and polyimide contact openings (Figure 4.6 D, E). The smallest electrode contacts manufactured within the current work were the 'square' design with 80 µm × 80 µm, i.e. an area of 6400 μm^2 (0.0064 mm^2 or 6.4×10^{-5} cm^2). Another electrode array, designed and manufactured, was actually comprising two distinct electrode contacts, a smaller one with 80 µm × 2000 µm, i.e. an area of 160000 μm^2 (0.16 mm^2 or 0.0016 cm^2), and a larger one with 500 µm × 2000 µm, i.e. an area of 1×10^6 μm^2 (1 mm^2 or 0.01 cm^2). Figure 4.12 shows the two electrode arrays described above.

In Figure 4.12 A, 'square' electrode contacts are visible, as well as patterned interconnects underneath the second polyimide layer. In the 'square' design, the pitch between electrodes was set to 60 µm. An increased number of contacts could, however, be achieved with the microfabrication process and altering photomask design, by reducing the pitch to 5 µm, for example. A total of 24 electrode contacts (80 µm × 80 µm) could then be patterned in a 2 mm long space, meaning an increment from the current 14 × 1 array to a 24 × 1 array, keeping the same electrode area. However, such increase in the overall number of electrodes brings up new design challenges related to dimensions of the routing with the outside. Routing of silicon dies with the outside is a topic that will be addressed in Section 4.4, but the bottom line is that requirements derived from target applications shall be used when designing photomasks for the microfabrication process. In Figure 4.12 C, an array is shown with its two larger contact areas of 0.16 mm^2 and 1 mm^2. The TiN on electrode contacts gives the brown color to the exposed areas, after the protective aluminum is etched using the PES-type wet etchant, composed of phosphoric, acetic and nitric acid mixture (77%, 19%, 4% respectively).

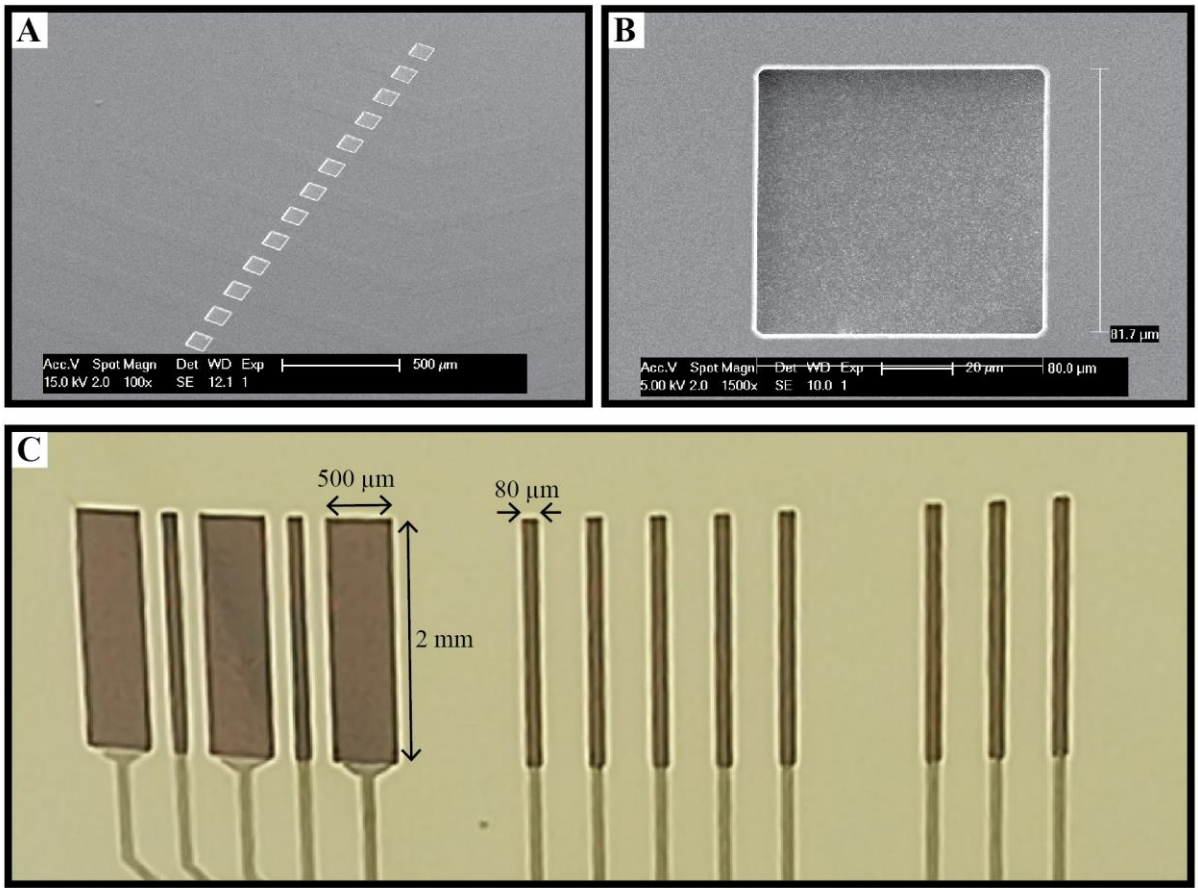

Figure 4.12 Fabricated TiN microelectrode arrays. A) SEM image of the 'square' design – an array comprising 14 contacts with an area of 80 µm × 80 µm, distributed over a total length of about 2 mm and a contact spacing of 60 µm. B) Close-up view of one square contact. C) Optical microscope image of the 'cortical' design – an array comprising 13 contacts, 10 of which are 80 µm × 2000 µm and 3 are 500 µm × 2000 µm. Background yellow color corresponds to polyimide, brown color corresponds to exposed TiN electrode contacts, and the whitish-silver color is given by a 100 nm aluminum layer.

Though inspired by other methods to integrate microelectrodes on polyimide substrates, such as the work of Myllymaa et al on polyimide-titanium-platinum devices [60], and the work of Tolstosheeva et al on polyimide-titanium-gold [61], the microfabrication process here described uses an electrode material which is widely used in CMOS industries, and does so by employing low temperature processes only (< 400 °C), making it compatible with the CMOS back-end process.

4.3 Microfabrication – Results

Figure 4.13 presents two processed silicon wafers with the 7 polyimide-based microelectrode arrays each. The free-standing flexible foils remain attached to the wafer by polyimide tabs, only. Each device contains two silicon dies, a larger one with the 14 bond pads, and a smaller one with mechanical function only. Gradation of colors seen on front side of the wafer – Figure 4.13 A – is due to different

etching zones of the 1 µm thick silicon dioxide. Although the same effect is also present on back side, it is much less pronounced, since single sided polished wafers were used.

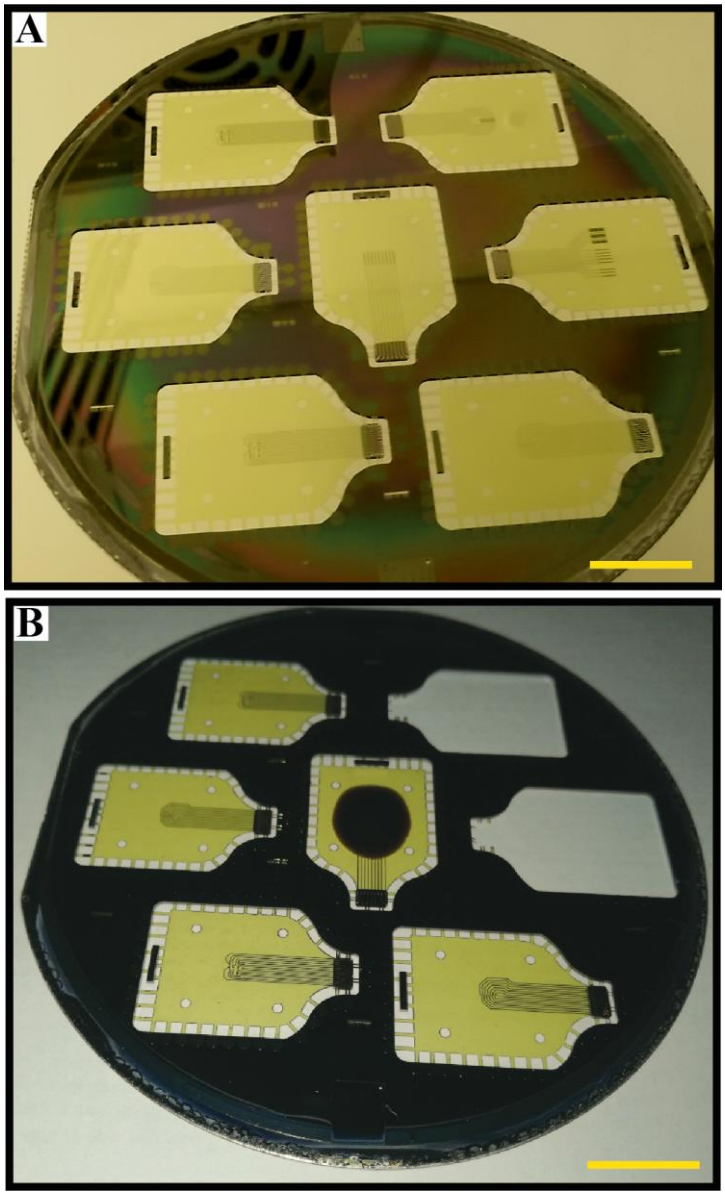

Figure 4.13 The processed silicon wafers. A) Front side photo with all 7 electrodes in it. B) Back side photo with 2 electrodes already detached from it. Incomplete silicon etching is observable in the device in center. Scale bars: 10 mm.

As the figure above show, the polyimide-based TiN microelectrode arrays were successfully fabricated. Though, these results were only achieved after a great deal of optimization at any given fabrication step, as yet discussed in Subsections 4.2.1 – 4.2.6. Several fabrication hurdles had to be overcome, being 1) good step coverage with conductive material (metal) between silicon die and polyimide, and 2) protecting the TiN electrode surface, avoiding reactions during DRIE, the two most challenging ones. Figure 4.14 presents several microelectrode arrays.

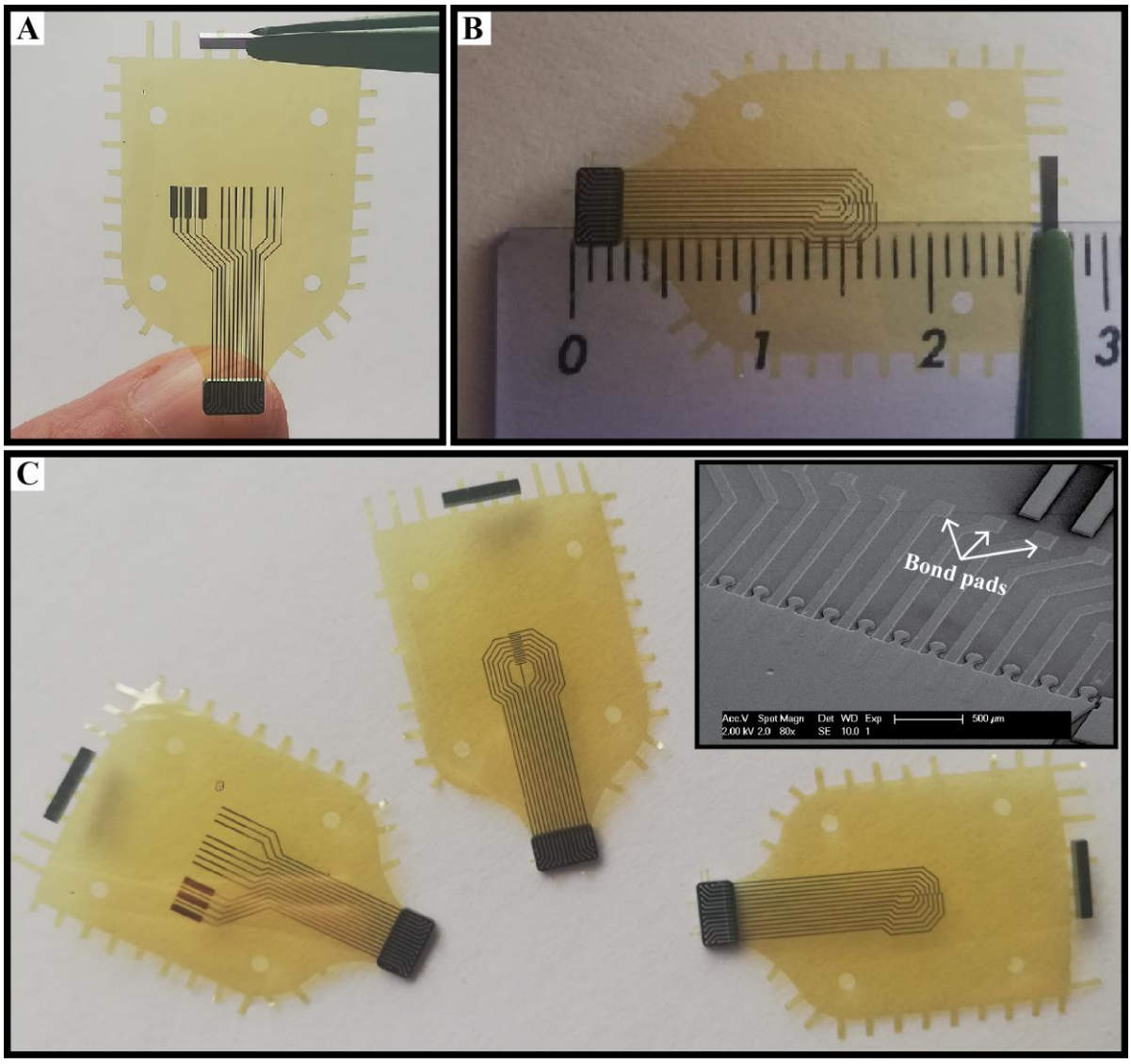

Figure 4.14 Fabricated polyimide-based TiN microelectrode arrays detached from wafers by cutting off polyimide tabs. A) 'Cortical' design. B) 'Square' design. Total length defined between silicon dies is 26 mm. C) Several devices after detachment. Inset on top right shows a detailed SEM picture of bond pads on the silicon die.

4.4 Manufacturing and Assembly of Cuff Electrodes

Simultaneously to the development of the electrode microfabrication process described in Sections 3.2 and 3.3, the possible use of such microelectrode arrays in acute stimulation and recording of the rat vagus nerve had laid the foundations for a parallel work. To use the developed MEAs in an *in vivo* environment, such as the rat vagus nerve, it was necessary to integrate them in larger structures that, in turn, would allow easier handling of thin and flexible polyimide foils. Indeed, when handled alone, thin films of polyimide tend to curl in undesirable and unpredictable ways, thus adhering to non-target structures. Therefore, an obvious advantage of mounting the polyimide-based microelectrodes on larger handling structures is ease of handling and surgical placing. Next, it will be discussed why a cuff electrode

in split-cylinder design is one possible solution to target the rat vagus nerve. Then, it will be discussed how the fabricated polyimide-based MEAs can be integrated in such cuff design.

4.4.1 Requirements for a split-cylinder cuff electrode

The vagus nerve contains sensory and motor components that control organ functions as varied as heart rate and digestion [144]. Vagus nerve stimulation (VNS) of afferent fibers is an approved treatment for epilepsy and depression [145], but the precise mechanism of action of VNS on the central nervous system is still unknown. Cuff electrodes have been used to interface with the rat vagus nerve in various research applications [124, 146].

The vagus is a cranial nerve, connecting the central nervous system to the abdominal region, running through the neck region. In the neck, the vagus is surgically accessible with relative ease, as it is located no further deep than 10 mm from the skin – Figure 4.15 A. The rat vagus nerve is a cylindrical structure with diameters ranging between 200 and 400 μm [147] – Figure 4.15 B. In Figure 4.15 A it is shown that is possible to expose a portion of the nerve by clamping it with sutures and needles.

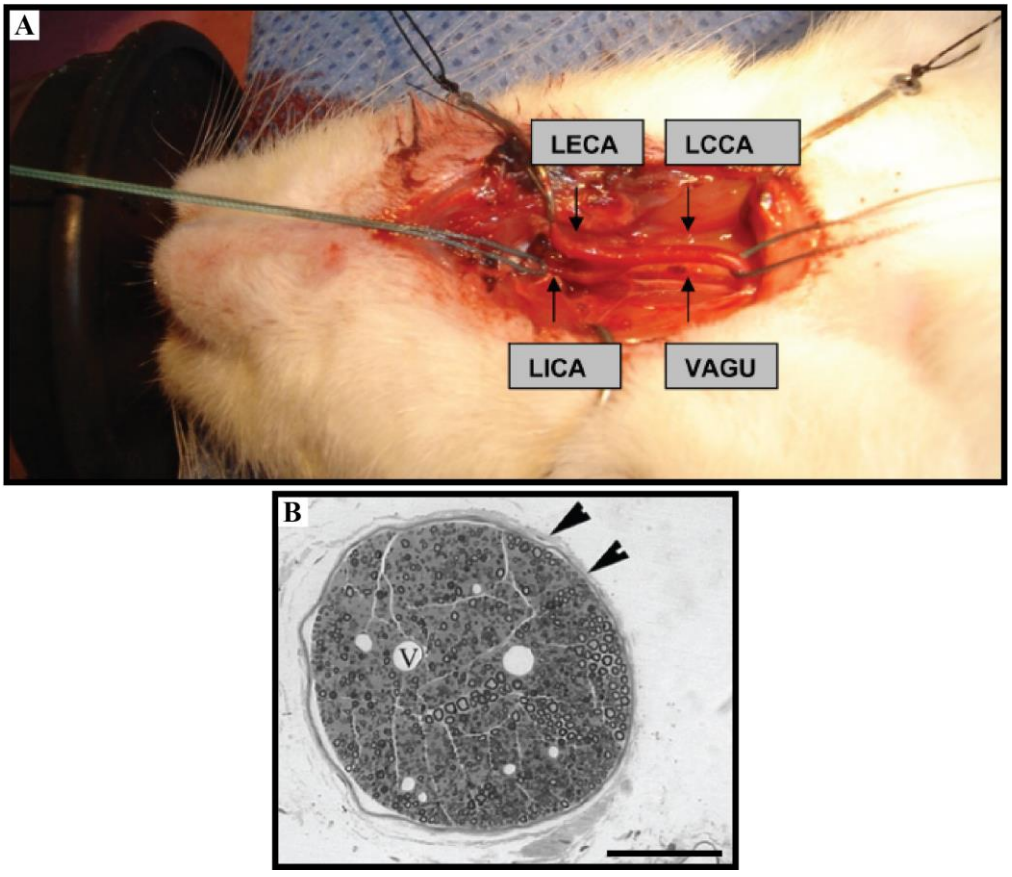

Figure 4.15 Rat vagus nerve. A) Surgical access to the vagus nerve in the neck region of a rat. Important to note that with the use of surgical sutures, it is possible to stretch this nerve after detaching it from the neighboring vascular tissue. LECA, LCCA, and LICA are different branches of the carotid artery; VAGU is the vagus nerve. Image from [148]. B) Cross section of rat vagus nerve. Scale bar: 100 μm. Image from [147].

A maximum width of 10 mm was one anatomical constraint that has been directly translated into an input requirement for the design of the electrode system. That value corresponded to the estimated length of a rat vagus nerve that can be surgically exposed. In addition, the electrode system shall also allow placement of the array at a depth of up to 10 mm from skin surface. Apart from these dimensional requirements, the electrode system would have to allow easy handling for placement and re-positioning around the nerve during acute use, and sharp edges should be avoided in order to minimize risks of nerve damaging. In terms of routing to the outside, silicon dies with bond pads were designed in the microfabrication process to facilitate the use of standard wire bonding technology – see Figure 4.14 C.

Derived from the list of anatomical and surgical requirements above, one solution for interfacing with the rat vagus nerve has been designed and implemented. The solution implemented is based on the operating principle of split-cylinder cuffs, discussed in Subsection 2.6.2. Figure 4.16 depicts the generic operational principle of the split-cylinder cuff, together with required dimensions listed above.

A molding process was developed to realize such cuff structures in polydimethylsiloxane (PDMS). Since a new kind of technical solution to realize cuff electrodes was going to be engineered, the possibility for upscaling or, eventually, downscaling the cuff dimensions was also taken as a requirement. That way, it would be possible to target different nerve structures in the future, using the same kind of molding concept. Also the parts to be used for molding of a split-cylinder cuffs would also have to allow the integration of polyimide-based MEAs onto it.

Split-cylinder cuffs were preferred over spiral cuffs regarding their acute application to rat vagus nerves because split-cylinders were considered by our collaborators as being “easier to manipulate during acute use”, especially if “features for re-positioning are included”.

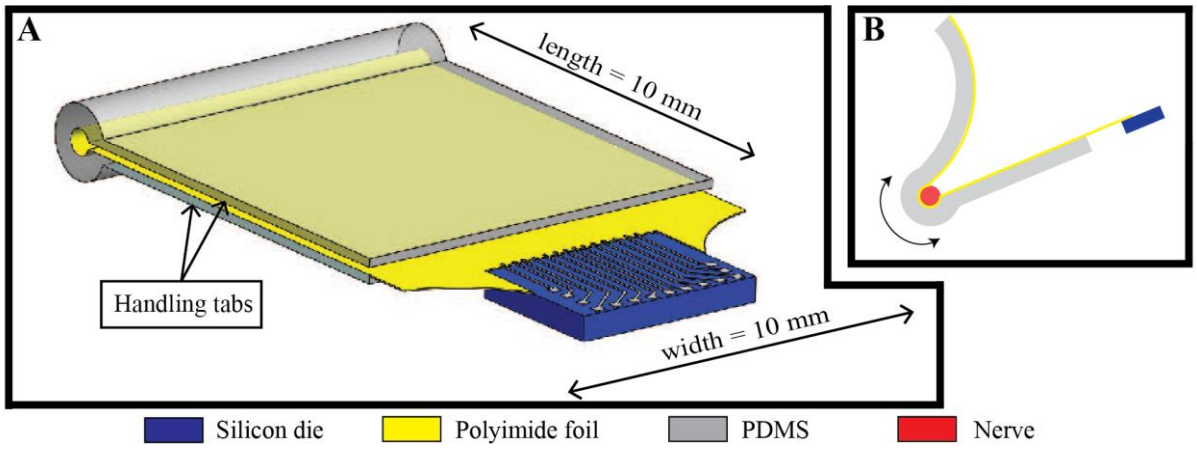

Figure 4.16 Schematic representation of the split-cylinder cuff electrode. A) In closed position. Molded PDMS cuff comprises a cylindrical section and two handling tabs, to which polyimide is attached along their inner surfaces. Required dimensions, discussed in the text, are highlighted. B) Cuff can be opened for placement and re-positioning around the nerve.

4.4.2 Designing a mold for split-cylinder cuffs

As mentioned earlier in Section 3.4, it was decided to design a split-cylinder cuff for interfacing with the rat vagus nerve. For that purpose, a molding process was developed to cast cuff structures in split-cylinder shape, i.e. a cylindrical tube cut open lengthwise. Assembling of polyimide MEAs onto pre-molded PDMS cuff structures then being the final processing step for producing of functional cuff electrodes.

The inner diameter of the cuff was targeted to range between 600 and 700 µm – after assembling of polyimide onto PDMS – making it suitable for sub-mm neural applications, e.g., in the rat vagus nerve with diameters between 200-400 µm. In this case, the distance between electrode and nerve is expected to be between 50 and 250 µm, which are typical distances between extraneural electrodes and nerves. Lertmanorat et al [149] have shown selective stimulation of the cat gastrocnemius nerve (0.3 mm x 1.2 mm) with a flat interface nerve electrode FINE of 0.5 mm opening, i.e. gap nerve/electrode of 100 µm, and Yu et al [46] have shown selective recruitment of fascicles in rat sciatic nerve (1.6 mm x 1.2 mm) using a 1.7 mm diameter cuff, i.e., gap nerve/electrode of 250 µm.

A multi-part mold comprising nine individualized parts was designed in the computer-aided design software Solidworks. These parts served a dual purpose of 1) molding cuff structures in PDMS, and 2) aid in assembling of polyimide foils onto the cuffs. Figure 4.17 shows the nine parts of the mold, how they are aligned and mated. Rods were designed as elementary mating units. Vertical, orange rods shown in Figures 4.17 A and B guarantee mating of all parts involved in the molding of the cuff. Cuff width is defined by the distance between part 4 and part 5, and distance between part 3 and part 6 – per design this was fixed to 10 mm, as listed in the requirements Section 3.4.1 and shown in Figure 4.17. Cuff length is also fixed to 10 mm, as per design of mold parts 1-7. All inner surfaces of the cuff, presented in Figure 4.17, are defined by part number 7. Inner diameter of molded PDMS cuffs was set to 800 µm, defined by diameter of 7a. This value plus assembly of polyimide electrodes was estimated to yield an inner diameter of final cuff electrode between 600 and 700 µm, as planned. Longitudinal slit that separates the handling tabs is defined by the 200 µm thick plate 7b, thus creating the typical shape of a split-cylinder cuff. Handling tabs are 1 mm thick, as given by the thickness of red and blue parts. Small rods 7c, shown in Figure 4.17 C, were introduced to guarantee that polyimide foils can be aligned with the pre-molded cuffs. This is of importance for the cuff assembly manufacturing step, i.e. mounting and gluing of polyimide thin films on PDMS cuffs. As it was shown in Figure 4.6 B and E in Subsection 4.2.1, circular holes have been designed in polyimide masks for the purpose of alignment. Therefore, holes on polyimide films with 1.05 mm diameter are used for securing these films on 1 mm diameter rods shown

in Figure 4.21 A, thus guaranteeing alignment upon assembly. Part number 8 is used for molding of PDMS around the silicon dies with bond pads and also around the printed circuit boards used for routing with the outside. Tolerances of 10 µm have been included when designing the mold. That way, leakage of PDMS in its low viscosity, uncured state was minimized.

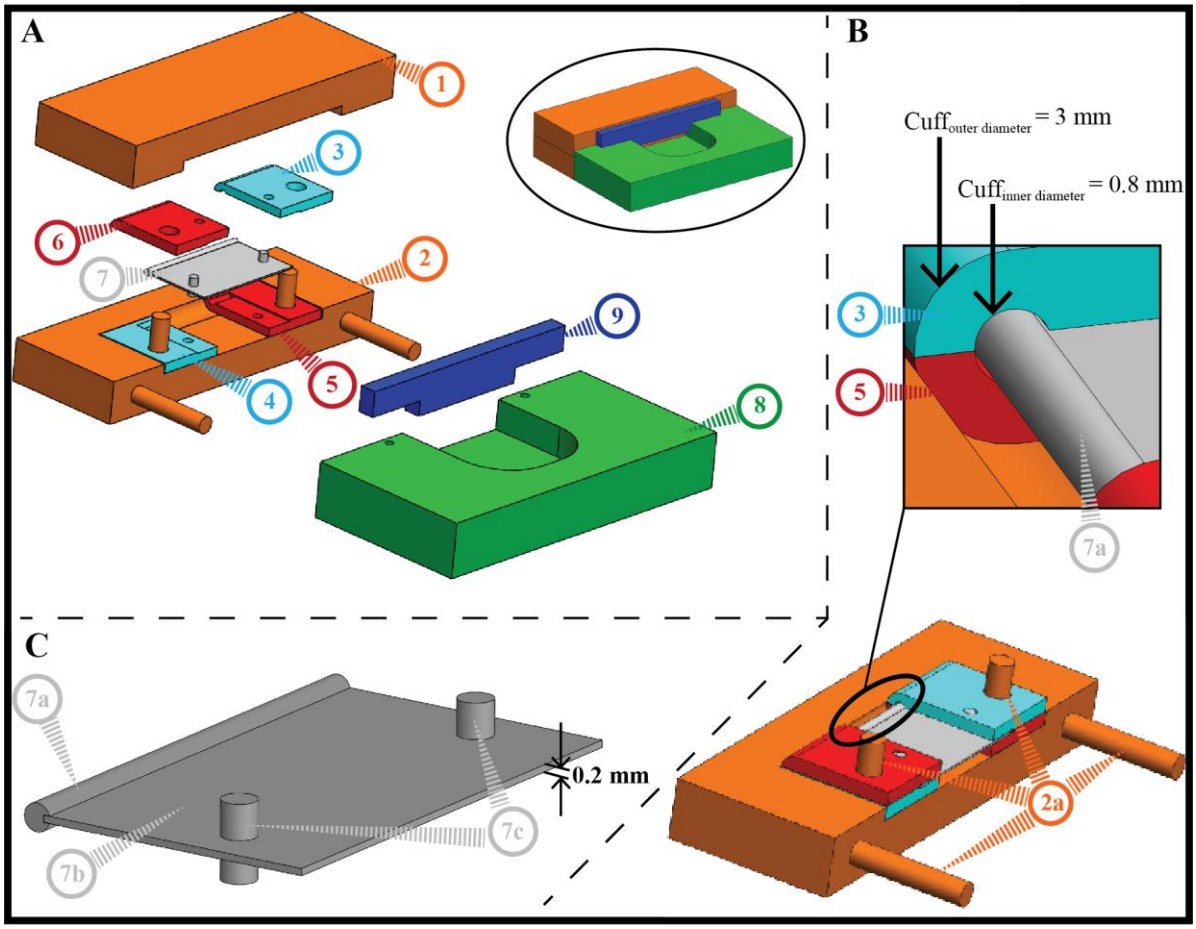

Figure 4.17 Project of the multi-part mold comprising 9 individualized parts for cuff molding, as designed in Solidworks. A) Exploded view. Orange parts (1, 2) define the outer surfaces of the cuff structure. Red (3, 4) and blue (5, 6) parts define the thickness of tabs used to open, close and handle the cuff. These parts (3-6) also shape the cuff outer diameter and serve as support structures for part 7. Part number 7 defines the inner surfaces of the cuff structure – namely its cylindrical shape and longitudinal slit that separates the handling tabs. Details on part number 7 are given in B) and C). Part 8 is used to mold PDMS around the silicon die with bond pads, as well as around a printed circuit board that routes with the outside. Part 9 is used to avoid joining of the two handling tabs during molding. Inset in the top right corner shows the fully assembled mold. B) Bottom figure shows a partially assembled mold and details 4 rods (2a). Two vertical rods align and mate all parts relevant to cuff molding (1-7). Two horizontal rods align and mate cuff molding parts with part 8, used for over molding of silicon die and PCB. Top inset figure details parts relevant for molding of cylindrical cuff structures – rod that defines the cuff inner diameter (7a) is 0.8 mm in diameter, whereas the outer diameter (3 mm) is defined by round shaped surfaces in parts 1 and 2. C) Part number 7 and its sub-parts are detailed. Part 7 is an assembly of 7a) a cylindrical rod that shapes the cuff cylindrical part, 7b) a rectangular, 200 µm thick plate that creates the longitudinal slit typical of split-cylinder cuffs, and 7c) two vertical rods, with 1 mm diameter, used for assembling of polyimide foils onto pre-shaped cuffs, by securing of thin polyimide films with holes.

4.4.3 Mold fabrication and molding of dummy cuffs

The customized multi-part mold, which the design has been presented in the previous Section, was fabricated by a machinery workshop (DEMO) at TU Delft. All parts were fabricated in stainless steel, a material that guarantees good mechanical resistance and durability. Also it is easy to clean in between molding runs. Parts 7a and 7b were fabricated by electrical discharge machining (EDM) or spark machining, by which material is removed from working part by a series of rapidly recurring current discharges between two electrodes. All other parts were fabricated using conventional milling machines. Figure 4.18 shows the fabricated nine parts of the customized mold.

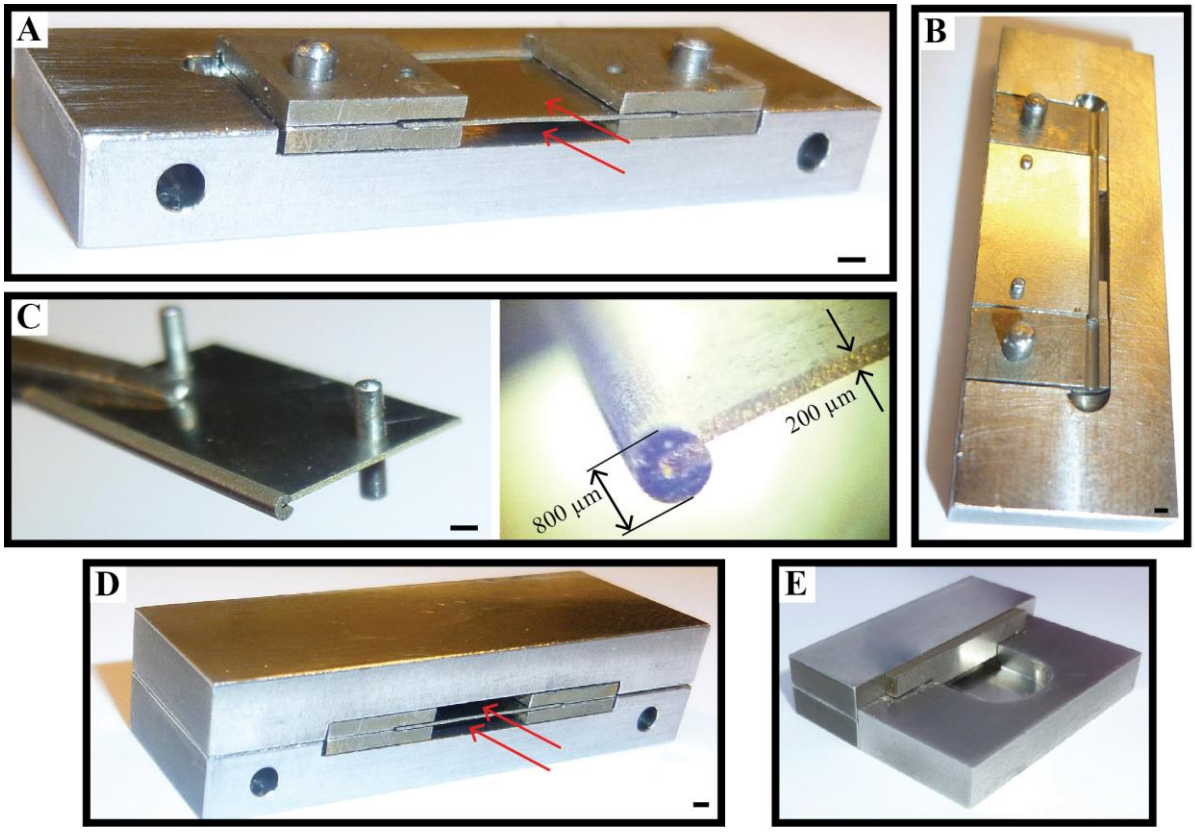

Figure 4.18 Customized mold comprising nine individualized parts, fabricated in stainless steel. A) Front view of parts 2-7. Arrows point to space for handling tabs. B) Top-side view of parts 2-7 showing part 7a fitting into dedicated grooves on parts 4 and 5. Vertical rods for mating are also visible. C) Detailed view on part 7 with all its sub-parts assembled. On the right a detailed view on a groove fabricated by electrical discharge machining in 7a, allowing 7b to be mated into it. D) Assembly of parts 1-7, with arrows pointing into the handling tabs spaces, through which PDMS is poured into the mold. E) Complete assembly of the mold. Scale bars: 1 mm.

Assembly and disassembly of the different parts is straightforward and relatively easy. Ultrasonic cleaning in isopropanol enables complete removal of thin films of PDMS between molding runs, which is very convenient for the next assembly. Without such, assembly of parts, new molding, and de-molding

can be cumbersome. After pouring of PDMS into the mold, and closing it, curing of PDMS takes around 1 hour in convection oven at 80 °C. Figure 4.19 presents a dummy cuff after de-molding.

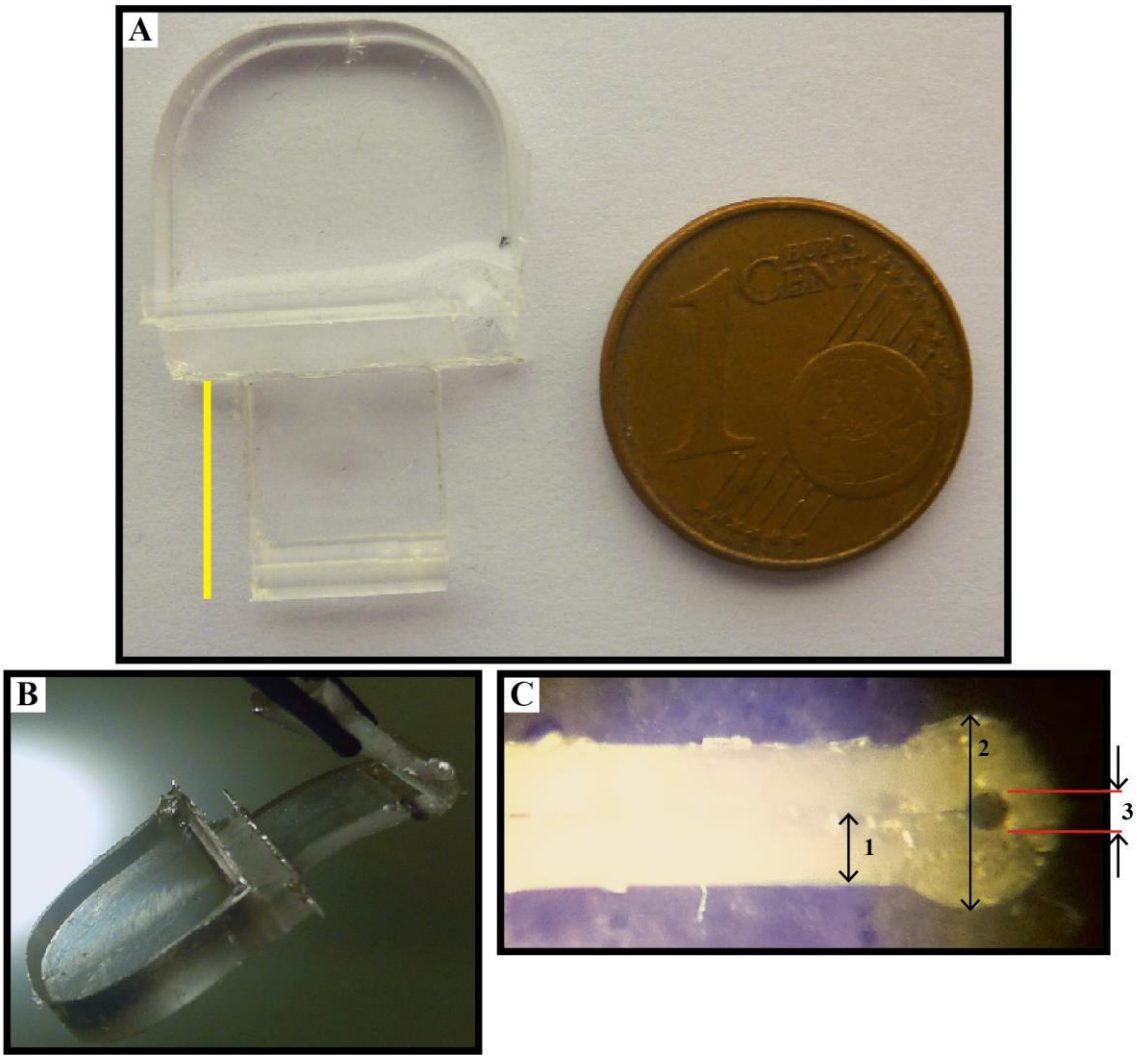

Figure 4.19 Dummy split-cylinder cuff in PDMS. A) Dummy cuff after de-molding. Yellow bar equals to 10 mm long and corresponds to the cuff portion of the molded structure, the remaining bulkier PDMS is where the silicone die and PCB are intended to be. B) Manipulating the handling tab with a tweezer for cuff opening. C) Optical microscope, side view of the cuff cross section. 1 = 1 mm, 2 = 3 mm, 3 = 0.8 mm. The slit separating the two handling tabs is also visible here.

The top handling tab can be manipulated to open and close the split-cylinder cuff, while its counterpart, the bottom tab, remains attached to the bulk PDMS that is intended to protect the silicon dies, wire bonding, and the printed circuit board.

4.4.4 *In vivo* validation of dummy cuffs

The design of dummy cuffs molded in PDMS has been validated *in vivo* in rat vagus nerve. First the rat vagus nerve was surgically accessed in the neck region, and neural tissue was identified and isolated from neighboring structures (e.g., blood vessels, muscle tissue). Then the nerve was kept it

tension with the support of surgical suture lines – Figure 4.20 A. With the help of a pair of surgical tweezers, the dummy cuff is opened by grabbing of the handling tabs. One tab is inserted under the vagus nerve, and then it is pulled, so that its cylindrical portion cuffs around the cylindrical nerve – Figure 4.20 B.

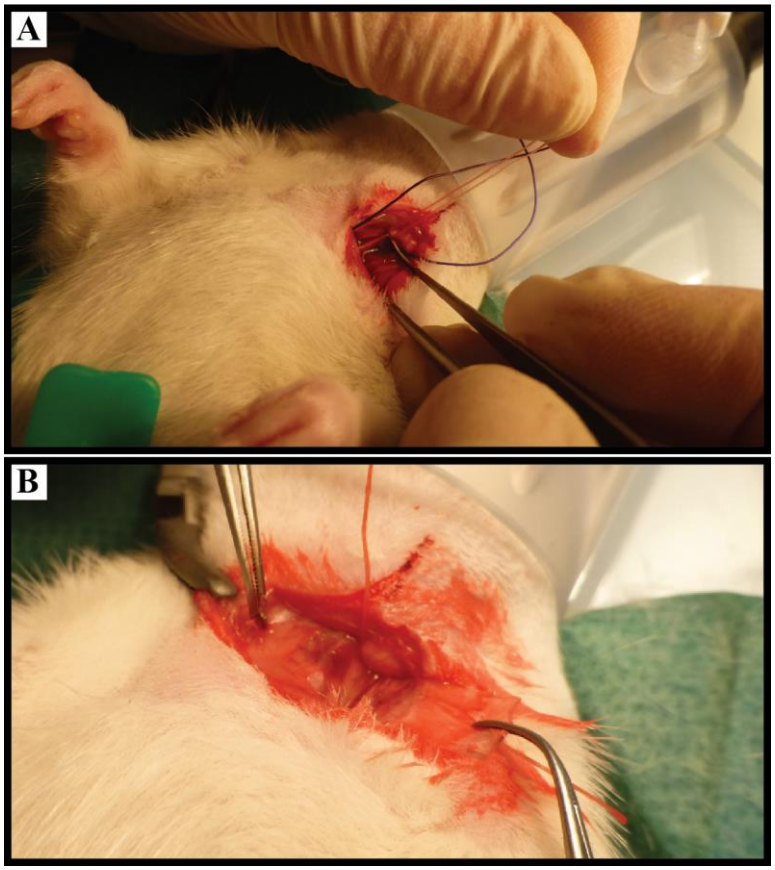

Figure 4.20 *In vivo* use of PDMS split-cylinder dummy cuff. A) Rat vagus nerve is surgically exposed. B) The cuff is handled and opened with two surgical tweezers and placed around the rat vagus nerve.

4.5 Assembling Polyimide-based MEAs onto the Cuffs

As shown before the polyimide layers contain four holes each. These holes are 1.05 mm in diameter, i.e. 50 micron larger than the small aligning rods of the mold. During the design phase of photomasks, the necessary alignment between electrode arrays and holes in polyimide layers was taken into consideration. This way, by clamping of polyimide foils into those rods, alignment of TiN arrays in the cylindrical channel of the cuff is guaranteed. After detachment of polyimide-based MEAs from wafers, the silicon die with bond pads is glued to a customized printed circuit board and then wire bonding is done. The PCB was designed for housing an 18-pin neuro connector from Omnetics. This PCB is only for routing of microelectrode arrays to the outside, thus enabling electrochemical characterization of TiN electrodes,

thus no active electrical components are part of it. Figure 4.21 depicts parts of the assembly process of polyimide foils into cuffs.

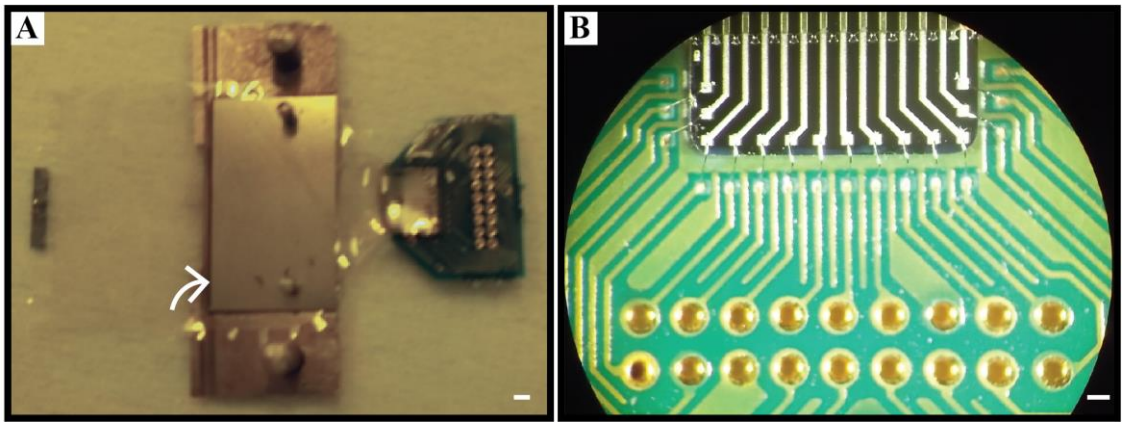

Figure 4.21 Assembly of polyimide foils into cuffs. A) Clamping of polyimide foil in the 1 mm thick vertical rods, preparing the foil for being curved and folded over the cylindrical horizontal rod with 0.8 mm diameter. The following assembly step is the folding indicated by the curved arrow. Scale bar: 1 mm B) Close-up of PCB, showing bonding wires and the 18 gold plated vias for mating of the Omnetics 18-pin neuro connector. Scale bar: 200 µm.

The two holes on polyimide foils that are closest to silicon die are mated on mold parts numbers 4 and 5 using the rods, and after the metal plate (mold part number 7) is placed on top (Figure 4.21 A). Then, polyimide foil is curled using the 0.8 mm diameter, horizontal rod (part mold 7a) as axis of curvature. Mold parts 3 and 6 are then placed on top, thus fixing the polyimide foil. At this point, the electrode contact openings are facing inwards, at the cylindrical rod 7a. To the back side of polyimide (opposite side of electrode contacts) is then manually applied a silicone adhesive layer of MED-2000 (NuSil). Another layer of MED-2000 is subsequently applied to the inner surfaces of a dummy cuff. The PDMS dummy cuff with adhesive is then clamped around the polyimide foil and pressure is applied. After curing of adhesive (24 hours at room temperature), parts of the mold are disassembled, and the newly assembled cuff with polyimide on PDMS is released from it. An example of a fully assembled split-cylinder cuff electrode is shown in Figure 4.22.

4.5.1 Scanning of fully-assembled cuff electrode

After assembling of cuff electrodes, one sample has been imaged thus revealing answers to questions like *"What is the diameter of the cuff electrode after assembly?"* or *"What is the final gap between polyimide and PDMS in the assembled device?"* Figure 4.23 shows two cross sectional images of an assembled cuff electrode, obtained by micro computerized tomography, thus characterizing the cuff mechanically. The cross sectional plane shown in Figure 4.23 A highlights that the maximum gap found between the bulky PDMS cuff structure and the glued polyimide foil is 80 µm. This means that the final

diameter of the cuff electrode is around 640 µm. Silicone adhesive is present in large portions of the PDMS-polyimide interface, alongside with some small void regions. In Figure 4.23 B it is shown a cross section image of handling tabs, highlighting a separation of 270 µm between them. Adhesive thickness is, in this area, lower than that of the polyimide foil.

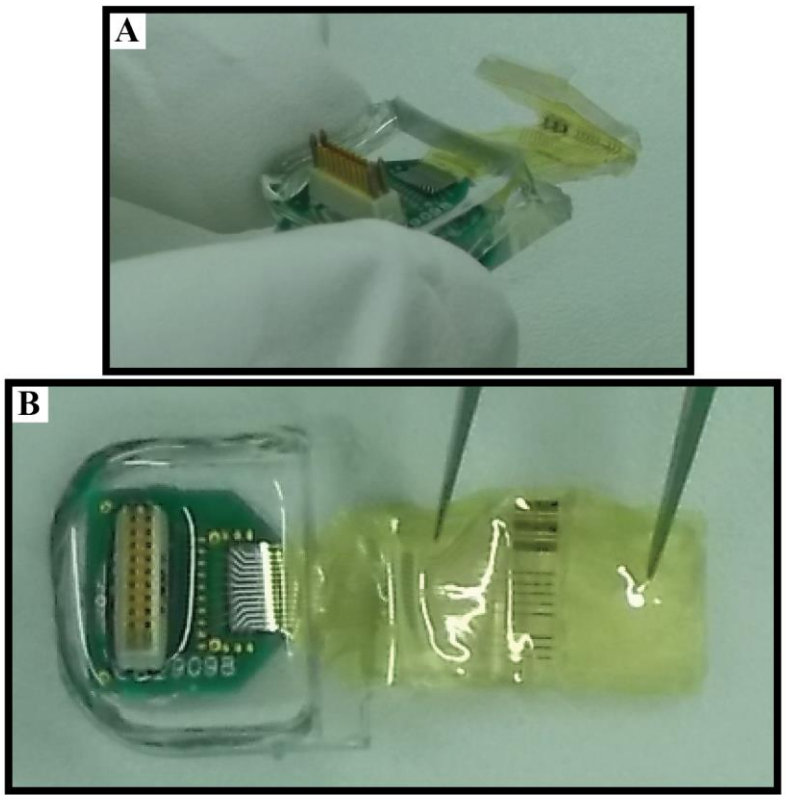

Figure 4.22 Split-cylinder cuff with integrated polyimide-based, TiN microelectrode array. A) Cuff in its "closed" position remains partially opened, due to residual stress between polyimide and PDMS. B) Fully opening of the cuff with a tweezer. Brown TiN contacts can be seen as well as the bonding wires connecting pads on silico die to pads on PCB. An 18 pin Omnetics neuro-connector establishes the interfaces with the external electronics.

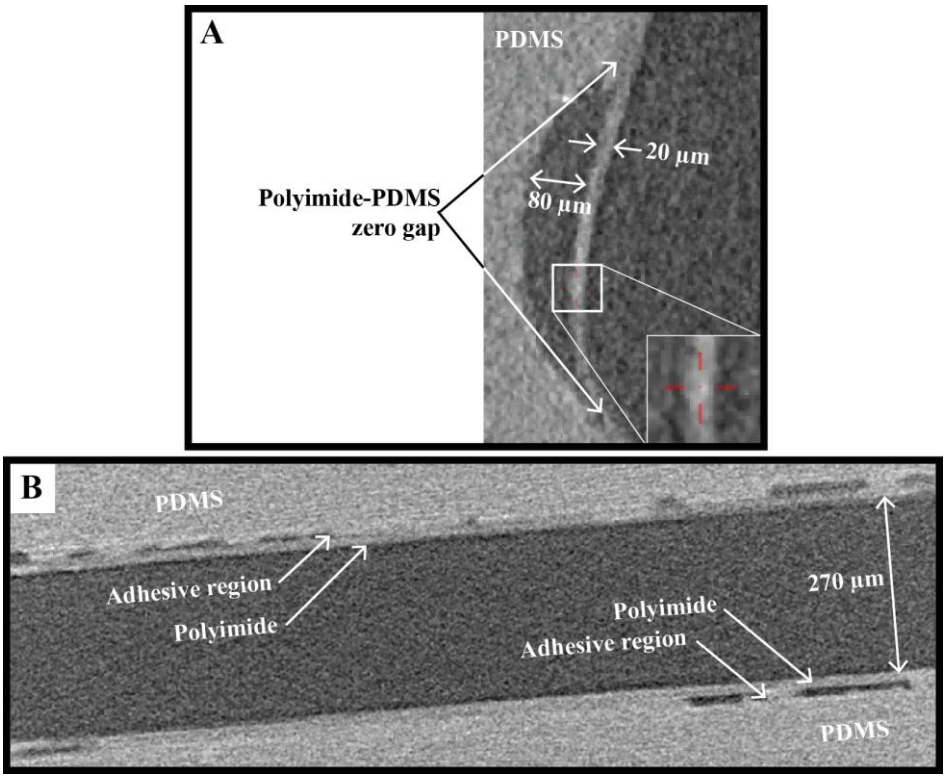

Figure 4.23 Micro-CT images of an assembled split-cylinder cuff with integrated microelectrode array. A) Cross sectional plane of the cuff electrode, detailing its cylindrical portion. Polymers (PDMS and polyimide) are light gray and air is dark gray. The polyimide foil is 20 µm thick and the maximum gap between PDMS and polyimide foil is of 80 µm. Close to that maximum value, the gap between polyimide and PDMS decreases. B) Micro-CT of the handling tabs. Gap between polyimide and PDMS is lower than 20 µm, and the separation between the two stripes is 270 µm.

5 Electrochemical Characterization of TiN Micro and Macroelectrodes

The microfabricated polyimide-based, TiN MEAs have been characterized from an electrochemical perspective. As discussed in Chapter 3, three electrochemical characterization methods were employed – electrochemical impedance spectroscopy (EIS), cyclic voltammetry (CV), and voltage transient measurement (VTM). All electrochemical measurements were done using a three-electrode configuration with TiN electrodes as working electrodes, a large area platinum counter electrode (approx. 30 mm x 30 mm), and an Ag|AgCl reference electrode – see Figure 5.1. All measurements were carried out at room temperature. All potentials reported are relative to the Ag|AgCl reference. As mentioned in Sections 3.2 and 3.3, TiN of three distinct areas were characterized in the present Thesis: 6400, 160000, and 1000000 μm^2 – see Figure 5.2. This way, electrochemical properties of TiN could be characterized for both, micro and macroelectrodes. The electrolyte used in all experiments was a phosphate-buffered saline (PBS, 1X, 62 Ω·cm) at pH 7.4.

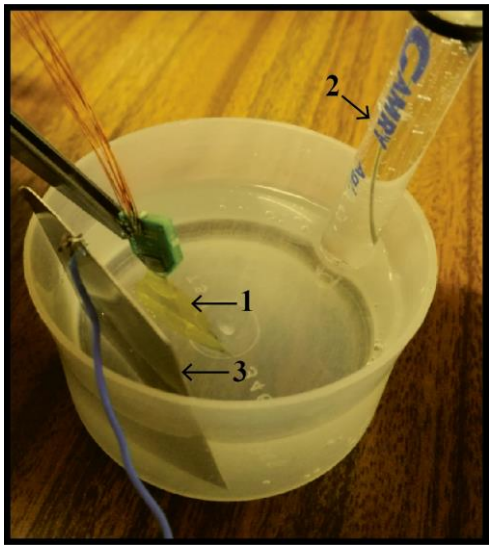

Figure 5.1 Photo of a three-electrode electrochemical cell used in the Thesis. 1: working (or active) TiN electrodes under test; 2: silver-silver chloride (Ag|AgCl) reference electrode from Gamry; 3: large platinum counter electrode, used for current sink.

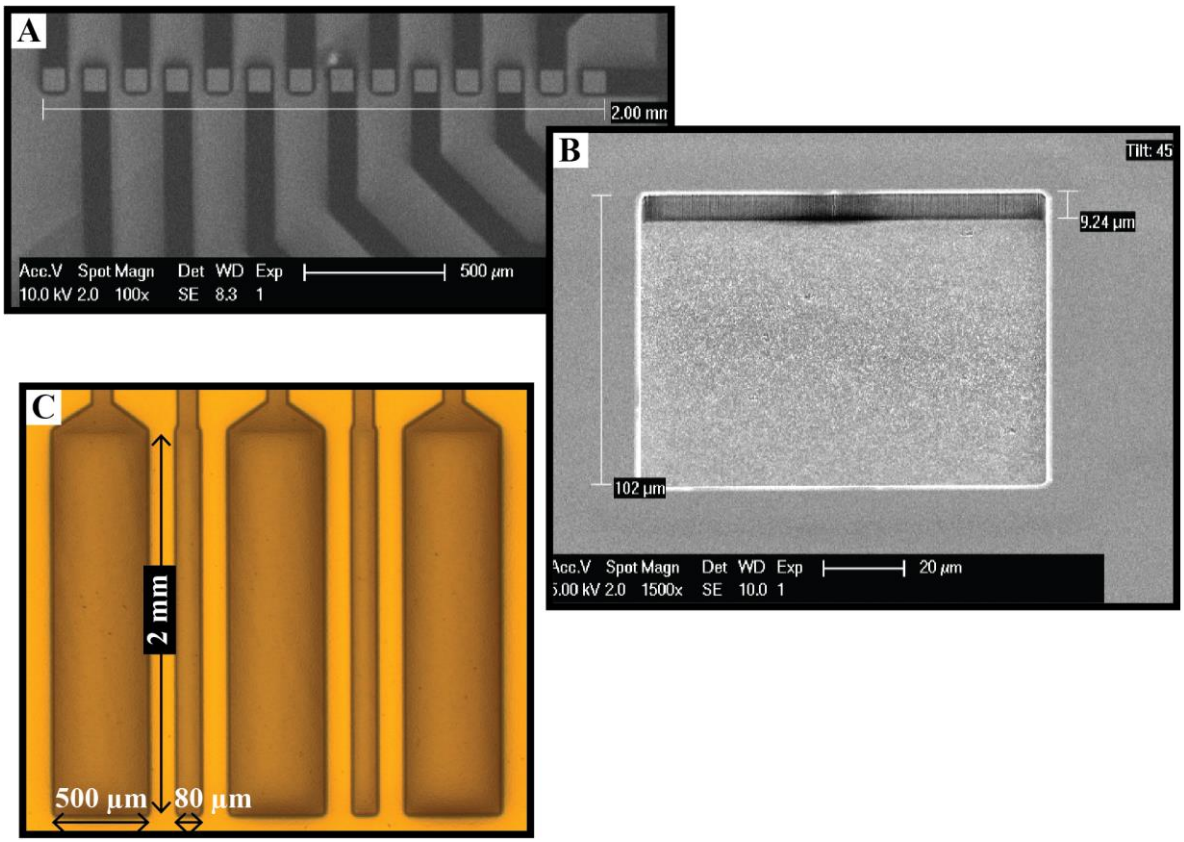

Figure 5.2 Fabricated TiN electrodes that have been electrochemically characterized. A) SEM image of 14 microelectrodes in a 2 mm long, linear array. B) SEM image of one 80 µm × 80 µm microelectrode contact (area = 6400 µm²) with polyimide vertical walls, defined by anisotropic etching. This image was acquired with wafer at a 45° angle. C) Optical microscope image of 160000 and 1000000 µm² electrode contacts, respectively the narrower and the wider contacts.

Regardless of the equipment used for data acquisition – a potentiostat in the case of EIS and CV and an oscilloscope for VTM were used – all data has been post-processed and plotted in Origin® Lab software. The amount of electrode contacts that have been tested differed among different tests. One reason for that is because some tests are destructive to the electrodes, e.g., polarizing the electrode outside of its safety limits. So, while minimizing the amount of destructive testing, that naturally lead to a higher number of non-destructive testing like spectroscopy measurements and a lower number of (potentially) destructive testing like voltammetry and voltage transients. An overview on the total number of electrode contacts tested per electrode area per measurement technique is given in Table 5.1.

Table 5.1 TiN electrode contacts that were electrochemically tested and for which results are presented in this Chapter.

		Area of electrode contact (μm²)		
		6400	**160000**	**1000000**
Electrochemical testing method	**EIS**	20 (2 wafers)	10 (2 wafers)	2 (1 wafer)
	CV	3 (1 wafer)	3 (1 wafer)	2 (1 wafer)
	VTM	10 (2 wafers)	5 (2 wafers)	2 (1 wafer)

5.1 Electrochemical Impedance Spectroscopy

In vitro impedance spectroscopy was acquired with a Gamry Reference 600 potentiostat combined with the Gamry Framework™. The 3-electrode configuration and saline used were described earlier in this Chapter. The impedance spectra were characterized between 1 Hz and 1 MHz at open circuit applying an *ac* signal equal to 10 mV rms sine wave. After preparation of the electrochemical cell, the open circuit potential (potential in working electrode versus potential in reference electrode, with zero injected current) was allowed to reach an equilibrium. Typically a time interval of 30 to 60 minutes was allowed after setting up of electrochemical cell and before running first experiments.

Figure 5.3 A and B shows the EIS spectra of twenty of the smallest microelectrodes with an area of 6400 μm² (80 μm × 80 μm), respectively their impedance magnitude and impedance phase. The samples exhibit a time constant behavior, i.e., a capacitive response in parallel with a resistive response which is typical of a metal-electrolyte interface, as discussed in Chapter 3. Impedance magnitude behavior can be analyzed over three distinct frequency intervals: 1) low-frequency region (below 100 Hz), where $|\mathbf{Z}| = \mathbf{R}_p + \mathbf{R}_e$, with dominant polarization resistance; 2) mid-frequency region between 100 Hz and 10 kHz with nearly linear dependence between impedance magnitude and stimulation frequency; and 3) above 10 kHz, magnitude is less frequency dependent than for lower frequencies, and the total impedance is close to the electrolyte's resistance (R_e). Regarding the impedance phase, it remains predominantly capacitive up to 10 kHz, with an angle between -60° and -80°. For frequencies above the 10 kHz, the phase shifts rapidly to resistive (reaching an interval between -30° and -10°). Proxy values of impedance magnitude at 1 kHz are highlighted.

From the two 14 × 1 microelectrode arrays (shown in Figure 5.2 A) that have been chosen from 2 different wafers and subjected to EIS testing, eight electrode contacts have presented much higher impedance magnitudes ($|Z|_{1\ kHz}$ > 500 kΩ) with associated phase rotations, indicated by phase angle

near zero degrees below 1 kHz. This is indicative of a deficient interface electrode-electrolyte, when compared to the fully functional interfaces reported above. These electrodes were then disabled and not used for any further testing.

Figure 5.3 C and D shows the EIS spectra of ten macroelectrodes with an area of 160000 μm^2 (80 µm × 2 mm), respectively their impedance magnitude and phase angle. The EIS spectra of these larger electrodes show a similar behavior to that of the microelectrodes, with slightly prolonged resistive region at higher frequencies (longer plateau above 10 kHz), and with lower impedance magnitudes overall ($|Z|_{avg@1\ kHz}$ = 5.5 kΩ). Phase angle up to 1 kHz confirms a predominantly capacitive coupling.

Figure 5.4 A and B shows the profiles of impedance magnitude and phase for the 3 electrodes under test, the microelectrodes (6400 μm^2) and the macroelectrodes (160000 and 1000000 μm^2). Impedance magnitude decreases with increasing the electrode's area. Particularly interesting is the decrease in electrolyte's resistance at high frequencies with increasing electrode's area. In fact, if the equation proposed by Franks *et al.* [165] for calculation of the electrolyte's resistance:

$$R_e = \rho_{PBS} / 4r \tag{5.1}$$

is applied to the microelectrodes, then electrolyte's resistance equals to 3875 Ω (assuming these contacts are approximated to circles with a radius r = 40 µm). From equation 5.1, it turns trivial that an increment in electrode's area leads to a decrease in the electrolyte's resistance.

5.1.1 Implications of porosity on EIS profiles

Figure 4.4 in the previous Chapter highlighted the near purely resistive behavior of "rough" or "porous" TiN films, exhibiting near-R_e magnitudes across the entire frequency spectrum. Additionally, this is linked with a near zero phase angle across the entire frequency spectrum – also shown in Figure 4.4. On the other hand, magnitude profiles of "smooth" TiN films exhibit an increase for lower frequencies that are in agreement with the profiles achieved in the electrodes in this Thesis.

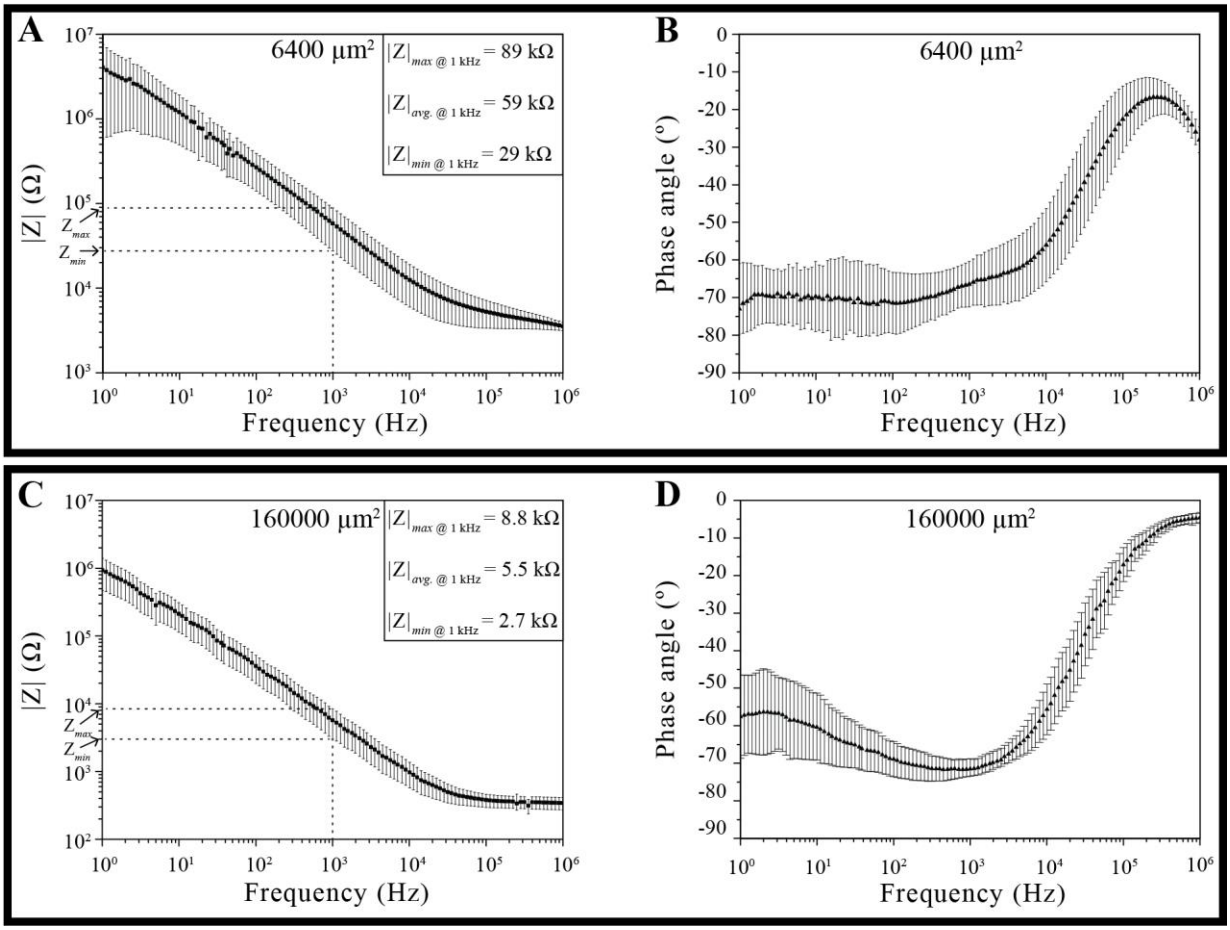

Figure 5.3 Impedance magnitude (A, C) and phase angle (B, D) as functions of the stimulation frequency – Bode plots – for the two smallest TiN electrodes tested. Average and standard deviation values are plotted for any given frequency. (A, B) correspond to measurements on twenty TiN microelectrodes (80 µm × 80 µm). (C, D) measurements on ten macroelectrodes (80 µm × 2 mm). Magnitudes at 1 kHz are highlighted.

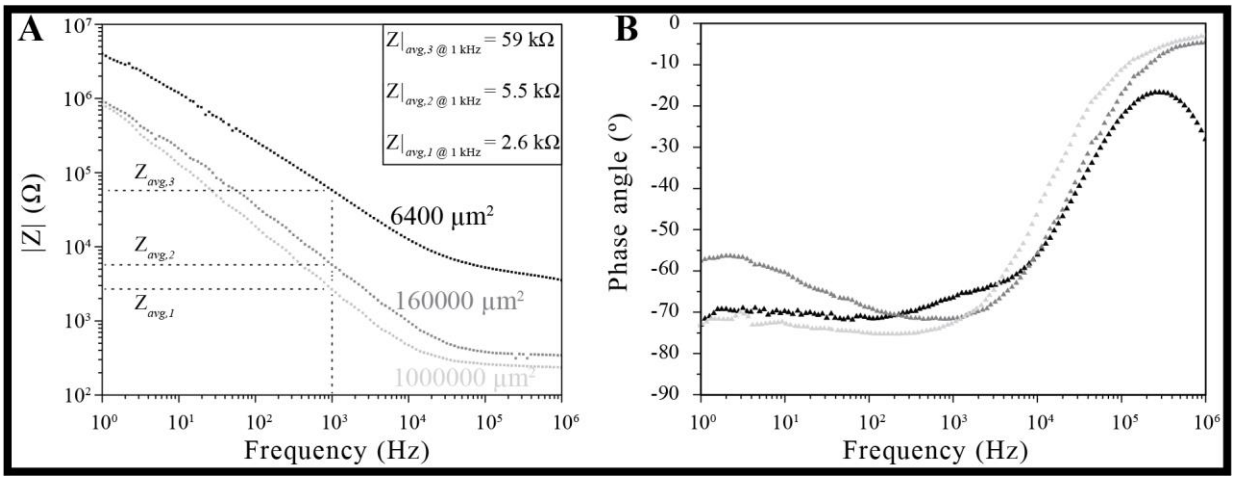

Figure 5.4 Impedance magnitude (A) and phase angle (B) as functions of the stimulation frequency – Bode plots – for the three TiN electrodes tested. Plotting of average points only. Magnitudes at 1 kHz are highlighted.

Morphology of the smooth and porous TiN films is the underlying reason for these differences in their EIS profiles. Considering a transmission line model of pores, as the one proposed by Norlin *et al.* [171] it is clear that, at low-to-mid frequencies, the deeper pores of rougher films become increasingly relevant for charge transfer, maintaining the resistive dominant transfer across the spectrum. For smooth TiN, as the ones fabricated and characterized in the scope of the present Thesis, the capacitive component becomes dominant at low-to-mid frequencies (1 Hz – 10 kHz). At higher frequencies, impedance magnitude approximates to the electrolyte's resistance regardless of film porosity.

5.2 Cyclic Voltammetry

Cyclic voltammetry was acquired with a Gamry Reference 600 potentiostat combined with the Gamry Framework™. The 3-electrode configuration and saline used were described earlier in this Chapter.

5.2.1 Determining the water window

The CV cycling was first performed between potential limits beyond the hydrolysis limits (-1 V and + 1.2 V), represented in a CV curve as large current peaks that correspond to dissolved gas and/or other reactions. The potential values at which large current peaks are triggered define the water window limits. Since cycling outside of safe limits is a destructive test for electrodes, this test was restricted to a limited number of electrodes (8 in total) as shown before in Table 5.1. The TiN voltammogram obtained within and beyond the water window, at a slow sweep rate of 50 mV/s, is shown in Figure 5.5.

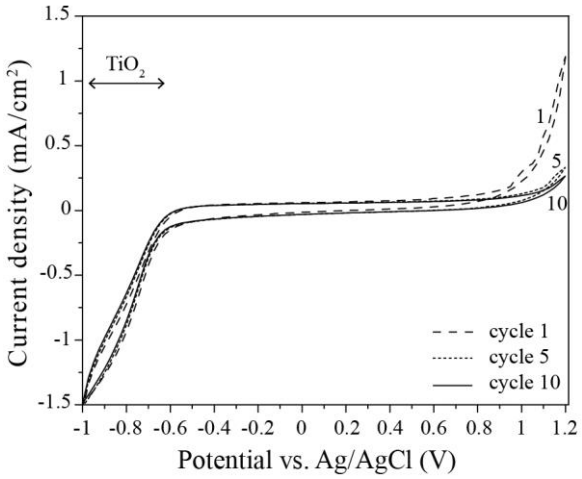

Figure 5.5 Cyclic voltammogram of TiN electrodes in PBS at a sweep rate of 50 mV/s. Plots are shown for cycles number 1, 5 and 10.

This profile of a voltammogram, between -1 and +1.2 V, have been obtained for the three distinct areas. The CV indicates a typical TiN voltammogram profile with no distinct current peaks around zero potential and fast increases in both cathodic and anodic currents, beyond certain potential limits, as

shown for platinum electrodes in Figure 4.5 C. Peaks in the cathodic direction, below -0.6 V, may be attributed to reduction of titanium dioxide with nitrogen formation [178], leading to absorption of hydrogen into the oxide and increased conductivity [171]. Peaks in the anodic direction (above 0.8 V) are perhaps due to oxidation of the reduced oxide, as shown in Figure 3.5 C for platinum, in the Chapter 3. Decrease in anodic peaks (cycle 1 to 5) and subsequent stabilization trend (cycle 5 to 10) of current maximum densities means that the oxide growth achieves a stable thickness. These limits of -0.6 V and 0.8 V are therefore defined as safe potential limits, defining the usually called water window region. Cycling the TiN electrodes between them guarantees safe charge injection through non-faradaic or capacitive reactions, i.e., with reversible redistribution of charge. Provided polarization of the stimulation (working) electrode during a stimulation pulse remains more positive than the water reduction potential and more negative than the water oxidation potential, the stimuli charge density if often considered as "safe" [179].

These limits for safe charge injection are consistent with literature values presented in the Figure 3.5 A. Same water window limits have been reported in the works of Weiland *et al.* for TiN microelectrodes on rigid substrates [163], and in González-González *et al.* [49] on TiN microelectrode cuffs on shape memory polymers. An overview of reference works on TiN electrodes, highlighting key geometrical parameters and electrochemical measures is provided in Table 5.2. A comparative analysis across the different TiN electrode works with varying electrochemical performances is performed in Subsections 5.3.3 and 5.3.4.

Table 5.2 Geometrical surface area and electrochemical properties of TiN electrodes, in some of the reference works and in this Thesis.

GSA	Impedance @ 1 kHz	Water window	Charge injection capacity	Reference
4000 µm²	20 – 30 kΩ	-0.6 V to +0.8 V	550 µC/cm² @ 200 µs cathodic	Weiland *et al.* [163]
6 mm²	242 kΩ (smooth) 203 kΩ (porous)	-0.6 V to +1 V	24 µC/cm² @ 200 µs cathodic (smooth)	Meijs *et al.* [172]
13500 – 139500 µm²	1 – 3 kΩ	-0.6 V to +0.8 V	500 µC/cm² @ 200 µs cathodic	González-González *et al.* [49]
6400 µm² **160000 µm²** **1000000 µm²**	29 – 89 kΩ 2.7 – 8.8 kΩ 2.6 kΩ	-0.6 V to +0.8 V	154 µC/cm² 8.5 µC/cm² - @ 200 µs cathodic	Present work

5.2.2 Studying chemical reactions at the interface

After determining water window for the TiN electrodes, CV was then performed, at slow sweep rate of 50 mV/s and within the no-hydrolysis limits, to study electrochemical behavior and reactions. Figure 5.6 shows voltammograms for the three TiN electrodes within between -0.6 V and 0.8 V. Investigation of electrochemical reactions for potentials between -0.6V and 0.8 V reveals a rectangular-like shape of all TiN electrodes under study, indicative of a capacitive behavior. Small current peaks are visible in the anodic sweep of the microelectrodes (Figure 5.6 A, where numbers '1', '5' and '10' are located), which can be due to adsorption of H into the titanium dioxide formed in the cathodic sweep, leading to an increased conductivity. This chemical reaction is defined as follows [171]:

$$TiO_2 + nH + ne^- \rightarrow TiO_{2-n}(OH)_n \quad (5.2)$$

A decrease in the cathodic peak potentials, as cycle number increases, is an indication that the reduction of titanium dioxide tends to decrease, perhaps due to thinning of oxide/hydroxide layers.

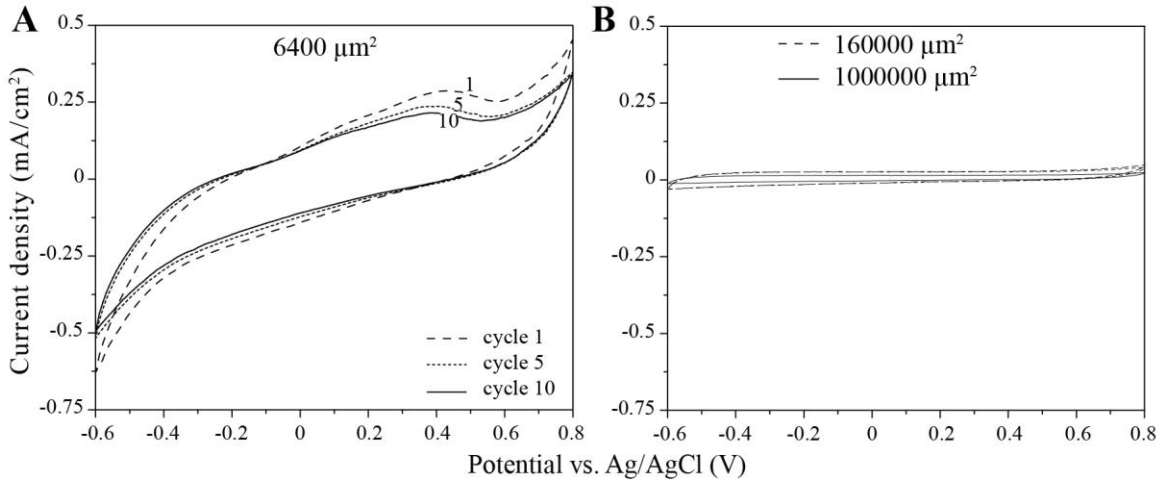

Figure 5.6 Cyclic voltammograms of TiN electrodes in PBS at a sweep rate of 50 mV/s and within water window. A) Voltammogram of the TiN microelectrodes with 6400 µm². Plots are shown for cycles number 1, 5 and 10. B) Voltammograms of the larger TiN macroelectrodes, with 160000 and 1000000 µm².

Absence of noticeable peaks in the voltammograms of larger macroelectrodes (Figure 5.6 B) suggests a lower level of penetration in the TiN pores – as compared to the microelectrodes – thus limiting the occurrence of red-ox reactions. The rectangular-like shape is even more pronounced for the larger macroelectrodes and the total current density achieved is significantly lower due to larger areas through which current is injected into saline.

5.2.3 Studying charge injection and roughness

As discussed in Chapter 3, Subsection 3.3.2, study of cyclic voltammograms and corresponding profiles provides important information about roughness and crystalline structure of the TiN electrodes. It is noteworthy that CV curves of TiN microelectrodes show nearly the same integral areas for slow sweep rates of 50 and 100 mV/s as well as for a high rate of 1 V/s – Figure 5.7. In fact, the charge storage capacity (CSC_c), an indicative value often calculated from integrating the negative current (cathodic phase), is 123, 128, and 126 μC/cm², respectively for the 0.05, 0.1, and 1V/s. Therefore, the amount of charge available for injection into saline is rather constant among different sweep rates of voltammetry. Additionally, the profile of charge injection suffers nearly no change, keeping a shape typical of capacitive injection (rectangular-shaped) regardless of sweep rate. The charge-transfer process is almost completely reversible, if judged only by the amount of charge transferred across the interface, in both anodic and cathodic phases. At a high sweep rate of 1 V/s, no adsorption/desorption peaks could be observed.

Comparing these results with those of Norlin *et al.* [171], it turns out that sputtered TiN electrodes of this Thesis show comparable voltammograms to "smooth" films, i.e., rectangular-shaped at high rates. Moreover, in the work of Cunha *et al.* [180] it has been shown that smoother, Ti-rich TiN films present typical capacitive behavior for slow as well as for fast sweep rates. Rougher, N-rich TiN films tend to have an Ohmic-like voltammogram at high sweep rates.

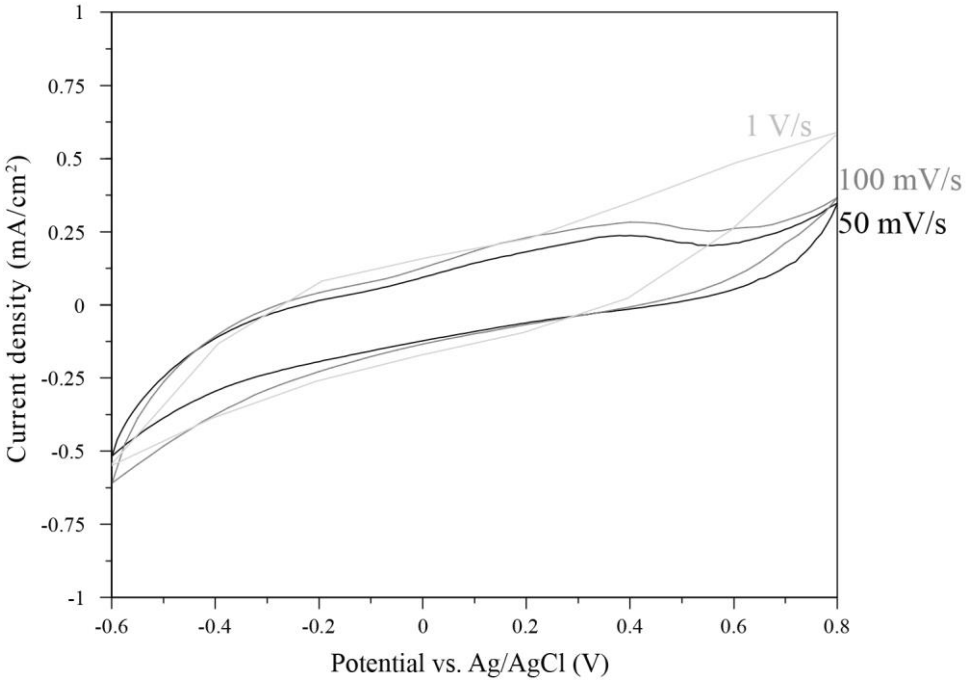

Figure 5.7 Cyclic voltammograms for the microelectrodes (6400 μm²) at sweep rates of 50 and 100 mV/s and 1 V/s.

5.3 Voltage Transient Measurements

The voltage transients were recorded and used to determine pulse parameters (amplitude, width) driving the E_{mc} – the most negative potential after the cathodic phase offset – to nearly -0.6 V. Voltage transients were measured upon stimulation with cathodic-first, charge-balanced biphasic, symmetric square pulses delivered by a Kethley current source model 6221. Acquisition of waveforms was performed with a digital oscilloscope at a sampling rate of 20 MS/s. Origin® Lab was used for post-processing of the raw data. The electrolyte type and three-electrode configuration were used in same way as described for CV – current is injected in TiN working electrodes and is sunk through a large platinum counter electrode; voltage drop is measured between working electrode and a Ag|AgCl reference electrode. VTMs were acquired and post-processed, and according data is shown for 10 microelectrodes (6400 µm²), 5 macroelectrodes (160000 µm²), and 2 macroelectrodes (1000000 µm²). All microelectrodes and smaller macroelectrodes (160000 µm²) were pulsed with 50 and 200 µs of pulse width, with current amplitudes being adjusted, to balance out the total charge injected. An overview on stimulation parameters for each electrode is given in Table 5.3. I_i and I_f are initial and final values of current amplitudes, which correspond to charge per phase values of $Q_{ph,\,i}$ and $Q_{ph,\,f}$. $Q_{inj,\,i}$ and $Q_{inj,\,f}$ are correspondent values of injected current, dependent from geometric surface area of electrodes. In order to determine the charge injection capacity (Q_{inj} or CIC) of TiN micro and macroelectrodes, it must be assessed which value of injected charge ($Q_{inj,\,i,\,...,\,f}$) drives the electrode's E_{mc} potential, in cathodic phase, to a value near, but not more negative, than -0.6 V (lower limit of water window).

Table 5.3 Stimulation parameters – pulse width and current amplitude – used in voltage transient measurements, varying upon GSA of electrodes under test. Corresponding charge values are also given.

GSA (µm²)	Pulse width			
	50 µs		200 µs	
6400	I_i = 64 µA $Q_{ph,\,i}$ = 3.2 nC $Q_{inj,\,i}$ = 50 µC/cm²	I_f = 300 µA $Q_{ph,\,f}$ = 15 nC $Q_{inj,\,f}$ = 234 µC/cm²	I_i = 16 µA $Q_{ph,\,i}$ = 3.2 nC $Q_{inj,\,i}$ = 50 µC/cm²	I_f = 80 µA $Q_{ph,\,f}$ = 16 nC $Q_{inj,\,f}$ = 250 µC/cm²
160000	I_i = 64 µA $Q_{ph,\,i}$ = 3.2 nC $Q_{inj,\,i}$ = 2 µC/cm²	I_f = 300 µA $Q_{ph,\,f}$ = 15 nC $Q_{inj,\,f}$ = 9.4 µC/cm²	I_i = 16 µA $Q_{ph,\,i}$ = 3.2 nC $Q_{inj,\,i}$ = 2 µC/cm²	I_f = 80 µA $Q_{ph,\,f}$ = 16 nC $Q_{inj,\,f}$ = 10 µC/cm²
1000000	I_i = 64 µA $Q_{ph,\,i}$ = 3.2 nC $Q_{inj,\,i}$ = 0.32 µC/cm²	I_f = 896 µA $Q_{ph,\,f}$ = 44.8 nC $Q_{inj,\,f}$ = 4.5 µC/cm²	-	-

To determine $E_{mc,}$ the approach of Leung *et al.* [176] was followed, in which the potential near the end of the interphase gap is used. As the interphase gap was set to 20 µs, E_{mc} values were taken at 15 µs after end of cathodic phase, thus being the most approximate value between measured and real potential values. Electrodes were actively biased to 0 V in between pulses. Due to the high number of electric cables and connections involved in measuring voltage transients, such measurements can become cumbersome and prone to errors. For ruling out erroneous cable routing, it is good practice to measure voltage drop across a resistor before doing so in the more complex electrochemical cells. Voltage drop across a 1 kΩ resistor, presented with a biphasic, cathodic-first, and symmetric square pulse is shown in Figure 5.8. Surely, voltage drop is 1 V when current amplitude is set to 1 mA.

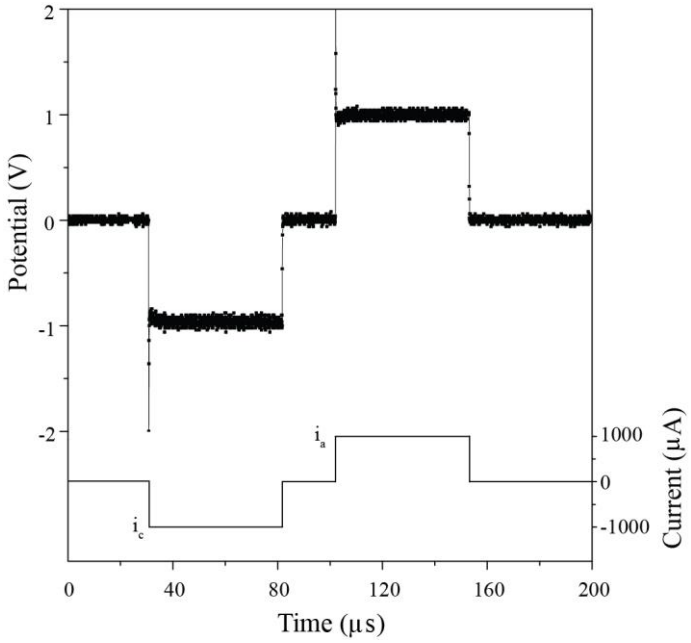

Figure 5.8 Voltage transient of a 1 kΩ resistor. Phase duration (or pulse width) is 50 µs. Pulse amplitude is 1 mA. Interphase gap is 20 µs. Input current is below, output voltage is the signal above.

5.3.1 VTMs of microelectrodes and 160000 µm² macroelectrodes

Figure 5.9 shows voltage transients of one microelectrode (A and B), and one macroelectrode (C and D). Plots are provided for phase durations of 50 and 200 µs. To ease interpretation, plots are restricted to two charge levels per figure (per electrode per phase duration), instead of all charge steps tested in between. For the microelectrode shown here, the maximum negative potential, the E_{mc} value, is -0.25 V and -0.55 V, respectively for 3.2 nC and 9.6 nC per phase. Access voltage, V_a, is surely higher when using a higher cathodic current amplitude of 192 µA (A, black trace). However, that did not have an impact on the maximum negative potential at the end of interphase gap, i.e. variation in V_a is proportional to current amplitude and the E_{mc}.

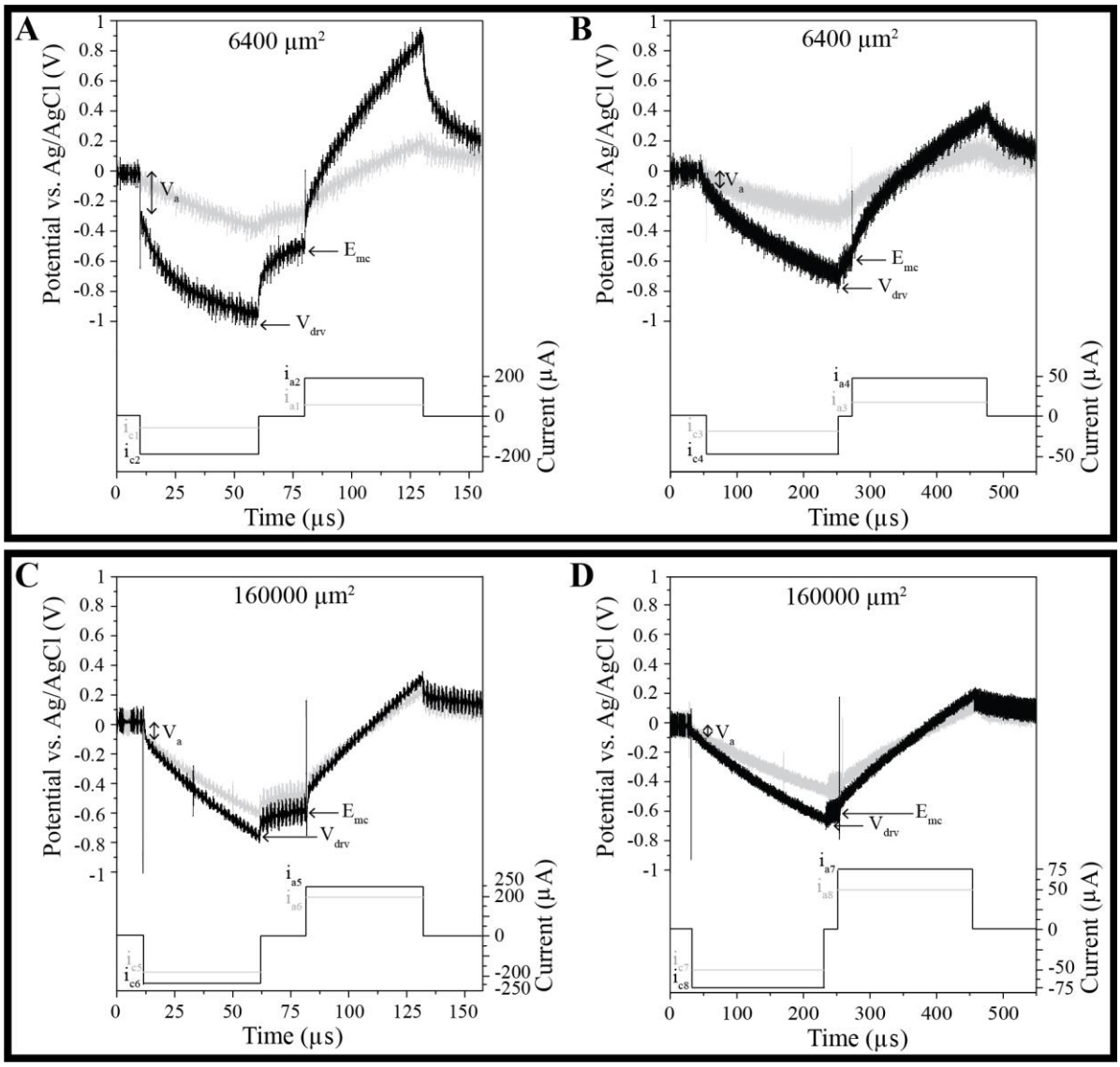

Figure 5.9 Plots of voltage transient measurements of TiN microelectrodes (A, B), and macroelectrodes (C, D). Phase durations of 50 µs (A, C) and 200 µs (B, D). A, B: E_{mc} values are approximately -0.25 V at 3.2 nC/phase (gray trace) and -0.55 V at 9.6 nC/phase (black). C, D: E_{mc} values are approximately -0.5 V at 9.6 nC/phase (gray) and -0.6 V at 14 nC/phase (black). V_a = access potential, E_{mc} = maximum negative potential excursion, V_{drv} = maximum driving potential. i_{c1}-i_{c8} = cathodic currents, i_{a1}-i_{a8} = anodic currents. i_{c1} = - 64 µA, i_{c2} = i_{c5} = - 192 µA, i_{c3} = -16 µA, i_{c4} = i_{c7} = - 48 µA, i_{c6} = - 280 µA, i_{c8} = - 72 µA.

All ten microelectrodes tested presented similar voltage transient profiles. A charge per phase of 9.6 nC drives the microelectrode to a potential of -0.55 V, i.e. near the lower limit of water window (-0.6 V). A charge per phase of 9.6 nC is, for the 6400 µm² microelectrode under test, equivalent to a charge density of 150 µC/cm². Maximum values of charge density that drive the ten microelectrodes to nearly -0.6 V varied between 130 and 180 µC/cm². Charge injection capacity, Q_{inj} or CIC, of TiN microelectrodes is then calculated to be 154 ± 16 µC/cm².

Voltage transients for macroelectrodes are shown in Figure 5.9 (C, D), respectively for pulse widths of 50 and 200 µs. Maximum charge densities between 8.25 and 8.75 µC/cm² drive the E_{mc} levels to close to -0.6 V in the 5 electrodes. Charge injection capacity, Q_{inj}, of TiN macroelectrodes is then 8.5 ± 0.19 µC/cm².

5.3.2 VTMs of 1000000 µm² (1mm²) macroelectrodes

Figure 5.10 shows voltage transients of one large macroelectrode (1mm²) for a phase duration of 50 µs. E_{mc} values, shown under the figure, are -0.05, -0.1, -0.35, -0.53 and -0.58 V, respectively for 3.2, 9.6, 25.6, 38.4, and 44.8 nC per phase.

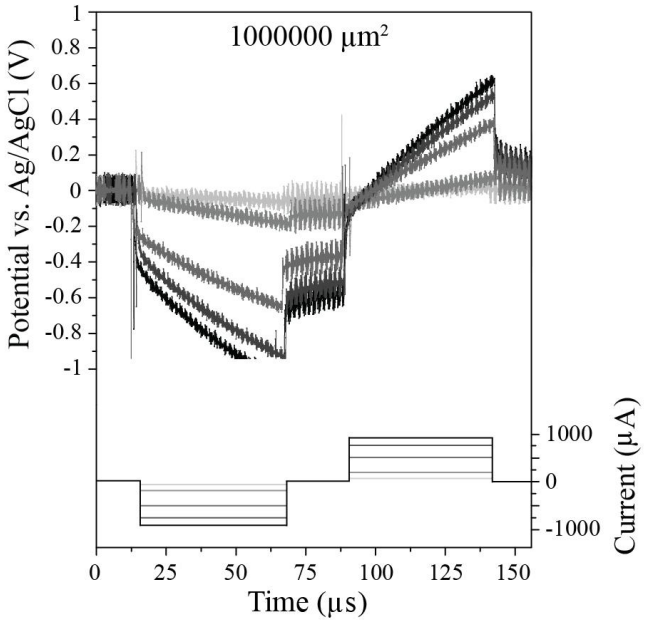

Figure 5.10 Five plots of voltage transient measurements of a 1000000 µm² (1 mm²) TiN macroelectrode. Current amplitudes are: 64, 192, 512, 768, and 896 µA (from light gray to black). E_{mc} values are: -0.05 V, -0.1 V, -0.35 V, -0.53 V, and -0.58 V (from light gray to black). Phase duration is 50 µs.

In the larger, 1 mm² macroelectrode the charge density that drives the E_{mc} potential to near -0.6 V is 4.5 µC/cm². That is therefore its charge injection capacity at a phase duration of 50 µs. Voltage transient measurements of 1 mm² macroelectrodes have not been performed at 200 µs.

5.3.3 Charge injection capacity *vs.* electrode area

Works on stimulation and recording electrodes usually present devices with geometric surface areas of wide ranges – from micro to macro – which surely makes comparison a challenging endeavor. TiN was first introduced as a sensing and stimulation material by Janders *et al.* with a large charge injection capacity of 23 mC/cm² being reported [181], over an electrode area of 83 µm². Weiland *et al.* reported CIC of 550/950 µC/cm² [163], respectively for areas 4000 µm², while much lower CIC of 24

μC/cm² was reported on TiN macroelectrodes with an area of 6 mm² by Meijs *et al.* [172]. These reference results that have been summarized in Table 5.2 suggest an inverse correlation between area of TiN electrodes and their charge injection, similarly to that reported for SIROF electrodes [182]. The results of the present Thesis corroborate such findings across different literature works. Indeed, the 6400 μm² microelectrodes presented a CIC of 154 μC/cm², whereas it decreases to 8.5 μC/cm² in 160000 μm² macroelectrodes.

5.3.4 Charge injection capacity *vs.* deposition parameters

In the work of Weiland *et al.* [163] TiN electrode contacts with geometric surface area (GSA) of 4000 μm², pulsed in PBS with 200 μs long pulses, resulted in a CIC of 550 μC/cm², comparatively higher than in the present study. Rigid, silicon-based probes including low pressure chemical vapor deposition (LPCVD) phosphorus-doped polysilicon as a conductor layer, were used as support to the sputtered TiN electrodes. When deposited directly on a highly conformal, pinhole free layer such as the LPCVD Poly-Si, porosity of PVD TiN is increased, comparing to when TiN is deposited on an underlying PVD layer [183], which is the case in the current Thesis work. TiN layers with high porosity yield higher charge injection capacity [172]. Additionally, LPCVD phosphorus-doped Poly-Si have a sheet resistance as low as 2 Ω/sq [184], providing lower resistivity interconnects when compared to the sputtered TiN in the present work (sheet resistance of 73.5 Ω/sq). Low pressure chemical vapor deposition uses, however, temperatures above 600 °C, which is the decomposition temperature of polyimide. Thus, a high-temperature process like LPCVD was not an option for the present microfabrication method.

In their study, Meijs *et al.* have used a titanium alloy (Ti-6Al-4V) rigid pin as an underlying layer for sputtering of TiN macroelectrodes with an area of 6 mm² [172]. A 10 μm thick TiN layer was deposited in two different stoichiometric conditions, yielding “smooth” and “porous” films, analyzed in both *in vitro* and *in vivo*. Voltammograms of both smooth and porous TiN electrodes showed a water window between -0.6 V and +1V, a rectangular shape (capacitive) profile, with no distinctive peaks in either of them. CIC of smooth TiN macroelectrodes in PBS was 24 ± 4 μC/cm², but no result was given in *in vivo* condition. In general, porous electrode layers yield electrically active areas larger than corresponding GSA, which in turn results into a larger charge injection capacity.

6 Conclusions

The work accomplished in the framework of this Thesis aimed at concept, design and develop of microelectrode arrays based on materials and processes that can be integrated as a back-end CMOS process. Important notions regarding the nature of stimulation and recording electrodes and their electrochemical properties, the mechanical properties of polyimides, theoretical models to predict 'allowed' mechanical deformations, and microfabrication techniques were given. Even if not original contributions, these analysis and discussions do revise some of the existing and critical knowledge for designing and manufacturing of flexible and implantable electrodes, thus providing solid grounds for the developments presented throughout.

In this work, polyimide-based, flexible, TiN electrodes were fabricated using a methodology that combines several microfabrication techniques and processes. In this approach, photolithography permitted the patterning of polyimide and metal films with reproducible feature precision, and the flexibility to easily and quickly change the electrode geometry, which can be important to change the electrode according to the anatomical requirements it must meet. Several iterative attempts have been required to achieve functional microelectrodes because of several hurdles. Etching of polyimide layers has been fine-tuned depending on whether the first or second layer were being etched. Metallization has also been optimized to achieve proper step coverage between bondpads on silicon dies and the electrode sites on polyimide.

Parallel to on-wafer microfabrication, a molding process has been developed that enables manufacturing of split-cylinder cuffs that target the rat vagus nerve. After microfabrication, polyimide electrodes were assembled onto the pre-molded cuffs. Mechanical assessment of split-cylinder cuff dummies was achieved *in vivo*.

Electrodes have been characterized by means of electrochemical methods. Charge injection capacity of microelectrodes is 154 μC/cm^2, i.e. 9.9 nC/phase. Macroelelectrodes have a lower charge injection capacity of 8.5 μC/cm^2, i.e. 13.6 nC/phase. Charge injection capacity, thus, decreases as the area increases. As these correlations between area and electrochemical measures were systematic across all measurements made, this is a basis to conclude that the microfabrication process is reproducible. Applications that require charge per phase of up to 10 nC per phase – as those allowed by current TiN microelectrodes – include intracortical microstimulation of the somatosensory cortex to restore hand tactile sensation (with 10 nC per phase with Utah microelectrodes) [38], and the use of cuff

electrodes for reconstructing electrical impedance tomography images of fascicular activation within the sciatic nerve and using charges of up to 5 nC per phase [40].

6.1 Future Work and Perspectives

The use of TiN as an electrode material, a widely used material in CMOS industries, plus the use of low temperature processes only (< 400 °C), makes the developed process compatible with the CMOS back-end process. While the current Thesis has confirmed that reliable interfaces between polyimide and silicon dies are possible, further work can now unfold on the silicon dies. A theoretical proposal that we have already put forward is to have an integrated radio-frequency (RF) circuitry for energy and communications, as well as an antenna, on the silicon die [185]. Having miniaturization in mind, the silicon dies with bond pads could include RF CMOS chip, with RF to DC converter, power control, voltage-controlled oscillator, and also non-RF structures like an antenna. The interconnection solution – silicon die to PCB – presented in this Thesis was adopted since it was required to have direct access to the electrodes for characterization, leading to a device with a size comparable to other electrode systems used in acute animal experiments [126-127]. However, the device can be significantly reduced in size if, instead of using the bulky connector attached to the PCB, the silicon die is used as a platform to enable the use of CMOS integration and/or packaging technologies. Since electrodes are routed and accessible on top of a silicon die, several technologies are available to integrate the developed electrode with electronics [186]. On a silicon wafer, self-assembling can be used to integrate multiple chips on a full wafer.

Also regarding miniaturization, in the current microelectrode array, the pitch between electrodes was set to 60 µm. By setting the pitch to 5 µm, a total of 24 electrodes could be patterned in a 2 mm long space, meaning an increment from the current 14 × 1 array to a 24 × 1 array, keeping the same electrode area. However, such increase in the overall number of electrodes would bring up new design challenges related to PCB dimensions, which again suggests the need for a wireless communication circuitry. In the present design, a 10 mm wide printed circuit board is enough to interface with 14 contacts. If more electrodes are to be used, judicious evaluation of the number of electrodes is required together with size constraints of the overall probe.

One important issue that must be addressed in future work, is the significant increases in impedance magnitude and changes of phase angle in 8 out of the 28 electrodes tested in EIS (please see Section 5.1). These changes, we believe, are associated with the cuff assembly process. Stress induced on the polyimide-based microelectrodes when maneuvering and gluing them onto the pre-molded PDMS led to

changes in the mechanical properties of the metal routings (electrodes and/or interconnects), ultimately leading to changes in the electrochemistry of those 8 electrode contacts. One possible solution to avoid damaging of contacts could be to use alternative methods for cuff forming, e.g. temperature tempering with metal rods [89] or in-situ suturing [49]. However, those methods present disadvantages in terms of handling, lacking dedicated handling structures as the current work proposes. The polyimide-based TiN microelectrodes presented in this work may as well be used as cortical arrays, i.e. without cuff assembly, thus preventing stress-induced undesired effects.

Another extremely important issue, likely the most important one, is related with the charge injection capacity of the sputtered TiN film. As mentioned in Subsection 3.2.4, sheet resistance of Ti-TiN film is 73.5 Ω/sq, whereas in other TiN films on rigid substrates that can be as low as 2 Ω/sq, as discussed in Subsection 5.3.3. Decreasing sheet resistance may be a relevant mean for increasing the amount of charge available at the interface. Thus, parameters such as the argon and nitrogen content in deposition plasma could be changed, thus achieving lowering the sheet resistance.

Appendix: Protocol for the Microfabrication of Polyimide-based TiN Electrodes

Next, the protocol or flowchart as followed in the last run at Else Kooi Laboratory (TU Delft) is presented below. For clarity some details have not been included.

1. Use single side polished silicon wafers, with following specifications:
    - n-type / p-type
    - resistivity: 2 – 5 Ωcm
    - thickness: 525 ± 15 µm
    - diameter: 100.0 ± 0.2 mm

    [FRONT SIDE PROCESSING]
2. Alignment marks.
    a. Coating 1.4 µm SPR3012 positive photoresist.
    b. 60s exposure with mask aligner.
    c. Development.
    d. Plasma etching.
    e. Check in microscope if marks are visible. Strip photoresist in pure oxygen plasma.
    f. Cleaning. 10 minutes HNO_3 99% at room temperature, rinse, 10 minutes HNO_3 69% at 110 °C, rinse, dry.
3. Deposit PECVD 1 µm silicone dioxide (SiO_2). Figure A.1 A.

    [BACK SIDE PROCESSING]
4. Deposit PECVD 6 µm silicone dioxide (SiO_2). Figure A.1 A.
5. Coating 3 µm SPR3012 positive photoresist. 60s exposure. Develop.
    a. Use mask #1 (Figure 3.6)
6. SiO2 etching with plasma containing CF4 (50 sccm), CHF3 (25 sccm) and He (40 sccm). Etch rate approx.. 500 nm/min, so the 6 µm took 12 minutes.
    Figure A.1 B.
7. Strip photoresist and clean as in 2f)

Figure A.1 Substrate (silicon wafer in white) with SiO_2 layers (green) deposited on the front and back sides (TOP). (B) Patterning of back side SiO_2 layer with mask #1. Layers thicknesses are not at scale.

[FRONT SIDE PROCESSING]

8. Polyimide coating. Manual wafer coater and hot plate.
    a. Dispense VM652 primer over substrate. 10s @ 500rpm + 45s @ 3500 rpm.
    b. Dispense 3 mL of HD microsystems polyimide 2611. 15s @ 350rpm + 45s @ 1000 rpm + 2s @ 4000 rpm to decrease thickness at the edges.
    c. Soft bake 6 min @ 120 °C in hot plate.
9. Polyimide curing. Low pressure oven.
    a. 200 mbar N_2 atmosphere.
    b. 2h @ 400 °C.
    c. Cooling overnight.
10. Cleaning after curing.
    a. Acetone + isopropanol + rinsing DI water
11. Measure polyimide thickness with profilometer. Should be 9-10 µm. Figure A.2.

Figure A.2 Front side 9-10 µm thick polyimide layer (yellow) after curing and before patterning.

12. Deposit 200 nm PECVD TEOS. To be used as hard mask for polyimide etching.

13. Coating 2 µm SPR 3017M photoresist. 60s exposure. Develop.
    a. Use mask #2 (Figure 3.6)
14. Etch PECVD TEOS using same chemistry as 6)
15. Polyimide etching with two-step approach.
    a. First, pure oxygen plasma to etch initial 6 µm. Etch rate is variable between 2 and 5 µm/min, depending on temperature (time).
    b. Second, etching is concluded in SPTS Omega ICP etcher with a plasma containing 80% of O_2, 13% of N_2 and 7% of CF_4 in order to minimize silicon residues.
    c. PECVD TEOS is removed using buffered hydrofluoric acid (BHF) 7:1.
    d. Figure A.3.

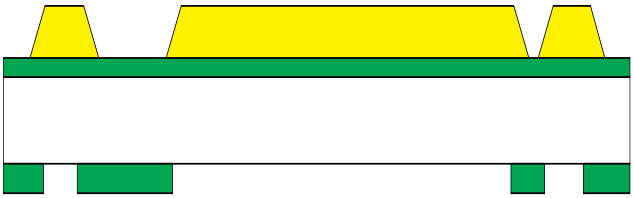

Figure A.3 Front side polyimide layer after patterning.

16. Sputter metal stack in SPTS Sigma PVD.
    a. 40 nm Ti + 200 nm TiN + 2.5 µm Al
    b. Deposition temperature: 300 °C
    c. No breaking of vaccuum
    d. Figure A.3.
17. Coating 1.4 µm SPR 3012 photoresist. 10s exposure. Develop.
    a. Use mask #3 for aluminum pads and step coverage (Figure 3.6)
18. Etching 2.5 µm aluminum layer, to define bond pads and aluminum coverage on silicon-polyimide transition.
    a. Dry etching until 250-300 nm thick in SPTS Omega ICP etcher (30 sccm Cl_2, 40 sccm HBr – hydrogen bromine).
    b. Rinse 1 min in Triton X-100 surfactant.
    c. Wet etching in PES-type (phosphoric-acetic-nitric acid solution).
       Etch rate: 150 nm/min.
    d. This approach minimizes etching time, while safeguarding TiN surface from being etched in the dry etching chemistry.

19. Sputter aluminum layer (100 nm thick) at room temperature.
    a. This layer is used for protection of TiN surface in subsequent steps like dry etching of the second polyimide layer.
    b. Titanium, TiN and the 100 nm thick aluminum are then patterned using mask #4
20. Stripping of photoresist with NMP solution @ 70 °C for 10 min.
    a. Use of this wet etchant is preferable over dry etching of resist, in order to protect the polyimide layer.
21. Measurement of aluminum thickness with profilometer.
22. Coating 2 µm SPR3012 photoresist. Expose 60s. Develop.
    a. Use mask #4 to pattern Ti-TiN interconnects and electrode contacts (Figure 3.6)
23. Dry etching of Ti-TiN double layer in SPTS Omega ICP etcher (30 sccm Cl_2, 40 sccm HBr – hydrogen bromine).
    a. Figure A.4
24. Stripping of photoresist with NMP solution @ 70 °C for 10 min.

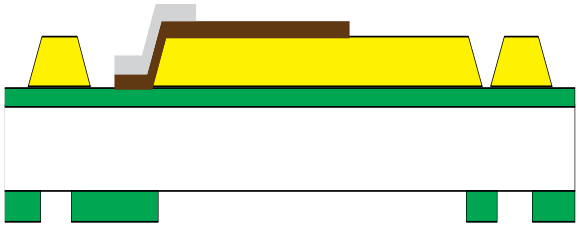

Figure A.4 Front side polyimide layer after sputtering of metal stack layer (40 nm titanium, 200 titanium nitride, 2.5 µm aluminum), and subsequent patterning of aluminum for bond pads and step coverage between silicone dies and polyimide.

25. 2nd layer Polyimide coating. Manual wafer coater and hot plate.
    a. Dispense VM652 primer over substrate. 10s @ 500rpm + 45s @ 3500 rpm.
    b. Dispense 3 mL of HD microsystems polyimide 2611. 15s @ 350rpm + 45s @ 1000 rpm + 2s @ 4000 rpm to decrease thickness at the edges.
    c. Soft bake 6 min @ 120 °C in hot plate.
26. Polyimide curing. Low pressure oven.
    a. 200 mbar N_2 atmosphere.
    b. 2h @ 400 °C.
    c. Cooling overnight.

27. Cleaning after curing.
    a. Acetone + isopropanol + rinsing DI water
28. Measure thickness of 2nd polyimide layer with profilometer. Should be 9-10 µm.
29. Deposit 200 nm PECVD TEOS. To be used as hard mask for etching of 2nd polyimide layer.
30. Coating 2 µm SPR 3017M photoresist. 60s exposure. Develop.
    a. Use mask #4 (Figure 3.6)
31. Etch PECVD TEOS using same chemistry as 6)
    a. Figure A.5.

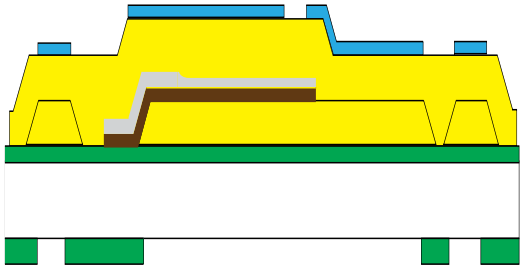

Figure A.5 After curing of 2nd polyimide layer, deposition and patterning of 200 nm PECVD TEOS, to be used as hard mask (blue) for patterning of interconnects and electrode contacts.

32. All 2nd polyimide layer is etched in SPTS Omega ICP etcher with a plasma containing 80% of O_2, 13% of N_2 and 7% of CF_4 in order to minimize silicon residues. This is pure anisotropic etching.
    a. Etch rates: PI: ~900 nm/min, SiO_2: 50nm/min, TiN: ~15nm/min
33. Etch PECVD TEOS that is left using the same chemistry as 6)

[BACK SIDE PROCESSING]

34. Deep reactive ion etching (DRIE) of bulk silicon wafer until stop layer. 1h30m @ 20 °C.
    a. Figure A.6.

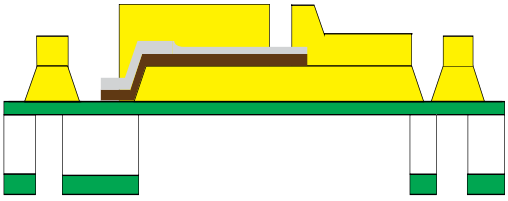

Figure A.6 After anisotropic etching of 2nd polyimide layer, and back side etching of bulk silicon wafer.

35. Etching of the 1 µm SiO_2 stop layer. Using same chemistry as in 6)
36. Etching of the protective, 100 nm thick aluminum layer on top of TiN contacts
    a. Use a timed wet etching step in same PES-type etchant (selective to TiN).

37. Devices are ready to be detached from the wafer by cutting of polyimide tabs, as seen below:

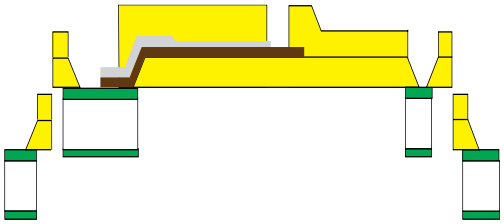

Figure A.7 Polyimide-based TiN electrodes after being detached from the carrier silicon wafer by cutting of polyimide tabs.

Bibliography

[1] [Online], "90/385/EEC," 1990.
Available: https://eur-lex.europa.eu/LexUriServ/LexUriServ.do?uri=CELEX:31990L0385:en:HTML.
[Accessed: 11-Jun-2020].

[2] [Online], "A Lifesaver in a Plastic Cup: A history of pacemakers at Siemens". Available: https://www.medmuseum.siemens-healthineers.com/en/stories-from-the-museum/herzschrittmacher
[Accessed: 11-Jun-2020].

[3] J. A. Hoerni, "Method of Manufacturing Semiconductor Devices," Google Patents, March 1962.

[4] B. Larsson, H. Elmqvist, L. Rydén, and H. Schüller, "Lessons from the first patient with an implanted pacemaker: 1958-2001," Pacing Clin. Electrophysiol., vol. 26, no. January, pp. 114–124, 2003.

[5] M. J. P. Raatikainen, D. O. Arnar, B. Merkely, A. J. Camm, and G. Hindricks, "Access to and clinical use of cardiac implantable electronic devices and interventional electrophysiological procedures in the European Society of Cardiology Countries: 2016 Report from the European Heart Rhythm Association," Europace, vol. 18, no. suppl 3, pp. iii1–iii79, 2016.

[6] B. C. Papsin and K. A. Gordon, "Cochlear Implants for Children with Severe-to-Profound Hearing Loss," N. Engl. J. Med., vol. 357, pp. 2380–7, 2007.

[7] J. O. Mills, A. Jalil, and P. E. Stanga, "Electronic retinal implants and artificial vision: journey and present," Eye, vol. 31, no. 10, pp. 1383–1398, 2017.

[8] N. Pouratian, Thakkar, Sandeep, Kim, Won, and J. Bronstein, "Deep brain stimulation for the treatment of Parkinson's disease: efficacy and safety," Degener. Neurol. Neuromuscul. Dis., vol. 2, pp. 1–16, 2012.

[9] J. S. Grider et al., "Effectiveness of Spinal Cord Stimulation in Chronic Spinal Pain: A Systematic Review.," Pain Physician, vol. 19, no. 1, pp. E33–E54, 2016.

[10] C. M. Degiorgio et al., "Prospective Long-Term Study of Vagus Nerve Stimulation for the Treatment of Refractory Seizures," Epilepsia, vol. 41, no. 9, pp. 1195–1200, 2000.

[11] S. T. Aaronson et al., "A 5-year observational study of patients with treatment-resistant depression treated with vagus nerve stimulation or treatment as usual: Comparison of response, remission, and suicidality," Am. J. Psychiatry, vol. 174, no. 7, pp. 640–648, 2017.

[12] [Online] "MED-EL Medical Electronics".
Available: https://www.medel.com/hearing-solutions/cochlear-implants/synchrony
[Accessed: 11-Jun-2020].

[13] J. Dorn, A. Ahuja, A. Caspi, and et al, "The Detection of Motion by Blind Subjects With the Epiretinal 60-Electrode (Argus II) Retinal Prosthesis," JAMA Ophthalmol., vol. 131, no. 2, pp. 183–189, 2013.

[14] [Online] "Argus Retinal implant".
Available: https://secondsight.com/discover-argus/
[Accessed: 11-Jun-2020].

[15] [Online] "ACTIVA Deep Brain Stimulator".

Available: https://www.medtronic.com/us-en/healthcare-professionals/therapies-procedures/neurological/deep-brain-stimulation.html
[Accessed: 11-Jun-2020].

[16] [Online] "Deep Brain Stimulation.".
Available: thebrainstimulator.net/brain-stimulation-comparison/attachment/dbs-deep-brain-stimulation/. [Accessed: 11-Jun-2020].

[17] [Online] "Grand View Research - Neuroprosthetics".
Available: www.grandviewresearch.com/press-release/global-neuroprosthetics-market.
[Accessed: 11-Jun-2020].

[18] A. Demosthenous, "Advances in Microelectronics for Implantable Medical Devices," Adv. Electron., vol. Article ID, pp. 1–21, 2014.

[19] Ng, Kian Ann, Greenwald, Elliot, Xu, Yong Ping, and N. Thakor, "Implantable neurotechnologies: a review of integrated circuit neural amplifiers," Med. Biol. Eng. Comput., vol. 54, no. 1, pp. 1–37, 2016.

[20] Y.-H. Joung, "Development of Implantable Medical Devices: From an Engineering Perspective," Int. Neurourol. J., vol. 17, no. 3, pp. 98–106, 2013.

[21] J. Choi, S.-P. Kim, J. Sohn, S.-M. Kim, and R.-H. Ryu, "Implantable Neural Probes for Brain-Machine Interfaces – Current Developments and Future Prospects," Exp. Neurobiol., vol. 27, no. 6, p. 453, 2019.

[22] M. A. Schiefer, K. H. Polasek, R. J. Triolo, G. C. J. Pinault, and D. J. Tyler, "Selective stimulation of the human femoral nerve with a flat interface nerve electrode," J. Neural Eng., vol. 7, no. 2, pp. 1–19, 2010.

[23] M. A. Schiefer et al., "Selective Activation of the Human Tibial and Common Peroneal Nerves with a Flat Interface Nerve Electrode," J. Neural Eng., vol. 10, no. 5, pp. 1–26, 2013.

[24] C. Veraart, W. M. Grill, and J. T. Mortimer, "Selective control of muscle activation with a multipolar nerve cuff electrode," IEEE Trans. Biomed. Eng., vol. 40, no. 7, pp. 640–653, Jul. 1993.

[25] M. D. Tarler and J. T. Mortimer, "Selective and independent activation of four motor fascicles using a four contact nerve-cuff electrode," IEEE Trans. neural Syst. Rehabil. Eng., vol. 12, no. 2, pp. 251–7, Jun. 2004.

[26] K. H. Polasek, H. a Hoyen, M. W. Keith, R. F. Kirsch, and D. J. Tyler, "Stimulation stability and selectivity of chronically implanted multicontact nerve cuff electrodes in the human upper extremity," IEEE Trans. Neural Syst. Rehabil. Eng., vol. 17, no. 5, pp. 428–37, Oct. 2009.

[27] B. P. Christie et al., "Long-term stability of stimulating spiral nerve cuff electrodes on human peripheral nerves," J. Neuroeng. Rehabil., vol. 14, no. 1, pp. 14–70, 2017.

[28] A. Branner, R. B. Stein, and R. A. Normann, "Selective Stimulation of Cat Sciatic Nerve Using an Array of Varying-Length Microelectrodes," J. Neurophysiol., vol. 85, no. 4, pp. 1585–1594, 2001.

[29] H. a C. Wark et al., "A new high-density (25 electrodes/mm^2) penetrating microelectrode array for recording and stimulating sub-millimeter neuroanatomical structures," J. Neural Eng., vol. 10, pp. 1–10, Aug. 2013.

[30] T. Boretius et al., "A transverse intrafascicular multichannel electrode (TIME) to interface with the peripheral nerve," Biosens. Bioelectron., vol. 26, no. 1, pp. 62–9, Sep. 2010.

[31] J. Badia, T. Boretius, E. Udina, T. Stieglitz, and X. Navarro, "Biocompatibility of Chronically Implanted Transverse Intrafascicular Multichannel Electrode (Time) in the Rat Sciatic Nerve," IEEE Trans. Biomed. Eng., vol. 58, no. 8, pp.

2324–2332, May 2011.

[32] G. Di Pino et al., “Intraneural stimulation elicits discrimination of textural features by artificial fingertip in intact and amputee humans,” Elife, vol. 5, pp. 1–27, 2016.

[33] C. Xie, J. Liu, T. M. Fu, X. Dai, W. Zhou, and C. M. Lieber, “Three-dimensional macroporous nanoelectronic networks as minimally invasive brain probes,” Nat. Mater., vol. 14, no. 12, pp. 1286–1292, 2015.

[34] J. J. Jun et al., “Fully Integrated Silicon Probes for High-Density Recording of Neural Activity,” Nature, vol. in press, no. 7679, pp. 232–236, 2017.

[35] K. J. Gustafson, G. C. J. Pinault, J. J. Neville, J. A. D. Jr, J. Jean-claude, and R. J. Triolo, “Fascicular anatomy of human femoral nerve: implications for neural prostheses using nerve cuff electrodes,” Rehabil. Res. Dev., vol. 46, no. 7, pp. 973–984, 2009.

[36] K. J. Gustafson, Y. Grinberg, S. Joseph, and R. J. Triolo, “Human distal sciatic nerve fascicular anatomy: Implications for ankle control using nerve-cuff electrodes,” J. Rehabil. Res. Dev., vol. 49, no. 2, p. 309, 2012.

[37] M. W. Merlo, R. L. Snyder, and M. Bachman, “Microelectrode arrays fabricated using a novel hybrid microfabrication,” Biomed. Microdevices, vol. 14, no. 1, pp. 193–205, 2013.

[38] S. N. Flesher et al., “Intracortical microstimulation of human somatosensory cortex,” Sci. Transl. Med., vol. 8, no. 361ra141, pp. 1–11, 2016.

[39] C. K. Overstreet, V. J. Santos, S. I. Helms Tillery, R. D. Ponce Wong, and R. B. Hellman, “Discriminability of Single and Multichannel Intracortical Microstimulation within Somatosensory Cortex,” Front. Bioeng. Biotechnol., vol. 4, no. December, pp. 1–10, 2016.

[40] K. Aristovich et al., “Imaging fast neural traffic at fascicular level with electrical impedance tomography: Proof of principle in rat sciatic nerve,” J. Neural Eng., vol. 15, no. 056025, 2018.

[41] S. Behkami, J. Frounchi, F. Ghaderi Pakdel, and T. Stieglitz, “Simulation of effects of the electrode structure and material in the density measuring system of the peripheral nerve based on micro-electrical impedance tomography,” Biomed. Eng. (NY)., vol. 63, no. 2, pp. 151–161, 2018.

[42] W. D. Memberg et al., “Implanted neuroprosthesis for restoring arm and hand function in people with high level tetraplegia,” Arch. Phys. Med. Rehabil., vol. 95, no. 6, pp. 1201–1211, Jun. 2014.

[43] C. Hassler, T. Boretius, and T. Stieglitz, “Polymers for Neural Implants,” J. Polym. Sci., vol. 49, pp. 18–33, 2011.

[44] A. Weltman, J. Yoo, and E. Meng, “Flexible, penetrating brain probes enabled by advances in polymer microfabrication,” Micromachines, vol. 7, no. 10, 2016.

[45] Joseph J Pancrazio et al., “Thinking Small – Progress on Microscale Neurostimulation Technology,” Neuromodulation, vol. 20, no. 8, pp. 745–752, 2017.

[46] H. Yu, W. Xiong, H. Zhang, W. Wang, and Z. Li, “A Parylene Self-Locking Cuff Electrode for Peripheral Nerve Stimulation and Recording,” J. Microelectromechanical Syst., vol. 23, no. 5, pp. 1025–1035, Oct. 2014.

[47] S. Elyahoodayan, C. Larson, A. M. Cobo, E. Meng, and D. Song, “Acute in vivo testing of a polymer cuff electrode with integrated microfluidic channels for stimulation, recording, and drug delivery on rat sciatic nerve,” J. Neurosci. Methods, vol. 336, p. 108634, 2020.

[48] F. Decataldo et al., “Stretchable Low Impedance Electrodes for Bioelectronic Recording from Small Peripheral Nerves,” Sci. Rep., vol. 9, p. 10598, 2019.

[49] M. A. González-González et al., “Thin Film Multi-Electrode Softening Cuffs for Selective Neuromodulation,” Sci. Rep., vol. 8, no. 1, pp. 1–15, 2018.

[50] Y. Lu, H. Lyu, A. G. Richardson, T. H. Lucas, and D. Kuzum, “Flexible Neural Electrode Array Based-on Porous Graphene for Cortical Microstimulation and Sensing,” Sci. Rep., vol. 6, no. May, pp. 1–9, 2016.

[51] M. Parmeggiani et al., “PDMS/Polyimide Composite as an Elastomeric Substrate for Multifunctional Laser-Induced Graphene Electrodes,” ACS Appl. Mater. Interfaces, vol. 11, pp. 33221–33230, 2019.

[52] M. David-Pur, L. Bareket-Keren, G. Beit-Yaakov, D. Raz-Prag, and Y. Hanein, “All-carbon-nanotube flexible multi-electrode array for neuronal recording and stimulation.,” Biomed. Microdevices, vol. 16, no. 1, pp. 43–53, Feb. 2014.

[53] B. Ji et al., “Flexible polyimide-based hybrid opto-electric neural interface with 16 channels of micro-LEDs and electrodes,” Microsystems Nanoeng., vol. 4, no. 27, pp. 1–11, 2018.

[54] J. Jeong, S. H. Bae, K. S. Min, J. M. Seo, H. Chung, and S. J. Kim, “A miniaturized, eye-conformable, and long-term reliable retinal prosthesis using monolithic fabrication of liquid crystal polymer (LCP),” IEEE Trans. Biomed. Eng., vol. 62, no. 3, pp. 982–989, 2015.

[55] D. Kang, A. Standley, J. H. C. Chang, Y. Liu, and Y. C. Tai, “Effects of deposition temperature on Parylene-C properties,” in Proceedings of the IEEE International Conference on Micro Electro Mechanical Systems (MEMS), 2013, pp. 389–392.

[56] D. P. Nair, N. B. Cramer, T. F. Scott, C. N. Bowman, and R. Shandas, “Photopolymerized Thiol-Ene Systems as Shape Memory Polymers,” Polymer (Guildf)., vol. 51, no. 19, pp. 4383–4389, 2010.

[57] S. Gupta, W. T. Navaraj, L. Lorenzelli, and R. Dahiya, “Ultra-thin chips for high-performance flexible electronics,” Nat. Partn. J. Flex. Electron., vol. 2, no. 1, 2018.

[58] T. Stieglitz, H. Beutel, M. Schuettler, and J. Meyer, “Micromachined , Polyimide-Based Devices for Flexible Neural Interfaces,” Biomed. Microdevices, vol. 2:4, pp. 283–294, 2000.

[59] H. Beutel, T. Stieglitz, J.-U. Meyer, O. Scholz, and W. Haberer, “High density interconnects and flexible hybrid assemblies for active biomedical implants,” IEEE Trans. Adv. Packag., vol. 24, no. 3, pp. 366–374, 2001.

[60] S. Myllymaa et al., “Fabrication and testing of polyimide-based microelectrode arrays for cortical mapping of evoked potentials,” Biosens. Bioelectron., vol. 24, no. 10, pp. 3067–3072, 2009.

[61] E. Tolstosheeva et al., “A multi-channel, flex-rigid ECoG microelectrode array for visual cortical interfacing,” Sensors, vol. 15, pp. 832–854, 2015.

[62] J. Laconte, D. Flandre, and J. P. Raskin, Micromachined Thin-Film Sensors for SOI-CMOS Co-Integration. Springer, 2006.

[63] D. H. Baek et al., “Interconnection of multichannel polyimide electrodes using anisotropic conductive films (ACFs) for biomedical applications,” IEEE Trans. Biomed. Eng., vol. 58, no. 5, pp. 1466–1473, 2011.

[64] S. Kisban et al., “Microprobe array with low impedance electrodes and highly flexible polyimide cables for acute neural recording.,” in Proceedings of the 29th Annual Internation Conference of the IEEE EMBS, 2007, vol. 2007, pp. 175–8.

[65] A. Schander et al., “Design and fabrication of novel multi-channel floating neural probes for intracortical chronic recording,” Sensors Actuators, A Phys., vol. 247, pp. 125–135, 2016.

[66] T. Stieglitz, M. Schuettler, and K. P. Koch, “Implantable biomedical microsystems for neural prostheses,” IEEE Eng.

Med. Biol. Mag., vol. 24, no. 5, pp. 58–65, 2005.

[67] R. Melzack and P. D. Wall, "Pain Mechanisms: A New Theory," Science (80-.)., vol. 150, no. 3699, pp. 971–979, 1965.

[68] W. Sweet and P. Wall, "Temporary Abolition of Pain in Man," Science (80-.)., vol. 155, no. 3758, pp. 109–109, 1967.

[69] [Online] "The Academy of 21st Century Learning: Electrical Stimulation of Frog Legs" Available: https://www.youtube.com/watch?v=sJifWqUa2pY. [Accessed: 11-Jun-2020].

[70] C. J. Schwiening, "A brief historical perspective: Hodgkin and Huxley," J. Physiol., vol. 590, no. 11, pp. 2571–2575, 2012.

[71] A. L. Hodgkin and A. F. Huxley, "A Quantitative Description of Membrane Current and its Application to Conduction and Excitation in Nerve," J. Physyology, vol. 117, pp. 500–544, 1952.

[72] K. S. Saladin, C. A. Gan, and H. N. Cushman, Anatomy & Physiology: The Unity of Form and Function, 8th editio. New York: McGraw-Hill, 2018.

[73] N. R. Hagfors, "Implantable Electrode," Google Patents, 1972.

[74] R. E. Avery and J. S. Wepsic, "Implantable Electrodes for the Stimulation of the Sciatic Nerve," 3738368, 1973.

[75] G. Naples, J. Sweeney, and J. Mortimer, "Implantable cuff, method of manufacture, and method of installation," 1986.

[76] G. Naples, J. Mortimer, A. Scheiner, and J. Sweeney, "A spiral nerve cuff electrode for peripheral nerve stimulation," IEEE Trans. Biomed. Eng., vol. 35, no. 8823295, pp. 905–916, 1988.

[77] W. L. Rutten, H. J. van Wier, and J. H. Put, "Sensitivity and Selectivity of Intraneural Stimulation Using a Silicon Electrode Array.," IEEE Trans. Biomed. Eng., vol. 38, no. 2, pp. 192–198, Feb. 1991.

[78] G. T. A. Kovacs, C. W. Storment, and J. M. Rosen, "Regeneration Microelectrode Array for Peripheral Nerve Recording and Stimulation," IEEE Trans. Biomed. Eng., vol. 39, no. 9, pp. 893–902, 1992.

[79] W. M. Grill, G. H. Creasey, D. A. Ksienski, C. S. Veraart, and J. T. Mortimer, "Thin film implantable electrode and method of manufacture," WO 93/20887.

[80] X. Navarro, T. B. Krueger, N. Lago, S. Micera, T. Stieglitz, and P. Dario, "A critical review of interfaces with the peripheral nervous systemfor the control of neuroprostheses and hybrid bionic systems," J. Peripher. Nerv. Syst., vol. 10, no. 3, pp. 229–58, Sep. 2005.

[81] W. M. Grill, S. E. Norman, and R. V Bellamkonda, "Implanted neural interfaces: biochallenges and engineered solutions," Annu. Rev. Biomed. Eng., vol. 11, pp. 1–24, Jan. 2009.

[82] C. J. Bettinger, "Recent advances in materials and flexible electronics for peripheral nerve interfaces," Bioelectron. Med., vol. 4, no. 1, pp. 1–10, 2018.

[83] S. Micera and X. Navarro, "Bidirectional Interfaces with the Peripheral Nervous System," Int. Rev. Neurobiol., vol. 86, no. 09, pp. 23–38, 2009.

[84] S. Micera et al., "On the use of longitudinal intrafascicular peripheral interfaces for the control of cybernetic hand prostheses in amputees.," IEEE Trans. Neural Syst. Rehabil. Eng., vol. 16, no. 5, pp. 453–72, Oct. 2008.

[85] A. B. Schwartz, "Cortical Neural Prosthetics," Annu. Rev. Neurosci., vol. 27, no. 1, pp. 487–507, 2004.

[86] D. Prodanov and J. Delbeke, "Mechanical and biological interactions of implants with the brain and their impact on implant design," Front. Neurosci., vol. 10, no. FEB, 2016.

[87] C. T. Nordhausen, E. M. Maynard, and R. a. Normann, "Single unit recording capabilities of a 100 microelectrode array," Brain Res., vol. 726, pp. 129–140, 1996.

[88] T. Stieglitz, H. Beutel, and J.-U. Meyer, "A flexible, light-weight multichannel sieve electrode with integrated cables for interfacing regenerating peripheral nerves," Sensors Actuators A Phys., vol. 60, no. 1–3, pp. 240–243, May 1997.

[89] F. J. Rodríguez et al., "Polyimide cuff electrodes for peripheral nerve stimulation," J. Neurosci. Methods, vol. 98, pp. 105–118, 2000.

[90] A. Branner and R. A. Normann, "A multielectrode array for intrafascicular recording and stimulation in sciatic nerve of cats," Brain Res. Bull., vol. 51, no. 4, pp. 293–306, Mar. 2000.

[91] S. Negi and et al, "Neural Electrode Degradation from Continuous Electrical Stimulation: Comparison of Sputtered and Activated Iridium Oxide," J. Neurosci. Methods, vol. 186, no. 1, pp. 220–231, 2010.

[92] [Online] "Utah array".
Available: https://blackrockmicro.com/electrode-types/utah-array/
[Accessed: 11-Jun-2020].

[93] T. S. Davis et al., "Restoring motor control and sensory feedback in people with upper extremity amputations using arrays of 96 microelectrodes implanted in the median and ulnar nerves," J. Neural Eng., vol. 13, no. 3, p. 36001, 2016.

[94] B. J. Black et al., "Chronic recording and electrochemical performance of Utah microelectrode arrays implanted in rat motor cortex," J. Neurophysiol., vol. 120, no. 4, pp. 2083–2090, 2018.

[95] N. Nannini and K. Horch, "Muscle recruitment with intrafascicular electrodes," IEEE Trans. Biomed. Eng., vol. 38, no. 8, pp. 769–776, 1991.

[96] T. Lefurge, E. Goodall, K. Horch, L. Stensaas, and A. Schoenberg, "Chronically implanted intrafascicular recording electrodes.," Ann. Biomed. Eng., vol. 19, no. 12, pp. 197–207, 1991.

[97] J. A. Malmstrom, T. G. McNaughton, and K. W. Horch, "Recording properties and biocompatibility of chronically implanted polymer-based intrafascicular electrodes.," Ann. Biomed. Eng., vol. 26, pp. 1055–1064, 1998.

[98] S. M. Lawrence, G. S. Dhillon, and K. W. Horch, "Fabrication and characteristics of an implantable, polymer-based, intrafascicular electrode," J. Neurosci. Methods, vol. 131, no. 1–2, pp. 9–26, Dec. 2003.

[99] N. Lago, K. Yoshida, K. P. Koch, and X. Navarro, "Assessment of Biocompatibility of Chronically Implanted Polyimide and Platinum Intrafascicular Electrodes," IEEE Trans. Biomed. Eng., vol. 54, no. 2, pp. 281–290, 2007.

[100] A. Kundu, K. R. Harreby, K. Yoshida, T. Boretius, T. Stieglitz, and W. Jensen, "Stimulation selectivity of the 'thin-film longitudinal intrafascicular electrode' (tfLIFE) and the 'transverse intrafascicular multi-channel electrode' (TIME) in the large nerve animal model," IEEE Trans. Neural Syst. Rehabil. Eng., vol. 22, no. 2, pp. 400–10, Mar. 2014.

[101] P. M. Rossini et al., "Double nerve intraneural interface implant on a human amputee for robotic hand control," Clin. Neurophysiol., vol. 121, no. 5, pp. 777–783, 2010.

[102] A. Benvenuto et al., "Intrafascicular thin-film multichannel electrodes for sensory feedback: Evidences on a human amputee," 2010 Annu. Int. Conf. IEEE Eng. Med. Biol. Soc. EMBC'10, pp. 1800–1803, 2010.

[103] E. Fernandez et al., "Restoring Natural Sensory Feedback in Real-Time Bidirectional Hand Prostheses," Sci. Transl.

Med., vol. 6, no. 222, pp. 222ra19-222ra19, 2014.

[104] T. Boretius et al., "A transverse intrafascicular multichannel electrode (TIME) to treat phantom limb pain — Towards human clinical trials," 2012 4th IEEE RAS EMBS Int. Conf. Biomed. Robot. Biomechatronics, pp. 282–287, Jun. 2012.

[105] M. Mueller, N. De La Oliva, J. Del Valle, I. Delgado-Martinez, X. Navarro, and T. Stieglitz, "Rapid prototyping of flexible intrafascicular electrode arrays by picosecond laser structuring," J. Neural Eng., vol. 14, no. 6, 2017.

[106] C. Boehler, T. Stieglitz, and M. Asplund, "Nanostructured platinum grass enables superior impedance reduction for neural microelectrodes," Biomaterials, vol. 67, pp. 346–353, 2015.

[107] R. M. Bradley, R. H. Smoke, T. Akin, and K. Najafi, "Functional regeneration of glossopharyngeal nerve through micromachined sieve electrode arrays," Brain Res., vol. 594, no. 1, pp. 84–90, 1992.

[108] T. Stieglitz, H. Ruf, M. Gross, M. Schuettler, and J. U. Meyer, "A biohybrid system to interface peripheral nerves after traumatic lesions: Design of a high channel sieve electrode," Biosens. Bioelectron., vol. 17, no. 8, pp. 685–696, 2002.

[109] A. Ramachandran et al., "Design, in vitro and in vivo assessment of a multi-channel sieve electrode with integrated multiplexer," J. Neural Eng., vol. 3, no. 2, pp. 114–124, 2006.

[110] S. P. Lacour, R. Atta, J. J. FitzGerald, M. Blamire, E. Tarte, and J. Fawcett, "Polyimide micro-channel arrays for peripheral nerve regenerative implants," Sensors Actuators, A Phys., vol. 147, no. 2, pp. 456–463, 2008.

[111] J. J. FitzGerald, S. P. Lacour, S. B. McMahon, and J. W. Fawcett, "Microchannel electrodes for recording and stimulation: In vitro evaluation," IEEE Trans. Biomed. Eng., vol. 56, no. 5, pp. 1524–1534, 2009.

[112] A. Ajam and R. Hossain, "Handcrafted Microwire Regenerative Peripheral Nerve Interfaces with Wireless Neural Recording and Stimulation Capabilities," Int. J. Sens. Networks Data Commun., vol. 05, no. 01, pp. 1–5, 2016.

[113] Srivinasan, Akhil et al., "Microchannel-based regenerative scaffold for chronic peripheral nerve interfacing in amputees," Bioma, vol. 41, pp. 151–165, 2015.

[114] P. F. Johnson, J. J. Bernstein, G. Hunter, W. W. Dawson, and L. L. Hench, "An in vitro and in vivo analysis of anodized tantalum capacitive electrodes: Corrosion response, physiology, and histology," J. Biomed. Mater. Res., vol. 11, no. 5, pp. 637–656, 1977.

[115] W. F. Agnew and D. B. McCreery, "Considerations for safety with chronically implanted nerve electrodes.," Epilepsia, vol. 31 Suppl 2, pp. S27–S32, 1990.

[116] D. Tyler and D. Durand, "Functionally selective peripheral nerve stimulation with a flat interface nerve electrode," IEEE Trans. Neural Syst. Rehabil. Eng., vol. 10, no. 4, pp. 294–303, 2002.

[117] P. B. Yoo and D. M. Durand, "Selective recording of the canine hypoglossal nerve using a multicontact flat interface nerve electrode," IEEE Trans. Biomed. Eng., vol. 52, no. 8, pp. 1461–1469, 2005.

[118] D. W. Tan, M. A. Schiefer, M. W. Keith, J. R. Anderson, J. Tyler, and D. J. Tyler, "A neural interface provides long-term stable natural touch perception," Sci. Transl. Med., vol. 6, no. 257, pp. 1–25, 2014.

[119] M. J. Freeberg, M. A. Stone, R. J. Triolo, and D. J. Tyler, "The design of and chronic tissue response to a composite nerve electrode with patterned stiffness," J. Neural Eng., vol. 14, no. 3, p. 036022, 2017.

[120] F. A. Cuoco and D. M. Durand, "Measurement of External Pressures Generated by Nerve Cuff Electrodes," IEEE Trans. Rehabil. Eng., vol. 8, no. 1, pp. 35–41, 2000.

[121] J. D. Sweeney, D. A. Ksienski, and J. T. Mortimer, "A Nerve Cuff Technique for Selective Excitation of Peripheral Nerve Trunk Regions," IEEE Trans. Biomed. Eng., vol. 37, no. 7, pp. 706–715, 1990.

[122] J. Hausmann et al., "Functional electrical stimulation through direct 4-channel nerve stimulation to improve gait in multiple sclerosis: a feasibility study," J. Neuroeng. Rehabil., vol. 12, no. 1, pp. 1–9, 2015.

[123] K. H. Polasek, S. Member, H. A. Hoyen, M. W. Keith, and D. J. Tyler, "Human Nerve Stimulation Thresholds and Selectivity Using a Multi-contact Nerve Cuff Electrode," IEEE Trans. Neural Syst. Rehabil. Eng., vol. 15, no. 1, pp. 76–82, 2007.

[124] D. T. T. Plachta et al., "Blood pressure control with selective vagal nerve stimulation and minimal side effects," J. Neural Eng., vol. 11, no. 3, pp. 1–15, Jun. 2014.

[125] N. S. Korivi and P. K. Ajmera, "Clip-on micro-cuff electrode for neural stimulation and recording," Sensors Actuators B Chem., vol. 160, no. 1, pp. 1514–1519, Dec. 2011.

[126] X. Kang, J.-Q. Liu, H. Tian, B. Yang, Y. Nuli, and C. Yang, "Self-Closed Parylene Cuff Electrode for Peripheral Nerve Recording," J. Microelectromechanical Syst., vol. 24, no. 2, pp. 319–332, Apr. 2015.

[127] Y. J. Lee, H. J. Kim, S. H. Do, J. Y. Kang, and S. H. Lee, "Characterization of nerve-cuff electrode interface for biocompatible and chronic stimulating application," Sensors Actuators, B Chem., vol. 237, pp. 924–934, 2016.

[128] G. G. Stoney, "The Tension of Metallic Films deposited by Electrolysis," Proc. R. Soc. London. Ser. A, vol. 82, no. 553, pp. 172–175, 1909.

[129] C. H. Hsueh, "Modeling of elastic deformation of multilayers due to residual stresses and external bending," J. Appl. Phys., vol. 91, no. 12, pp. 9652–9656, 2002.

[130] C. H. Hsueh, "Thermal stresses in elastic multilayer systems," Thin Solid Films, vol. 418, no. 2, pp. 182–188, 2002.

[131] G. P. Nikishkov, "Curvature estimation for multilayer hinged structures with initial strains," J. Appl. Phys., vol. 94, no. 8, pp. 5333–5336, 2003.

[132] S. Wagner, H. Gleskova, I. C. Cheng, J. C. Sturm, and Z. Suo, "Mechanics of TFT Technology on Flexible Substrates," in Flexible Flat Panel Displays, vol. 1, West Sussex, England: John Wiley & Sons, Ltd, 2005, pp. 263–283.

[133] A. V. da Silva, B. Mimoun, and R. Dekker, "FleSS: a Matlab Based Graphical User Interface for Stress–Strain Analytical Modeling of Multilayered Structures with Applied Bending," in Proceedings SAFE Workshop, 2010, no. July 2015, pp. 175–179.

[134] A. N. V. da Silva, "Analytical Modeling of the Stress-Strain Distribution in a Multilayer Structure with Applied Bending," Instituto Superior Técnico, Lisbon, Portugal, 2010.

[135] T. Li, Z. Zhang, and B. Michaux, "Competing failure mechanisms of thin metal films on polymer substrates under tension," Theor. Appl. Mech. Lett., vol. 1, no. 4, p. 041002, 2011.

[136] B. Mimoun, H. T. M. Pham, V. Henneken, and R. Dekker, "Residue-free plasma etching of polyimide coatings for small pitch vias with improved step coverage," J. Vac. Sci. Technol. B Microelectron. Nanom. Struct., vol. 31, no. 2, p. 021201, 2013.

[137] G. Turban and M. Rapeaux, "Dry Etching of Polyimide in O -CF, and O -SF Plasmas," J. Electrochem. Soc., vol. 30, no. 11, pp. 2231–2236, 1983.

[138] W. Vanderlinde and A. Ruoff, "Reactive ion beam etching of polyimide thin films," Vac. Sci. B Microelectron. Nanom. Struct., vol. 6, no. 6, pp. 1621–1625, 1988.

[139] U. Buder, J. P. von Klitzing, and E. Obermeier, “Reactive ion etching for bulk structuring of polyimide,” Sensors Actuators A Phys., vol. 132, no. 1, pp. 393–399, 2006.

[140] V. Bliznetsov, A. Manickam, J. Chen, and N. Ranganathan, “High- throughput anisotropic plasma etching of polyimide for mems,” J. Micromechanics Microengineering, vol. 21, no. 6, p. 067003, 2011.

[141] C. Mogab, A. Adams, and D. Flamm, “Plasma etching of si and si02— the effect of oxygen additions to cf4 plasmas,” J. Appl. Phys., vol. 49, no. 7, pp. 3796–3803, 1978.

[142] a a Taylor, M. J. Cordill, L. Bowles, J. Schalko, and G. Dehm, “An elevated temperature study of a Ti adhesion layer on polyimide.,” Thin Solid Films, vol. 531, no. C, pp. 354–361, Mar. 2013.

[143] F. Fracassi, R. D’Agostino, R. Lamendola, and I. Mangieri, “Dry etching of titanium nitride thin films in CF 4 –O 2 plasmas,” J. Vac. Sci. Technol. A Vacuum, Surfaces, Film., vol. 13, no. 2, pp. 335–342, 1995.

[144] J. Meregnani et al., “Anti-inflammatory effect of vagus nerve stimulation in a rat model of inflammatory bowel disease.,” Auton. Neurosci., vol. 160, no. 1–2, pp. 82–9, Feb. 2011.

[145] S. E. Krahl, “Vagus nerve stimulation for epilepsy: A review of the peripheral mechanisms.,” Surg. Neurol. Int., vol. 3, no. Suppl 1, pp. S47-52, Jan. 2012.

[146] S. S. Chavan et al., “A novel flexible cuff-like microelectrode for dual purpose, acute and chronic electrical interfacing with the mouse cervical vagus nerve,” J. Neural Eng., vol. 14, no. 6, p. 066005, 2017.

[147] A. C. Licursi de Alcântara, H. C. Salgado, and V. P. Sassoli Fazan, “Morphology and morphometry of the vagus nerve in male and female spontaneously hypertensive rats,” Brain Res., vol. 1197, pp. 170–80, Mar. 2008.

[148] R. L. Calloni et al., “Transient middle cerebral artery occlusion in rats as an experimental model of brain ischemia,” Acta Cir. Bras., vol. 25, no. 5, pp. 428–433, 2010.

[149] Z. Lertmanorat, K. J. Gustafson, and D. M. Durand, “Electrode array for reversing the recruitment order of peripheral nerve stimulation: experimental studies.,” Ann. Biomed. Eng., vol. 34, no. 1, pp. 152–60, Jan. 2006.

[150] S. F. Cogan, “Neural stimulation and recording electrodes.,” Annu. Rev. Biomed. Eng., vol. 10, pp. 275–309, Jan. 2008.

[151] J. C. Williams, J. A. Hippensteel, J. Dilgen, W. Shain, and D. R. Kipke, “Complex impedance spectroscopy for monitoring tissue responses to inserted neural implants,” J. Neural Eng., vol. 4, no. 4, pp. 410–423, 2007.

[152] R. K. Shepherd, J. Matsushima, R. L. Martin, and G. M. Clark, “Cochlear pathology following chronic electrical stimulation of the auditory nerve: II deafened kittens,” Hear. Res., vol. 81, no. 1–2, pp. 150–166, 1994.

[153] F. Steigerwald et al., “Pulse duration settings in subthalamic stimulation for Parkinson’s disease,” Mov. Disord., vol. 33, no. 1, pp. 165–169, 2017.

[154] T. M. Bruns, D. J. Weber, and R. A. Gaunt, “Microstimulation of Afferents in the Sacral Dorsal Root Ganglia Can Evoke Reflex Bladder Activity,” Neurourol. Urodyn., vol. 34, no. 1, pp. 65–71, 2015.

[155] D. B. McCreery, T. G. H. Yuen, W. F. Agnew, and L. A. Bullara, “Stimulus parameters affecting tissue injury during microstimulation in the cochlear nucleus of the cat,” Hear. Res., vol. 77, no. 1–2, pp. 105–115, 1994.

[156] D. B. McCreery, W. F. Agnew, and L. Bullara, “Charge density and charge per phase as cofactors in neural injury induced by electrical stimulation,” IEEE Trans. Biomed. Eng., vol. 37, no. 10, pp. 996–1001, 1990.

[157] L. A. Bullara, D. B. McCreery, W. F. Agnew, and T. G. Yuen, “Comparison of neural damage induced by electrical stimulation with faradaic and capacitor electrodes.,” Ann. Biomed. Eng., vol. 16, no. 5, pp. 463–481, 1988.

[158] R. V. Shannon and S. R. Otto, “Psychophysical measures from electrical stimulation of the human cochlear nucleus,” Hear. Res., vol. 47, no. 1–2, pp. 159–168, 1990.

[159] Z. Lertmanorat, F. Montague, and D. Durand, “A Flat Interface Nerve Electrode With Integrated Multiplexer,” IEEE Trans. Neural Syst. Rehabil. Eng., vol. 17, no. 2, pp. 176–182, 2009.

[160] M. Ochoa, P. Wei, A. J. Wolley, K. J. Otto, and B. Ziaie, “A hybrid PDMS-Parylene subdural multi-electrode array.,” Biomed. Microdevices, vol. 15, no. 3, pp. 437–43, Jun. 2013.

[161] R. Baratta, M. Ichie, S. K. Hwang, and M. Solomonow, “Orderly stimulation of skeletal muscle motor units with tripolar nerve cuff electrode,” IEEE Trans. Biomed. Eng., vol. 36, no. 8, pp. 836–843, 1989.

[162] S. M. Lawrence, J. O. Larsen, K. W. Horch, R. Riso, and T. Sinkjr, “Long-term biocompatibility of implanted polymer-based intrafascicular electrodes,” J. Biomed. Mater. Res., vol. 63, pp. 501–506, 2002.

[163] J. D. Weiland, D. J. Anderson, and M. S. Humayun, “In vitro electrical properties for iridium oxide versus titanium nitride stimulating electrodes,” IEEE Trans. Biomed. Eng., vol. 49, no. 12, pp. 1574–1579, 2002.

[164] M. Janders, U. Egert, M. Stelzle, and W. Nisch, “Novel thin film titanium nitride micro-electrodes with excellent charge transfer capability for cell stimulation and sensing applications,” in Proceedings of the 18th Annual International Conference of the IEEE Engineering in Medicine and BIology, 1996, pp. 245–247.

[165] W. Franks, I. Schenker, P. Schmutz, and A. Hierlemann, “Impedance characterization and modeling of electrodes for biomedical applications.,” IEEE Trans. Biomed. Eng., vol. 52, no. 7, pp. 1295–302, Jul. 2005.

[166] S. Meijs, M. Fjorback, and N. J. M. Rijkhoff, “Chronic Electrochemical Investigation of Titanium Nitride Stimulation Electrodes in vivo,” Converging Clin. Eng. Res. Neurorehabilitation, vol. 1, pp. 421–425, 2013.

[167] D. R. Merrill, M. Bikson, and J. G. R. Jefferys, “Electrical stimulation of excitable tissue: design of efficacious and safe protocols.,” J. Neurosci. Methods, vol. 141, no. 2, pp. 171–98, Feb. 2005.

[168] Bard, Allen J and L. R. Faulkner, Electrochemical Methods: Fundamentals and Applications, 2nd editio. John Wiley & Sons, Inc., 2001.

[169] J. E. B. Randles, “Kinetics of Rapid Electrode Reactions,” Discuss Faraday Soc, vol. 1, pp. 11–19, 1947.

[170] L. S. Robblee and T. L. Rose, “Electrochemical guidelines for selection of protocols and electrode materials for neural stimulation,” in Neural Prostheses, W. F. M. A. D. B. McCreery, Ed. Englewood Cliffs, NJ: Prentice Hall, 1990, pp. 25–66.

[171] A. Norlin, J. Pan, and C. Leygraf, “Investigation of Electrochemical Behavior of Stimulation/Sensing Materials for Pacemaker Electrode Applications,” J. Electrochem. Soc., vol. 152, no. 2, pp. J7–J15, 2005.

[172] S. Meijs, C. Sørensen, S. Sørensen, K. Rechendorff, M. Fjorback, and N. J. M. Rijkhoff, “Influence of implantation on the electrochemical properties of smooth and porous TiN coatings for stimulation electrodes.,” J. Neural Eng., vol. 13, no. 2, p. 026011, 2016.

[173] T. L. Rose and L. S. Robblee, “Electrical stimulation with Pt electrodes. VIII. Electrochemically safe charge injection limits with 0.2 ms pulses,” Biomed. Eng. IEEE, vol. 37, no. 11, pp. 1118–20, 1990.

[174] X. Beebe and T. L. Rose, “Charge Injection Limits of Activated Iridium Oxide Electrodes with 0.2 ms Pulses in Bicarbonate Buffered Saline,” Med. Biol. Eng. Comput., vol. 35, no. 6, pp. 494–495, 1988.

[175] S. F. Cogan, P. R. Troyk, J. Ehrlich, T. D. Plante, and D. E. Detlefsen, “Potential-biased, asymmetric waveforms for charge-injection with activated iridium oxide (AIROF) neural stimulation electrodes,” IEEE Trans. Biomed. Eng., vol.

53, no. 2, pp. 327–332, 2006.

[176] R. T. Leung, M. N. Shivdasani, D. A. X. Nayagam, and R. K. Shepherd, "In vivo and in vitro comparison of the charge injection capacity of platinum macroelectrodes," IEEE Trans. Biomed. Eng., vol. 62, no. 3, pp. 849–857, 2015.

[177] S. F. Cogan, P. R. Troyk, J. Ehrlich, C. M. Gasbarro, and T. D. Plante, "The influence of electrolyte composition on the in vitro charge-injection limits of activated iridium oxide (AIROF) stimulation electrodes," J. Neural Eng., vol. 4, no. 2, pp. 79–86, 2007.

[178] G. Bellanger and J. J. Rameau, "Corrosion of Titanium Nitride Deposits on AISI 630 Stainless Steel used in Radioactive Water With and Without Chloride at pH 11," Acta, Electrochim., vol. 40, no. 15, 1995.

[179] S. F. Cogan, D. J. Garrett, and R. A. Green, "Electrochemical Principles of Safe Charge Injection," in Neurobionics: The Biomedical Engineering of Neural Prostheses, 1st ed., R. K. Shepherd, Ed. Wiley Blackwell, 2016, pp. 55–88.

[180] L. T. Cunha, P. Pedrosa, C. J. Tavares, F. Vaz, C. Fonseca, and E. Alves, "The role of composition, morphology and crystalline structure in the electrochemical behaviour of TiNx thin films for dry electrode sensor materials," Electrochim. Acta, vol. 55, no. 1, pp. 59–67, 2009.

[181] M. Janders, U. Egert, M. Stelzle, and W. Nisch, "Novel thin film titanium nitride micro-electrodes with excellent charge transfer capability for cell stimulation and sensing applications," in 18th Annual International Conference of the IEEE Engineering in Medicine and Biology Society, 1996, pp. 245–247.

[182] S. F. Cogan et al., "Sputtered iridium oxide films for neural stimulation electrodes," J. Biomed. Mater. Res. - Part B Appl. Biomater., vol. 89, no. 2, pp. 353–361, 2009.

[183] W. Tato and D. Landolt, "Electrochemical Determination of the Porosity of Single and Duplex PVD Coatings of Titanium and Titanium Nitride on Brass," J. Electrochem. Soc., vol. 145, no. 12, p. 4173, 1998.

[184] A. Baudrant and M. Sacilotti, "The LPCVD Polysilicon Phosphorus Doped In Situ as an Industrial Process," J. Electrochem. Soc., vol. 129, no. 5, pp. 1109–1116, 1982.

[185] F. Rodrigues, S. Gomes, P. Anacleto, J. Fernandes, and P. M. Mendes, "RF CMOS wireless implantable microsystem for sacral roots stimulation with on-chip antenna and far-field wireless powering," in European Microwave Week 2015: "Freedom Through Microwaves", EuMW 2015 - Conference Proceedings; 2015 45th European Microwave Conference Proceedings, EuMC, 2015, pp. 76–79.

[186] A. C. Fischer et al., "Integrating MEMS and ICs," Microsystems Nanoeng., vol. 1, no. March, p. 15005, 2015.